Stellar Population Templates in the Near-Infrared

by

Crystal Brasseur
B.Sc., University of Victoria, 2007

A Dissertation Submitted in Partial Fulfillment of the
Requirements for the Degree of

MASTER OF SCIENCE

in the Department of Physics and Astronomy

Stellar Population Templates in the Near-Infrared

by

Crystal Brasseur
B.Sc., University of Victoria, 2007

Supervisory Committee

Dr. Peter B. Stetson, Supervisor
(Herzberg Institute of Astrophysics)

Dr. Don A. VandenBerg, Supervisor
(Department of Physics and Astronomy)

Dr. Kim Venn, Departmental Member
(Department of Physics and Astronomy)

Dr. Jon Willis, Departmental Member
(Department of Physics and Astronomy)

Supervisory Committee
Dr. Peter B. Stetson, Supervisor
(Herzberg Institute of Astrophysics)

Dr. Don A. VandenBerg, Supervisor
(Department of Physics and Astronomy)

Dr. Kim Venn, Departmental Member
(Department of Physics and Astronomy)

Dr. Jon Willis, Departmental Member
(Department of Physics and Astronomy)

ABSTRACT

We have obtained broad-band NIR-photometry for six Galactic star clusters, M92, M15, M13, NGC1851, M71 and NGC6791, as observed with the WIRCam wide-field imager on the Canada-France-Hawaii Telescope; supplemented by images taken with HAWK-I on VLT. From the resultant $(V-J)$-V and $(V-K)$-V colour-magnitude diagrams, fiducial sequences spanning the range in metallicity, $-2.4 \leq$ [Fe/H] $\leq +0.3$, have been defined which extend from the tip of the red-giant branch to ~ 2.5 magnitudes below the main-sequence turnoff. These fiducials provide a valuable set of empirical isochrones for the interpretation of stellar population data in the 2MASS system. From the NIR data, the reddenings of M15, M71 and NGC6791 — which have been subject to considerable controversy — were found to be E$(B-V)$= 0.075, 0.22 and 0.155 mag respectively

Comparisons of our CMDs to Victoria isochrones that have been transformed using the MARCS model colour-$T_{\rm eff}$ relations reveal that the models reproduce the giant branches of clusters more metal-rich than [Fe/H] ≈ -1.3, but they become systematically redder than the observed RGBs as the cluster metallicity decreases. These discrepancies are seen consistently in the two colours and therefore may indicate that the temperature scale of the stellar evolutionary models for giant stars at low metallicity is too cool.

MARCS colour transformations were also tested using the classic Population II subdwarfs. The MARCS colours show redward offsets of ~ 0.03 mag when compared with the observed $(V - K)$ and $(J - K)$ colours (assuming best estimates of $T_{\rm eff}$, log g, and [Fe/H]), and a systematic blue offset relative to the isochrone temperatures. Together with the indications from the cluster $(V - K)$ and $(V - J)$ CMDs, these results suggest that there is a problem with the MARCS colour transformations involving J.

Contents

List of Tables

List of Figures

ACKNOWLEDGEMENTS

I would like to thank my advisors, Peter Stetson and Don VandenBerg, who have not only made this research possible, but who have been so generous with their time and enthusiasm towards this project. In discussions with them, I have learned far more about photometry and stellar astrophysics than from any textbook.

Chapter 1

Introduction

1.1 Motivation

As the infrared region of the electromagnetic spectrum receives growing attention in modern astrophysics, it becomes desirable to have deep near-infrared photometry for Galactic star clusters spanning a wide range in metallicity. Star clusters are ideal stellar populations because, with just a few exceptions (e.g., ω Cen), the stars in a given cluster are homogeneous in both *age* and initial *chemical composition*. These systems not only provide us with exceedingly valuable stellar population templates, but they help us to refine the predicted colours of model atmospheres, and temperatures of stellar evolutionary models.

Only recently have infrared detectors begun to approach the photometric capabilities of optical detectors. Now a new generation of infrared detectors such as CFHT/WIRCam, UKIRT/WFCAM and, shortly, WFC3, will allow us to probe stellar populations to high photometric accuracy even in dust-obscured and heavily reddened galaxies. An important first step in analyzing these data will be to compare their observations with nearby, well-studied, simple stellar populations (i.e., open and globular clusters) spanning the full range in [Fe/H] from -2.4 to $+0.3$. With spectroscopic metallicity determinations and age estimates that are accurate to within $\pm$ 0.25 dex and $\pm$ 2 Gyr, respectively, the fiducials of these simple stellar populations can, in principal, be used to photometrically determine the age and metallicity of resolved stellar systems. Unlike isochrone analyses, metallicity determinations made through comparisons with fiducials are independent of any evolutionary model. Near-infrared fiducials become increasingly desirable for these determinations since evolved stellar

populations emit the majority of their light at infrared wavelengths and therefore can be seen out to great distances.

Currently available near-infrared fiducials of Galactic star clusters are restricted in both metallicity and magnitude range, with the observations rarely extending to fainter magnitudes than the base of the red giant branch. In addition, Figure 1.1 provides evidence that the near-infrared fiducial sequences of some Galactic globular clusters (GGCs) have not been reliably determined. The upper panel shows that, when current best estimates of distance and reddening are assumed, the red giant branch (RGB) of M13 is appreciably bluer than that of M3 on the $(V-K)_0$-M_K plane, despite both having similar [Fe/H] values to within ~ 0.1 dex (Carretta & Gratton 1997, Kraft & Ivans 2003). The CMDs obtained for these clusters from BVI studies (e.g., Johnson & Bolte 1998) show little or no separation between their RGBs. In the lower panel of Figure 1.1, a more troubling difference is seen for the same clusters: the RGB of M13 is *redder* than that of M3 in the $(J-K)_0$-M_K plane despite the fact that, if anything, M13 is believed to be slightly more metal-poor than M3.

To address the need for precise fiducial sequences in the near-infrared, we have obtained observations of six Galactic star clusters, M92, M15, M13, NGC1851, M71 and NGC6791. Not only will these observations result in an improved understanding of globular clusters, they will provide tests of synthetic colour-$T_{\rm eff}$ relations which transform the effective temperatures of stellar evolutionary models into observed colours. Note that only in the case of star clusters can we be certain which relations connect dwarfs and giants of the same metallicity.

At present, both the theoretical and empirical (i.e., field-star based) colour-$T_{\rm eff}$ relations are subject to considerable uncertainty in the near-infrared. As shown in Figure 1.2, for instance, recent $(V-K)$ versus $T_{\rm eff}$ relations imply up to ~ 0.18 mag differences in the predicted colours at a given M_V along the RGB segments of theoretical isochrones.

Isochrones, and in particular their RGB segments, are ultimately used to infer the ages, metallicities and star formation histories of much more distant stellar systems. Thus, the ability of colour-temperature relations to reproduce the fiducials of Galactic star clusters is a key requirement for the accurate application of stellar evolutionary models to heterogeneous populations of stars such as dwarf galaxies.

1.2 Previous Infrared Surveys

Frogel, Cohen & Persson (1983) were the first to present a survey of Galactic globular clusters (GGCs) in the infrared (IR). Owing to intrinsic technical limitations of the older generation of single-channel detectors, they were able to observe only a few bright stars in the external regions of the clusters (a total of 306 stars in 26 GGCs). Even with the observational limitations, Frogel et al. were able to investigate the dependence of the RGB location on metallicity. However, a detailed comparison with theoretical models based on suitable luminosity functions was impossible because of the low star counts.

With the technological improvements of modern infrared detectors, the limitations experienced by Frogel et al. have now been eliminated. One modern survey (Ferraro et al., 2000) affords well populated J and K CMDs for 10 GGCs and its authors were able to present, for the first time, a detailed analysis of the RGB behavior as a function of metallicity. These relations were used to derive a photometric estimate of a globular cluster's metal content from the RGB morphology and location. One limitation of this survey, however, is that it includes only RGB segments, as turn-off and main-sequence stars were not obtainable with their integration times.

A more recent survey by Valenti et al. (2007) presents near-IR colour-magnitude diagrams for a sample of 24 Galactic globular clusters. All clusters included in this survey were situated in the Galactic bulge, allowing Valenti et al. to explore RGB morphology in the high-metallicity range. It is important to note that this type of survey at optical wavelengths would be difficult-to-impossible due to the high interstellar extinction; however, this problem is almost completely eliminated at infrared wavelengths. This homogeneous compilation of bulge GGCs by Valenti has resulted in empirical templates for the RGBs of metal-rich stellar populations. However, as with the survey by Ferraro et al. (2000), fainter magnitudes than the RGB were not observed.

1.3 Existing Colour - $T_{\rm eff}$ Relations

It is instrumental in analyses of stellar populations to compare observations with stellar evolutionary models. By overlaying appropriate isochrones onto observed CMDs, we are able to infer ages, as well as check the reliability of distance and metallicity estimates. However, theoretical stellar models predict effective temperatures and lu-

minosities — so to compare with observations, one must employ colour-$T_{\rm eff}$ relations which transform the effective temperatures into colours that can be directly observed.

Colour-$T_{\rm eff}$ relations are derived by using either theoretical or empirical methods. For the former, theoretical grids of synthetic colours are produced by convolving the desired photometric bandpasses with synthetic spectra of stars having a range of $T_{\rm eff}$, gravity and metallicity. $T_{\rm eff}$ refers to the temperature of an equivalent black body, i.e., one with the same luminosity per unit surface area as the star, defined according to the Stefan-Boltzmann law $\frac{L}{4\pi R^2} = \sigma T_{eff}^4$ where R is the stellar radius, and L is the luminosity of the star. Thus $T_{\rm eff}$ is a derived quantity from the luminosity and radius, and cannot be directly observed. Rather, one can observe a star's luminosity and estimate its radius from lunar occultations or interferometric methods. By combining these temperatures with colour observations from two different photometric bands, empirical colour-$T_{\rm eff}$ relations can be derived.

When angular diameter observations are not available, empirical colour-$T_{\rm eff}$ relations often use indirect methods to estimate the temperatures of stars. The least model-dependent approach to the direct method is considered to be the infrared flux method (IRFM), where the temperature is found from a comparison between the observed and theoretical ratio of the bolometric flux to the infrared flux. This method, developed by Blackwell & Shallis (1977), derives angular diameters, θ, and effective temperatures, $T_{\rm eff}$. It is based on the insensitivity to $T_{\rm eff}$ of the surface flux, $F_{S,\lambda}$, from a star at an infrared wavelength, λ. The steps for this method are as follows:

1. Use a model atmosphere to compute the surface flux $F_{s,\lambda}$ at an infrared wavelength, λ, using initial estimates of $T_{\rm eff}$ and g.

2. Calculate a value for the angular diameter, θ, from

$$\theta = 2\sqrt{\frac{F_{E,\lambda}}{F_{s,\lambda}}}. \tag{1.1}$$

   where $F_{E,\lambda}$ is the measured flux at the Earth.

3. Using the model value obtained for bolometric flux and the above estimate for θ, calculate $T_{\rm eff}$ from

$$F_{bol} = \frac{\theta^2 \sigma T_{\rm eff}^4}{4}. \tag{1.2}$$

4. Repeat the procedure until convergence is obtained.

The infrared flux method has been used in recent years by several groups (e.g., Alonso et al. 1996, Ramírez & Meléndez 2005, etc.) to derive empirical colour-$T_{\rm eff}$ relations. The consistency of this method can be tested by deriving temperatures using several near-infrared bands. Alonso et al. (1996) found excellent agreement between them for stars hotter than 4000 K as shown in Figure 1.3 (below 4000K, molecular absorption begins to have a strong effect on the emitted stellar light).

For determining the effective temperatures of stars between 4000 K and 8000 K, $(V-K)$ colours are highly favoured, in part because the large baseline of the colour index means that reasonably large uncertainties in the K magnitude, for instance, will not greatly affect the derived temperature. However, studies conflict as to whether there is a strong metallicity dependance in this relation. For example, Alonso et al. (1999) found a weak dependence of [Fe/H] on calibrations of $T_{\rm eff}$ for dwarf stars of metallicities $-2.5\leq$[Fe/H]≤ 0.5 using $(V-K)$ photometry—see Figure 1.4 where the empirical relations have been fitted to polynomials resulting in a precision of the temperatures of $\approx$ 40 K at a given $(V-K)$ colour. Alonso et al. also find good consistency between the derived effective temperatures for the same giant stars in other studies (Figure 1.5).

Building upon the work of Alonso et al. (1999), Ramírez & Meléndez (2005) constructed a much larger sample of stars, especially populating the low metallicity regime. Shown in Figure 1.6 are the results of Ramírez & Meléndez for both dwarfs (upper panel) and giants (lower panel) as compared to predictions from the MARCS and Kurucz model atmospheres. At the solar metallicity the slopes of the relations are in reasonable agreement with dwarf calibrations above 4500 K and with the calibrations for giants below 5500 K. Their $(V-K)$-$T_{\rm eff}$ relation shows a very strong metallicity effect in the cool dwarfs, in the sense that the most metal-poor stars are very blue. The cool dwarfs are bluer also according to the theory, but the effect there is not as strong.

Ramírez & Meléndez (2005) state that the Kurucz and MARCS colours are in reasonable qualitative agreement with their findings but the latter fail to reproduce the detailed dependence on metallicity. The Ramírez & Meléndez $T_{\rm eff}$ scale is significantly hotter at low metallicity than the H_α-based $T_{\rm eff}$ scale (Nissen et al. 2007). Their scale is also hotter than the IRFM calibration of Alonso et al. (1996) which is uggested by Ramírez & Meléndez to be due to low statistics in the metal-poor regime of the former's sample of stars.

1.4 Scope of the Present Study

In the 2008B semester, we received time on CFHT/WIRCam to observe five Galactic star clusters (NGC6791, M13, M15, M92 and M71) in J and K. In addition, K-band images of NGC1851, taken with the VLT HAWK-I detector, were provided to us by our Italian collaborators, Giuseppe Bono and Massimo Dall'Ora.

In the following Chapter we present the details related to the reduction of these observations, including the calibration of our photometry to the standard 2MASS system. In Chapter 3, the colour-magnitude diagrams and fiducials are presented which provide template stellar population sequences for the range in [Fe/H]$= -2.4$ to $+0.3$. Chapter 4 presents an analysis of the implications of these data for synthetic colour-$T_{\rm eff}$ relations and theoretical isochrones. Finally, a short summary of our results, as well as a discussion of the usefulness of these fiducials for stellar populations research, is given in Chapter 5.

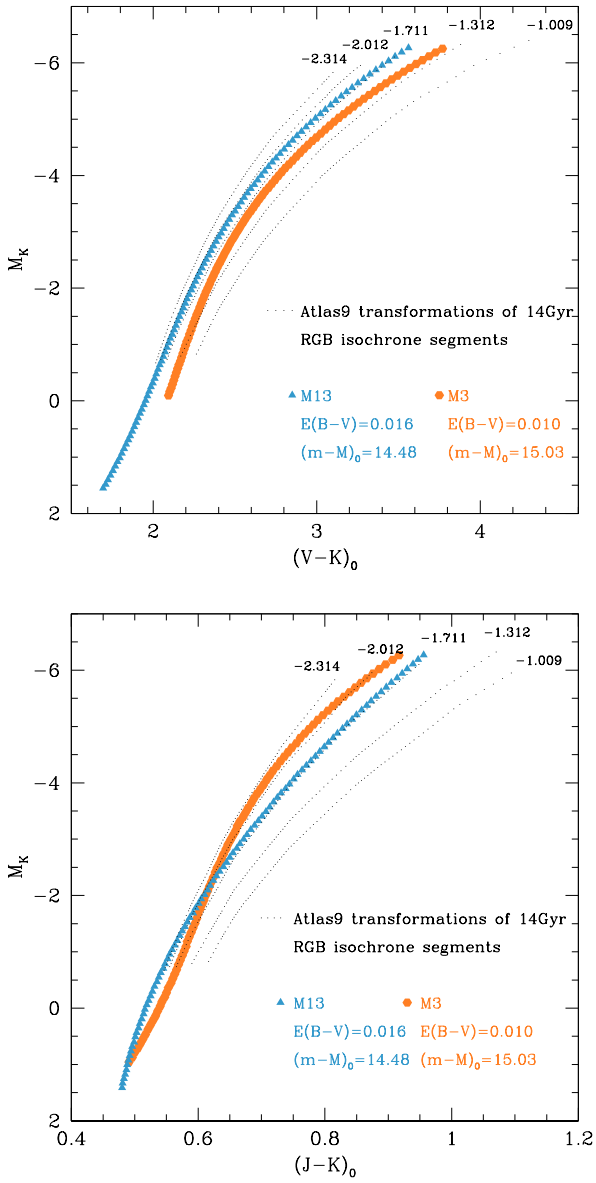

Figure 1.1 Upper: RGB fiducials for M13 (blue triangles) and M3 (orange circles) from Valenti et al. (2004) in the $(V-K)_0$-M_K plane superimposed on the RGB segments of 14 Gyr isochrones by VandenBerg et al. (2006; black dotted lines) as transformed to the near-infrared using the Atlas9 transformations. Although these clusters have similar metallicities (within ~ 0.1 dex), M13 appears appreciably bluer than M3. Lower: Same as the upper panel, but for $(J-K)_0$. Although M13 is more metal poor than M3, here it appears redder than M3, contrary to what is seen in the upper panel. This suggests that these fiducial sequences have not been reliably determined. Note that the upper portion of the M13 fiducial lies along [Fe/H]$= -1.711$ in both panels.

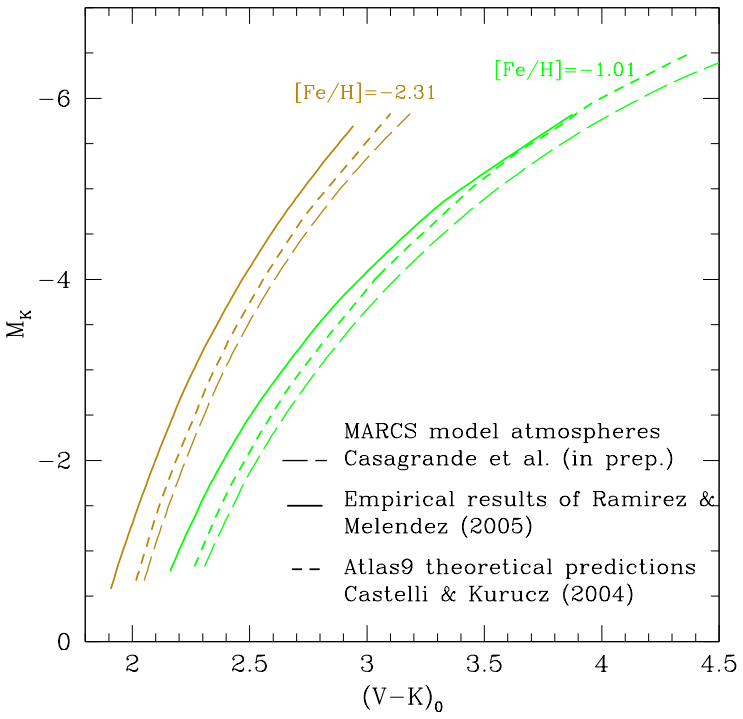

Figure 1.2 A comparison of RGB segments of 14 Gyr Victoria isochrones of two metallicities (as noted) that have been transformed to the observational plane using the empirically constrained $(V-K)$-$T_{\rm eff}$ relations (Ramirez & Melendez 2005; solid lines), the theoretical Atlas9 predictions by Castelli & Kurucz (2004; short dashed lines), and MARCS model atmosphere transformations (long dashed lines) by Casagrande et al. (in preparation).

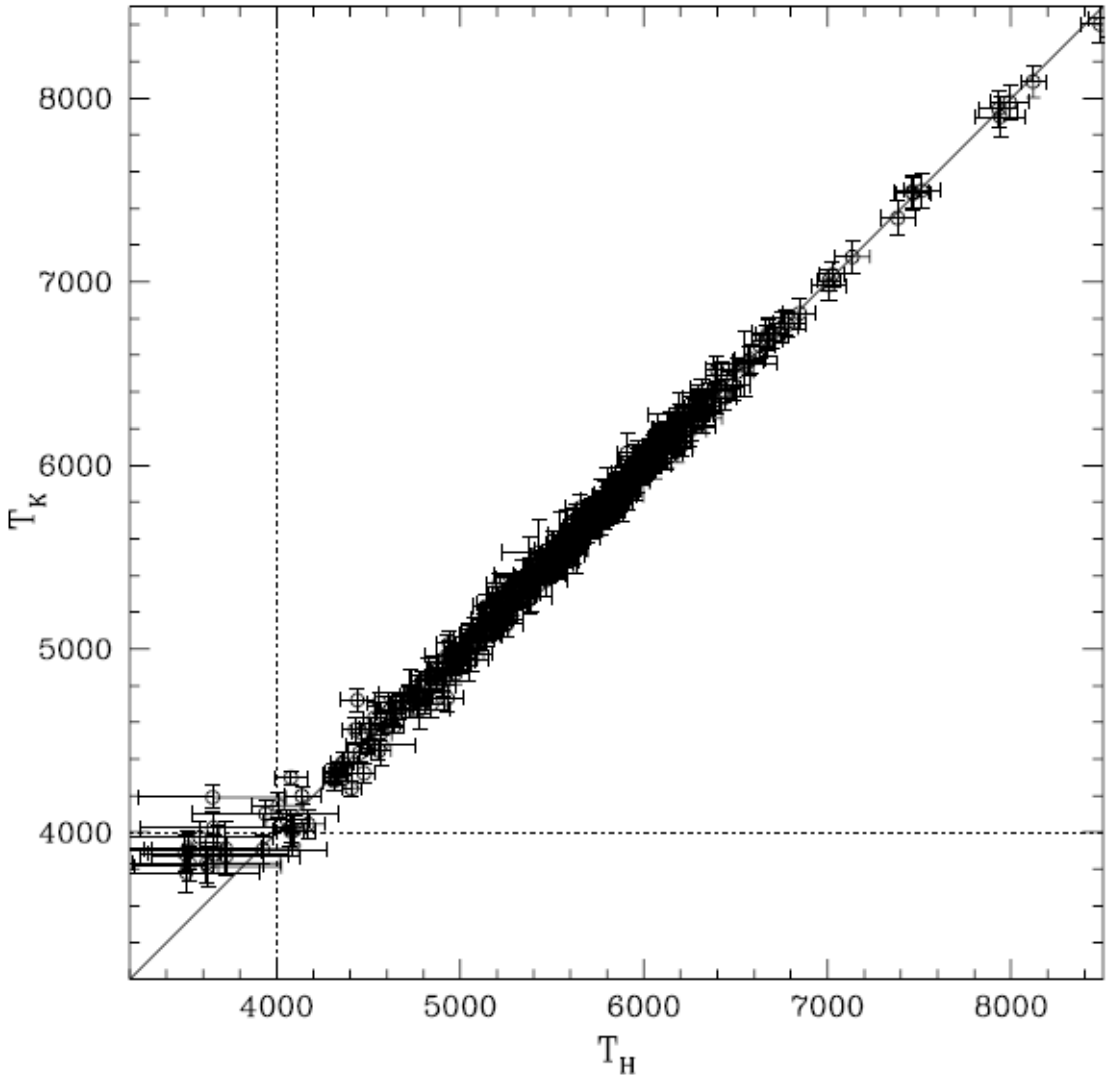

Figure 1.3 Stellar effective temperatures in the H and K bands, T_H and T_K respectively, as derived from the infrared flux method by Alonso et al. (1996). Good consistency is found for stars with temperatures above 4000 K.

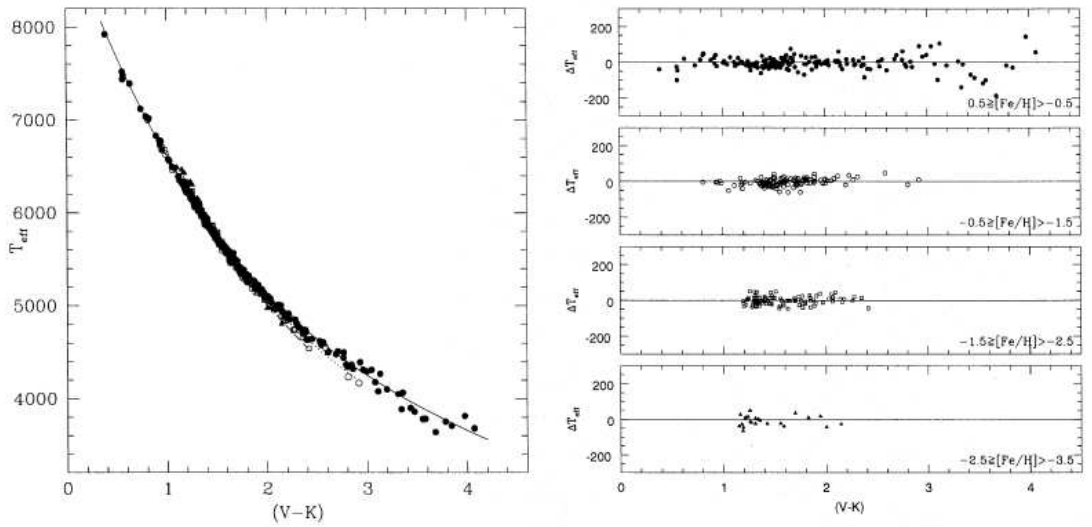

Figure 1.4 The dependence of $T_{\rm eff}$ on $(V-K)$ for low main sequence stars ranging from F0V to K5V as derived by Alonso et al. (1996) using the infrared flux method. In the left-hand panel points are separated according to metallicity as shown in the right hand panel.

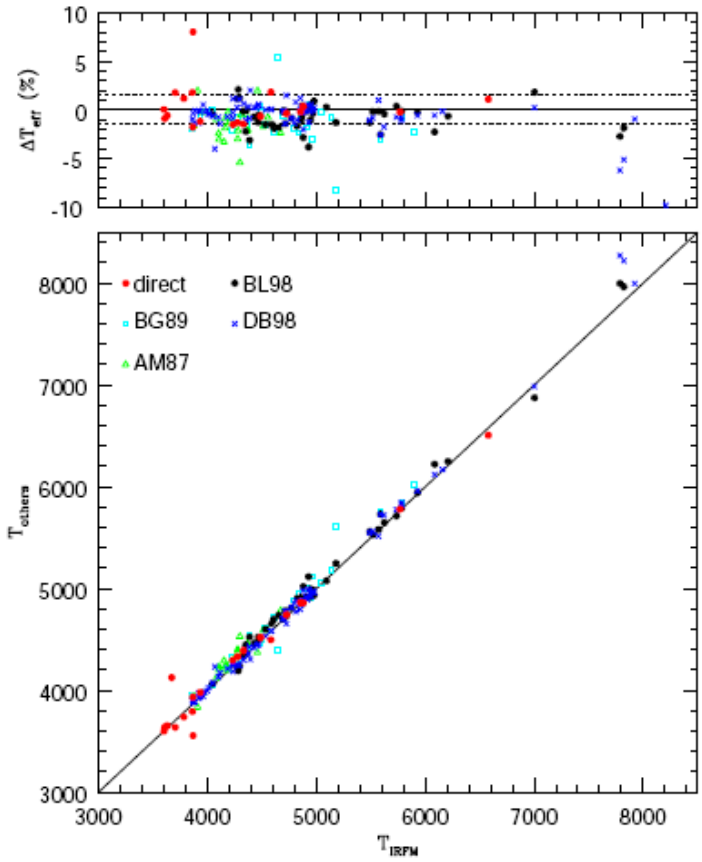

Figure 1.5 Alonso et al. (1998) compare their estimates of $T_{\rm eff}$ for giant stars ranging from F0 to K5 with the results of previous studies. Direct measurements: Code et al. (1976; C76), Ridgway et al. (1980; R80), Di Benedetto & Rabbia (1987; BR87), Hutter et al. (1989; H89), Mozurkewich et al. (1991; M91), and White & Feiermann (1987; WF87)), squares: Bell & Gustafsson (1989), triangles: Arribas & Martinez-Roger (1987), stars: Blackwell & Lynas-Gray (1998). In upper plot, the lines corresponding to the mean internal error of the work ($\pm$ 1.5%) are shown.

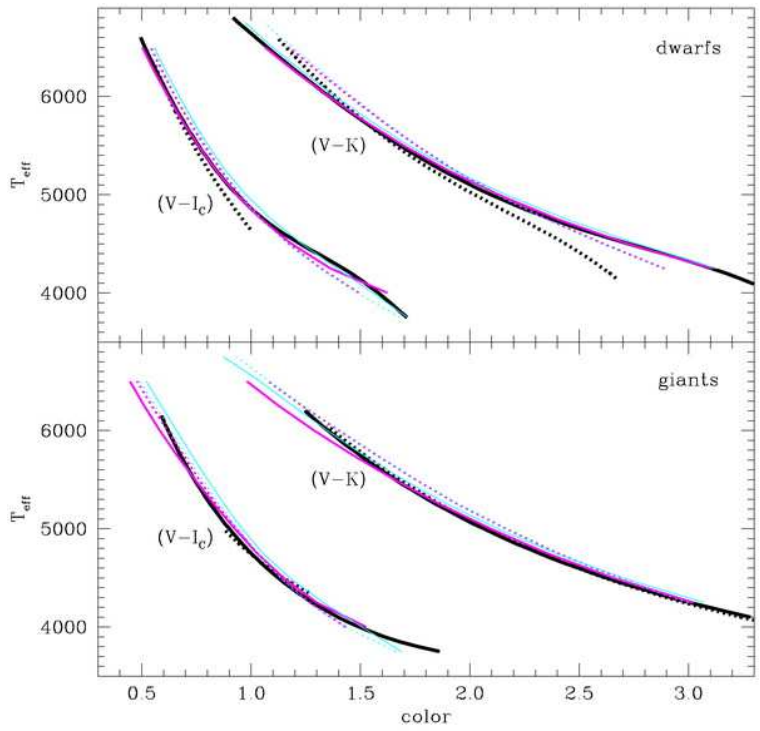

Figure 1.6 From Ramírez & Meléndez (2005). $T_{\rm eff}$ vs. $(V - I_C)$ and $(V - K)$ relations for dwarf (top) and giant (bottom) stars of [Fe/H] = +0.0 (solid lines) and −2.0 (dotted lines) according to the work of Ramírez & Meléndez (2005), (thick black lines), Bessell (Kurucz models 2004, thin cyan lines), and Houdashelt et al. (MARCS models 2000; magenta lines).

Chapter 2

Data Reduction

2.1 Introduction

Infrared photometry possesses various advantages compared to optical observations. For example, significantly reduced attenuation unveils otherwise dust-obscured regions, and evolved stellar systems are brightest at these longer wavelengths, allowing us to probe stellar populations out to greater distances. However, there are also several relative drawbacks and challenges arising in connection with near-infrared observations; arguably the most severe stemming from background thermal emission.

Only in the last few years have infrared detectors begun to reach the capabilities of optical CCDs in terms of pixel resolution, sensitivity (quantum efficiency) and stability. The latter, for example, requires considerable effort to facilitate cooling of the detector, otherwise thermal noise from within the instrument would vastly dominate any science signal.

Even with technological advances, all ground-based telescopes inevitably suffer from a high level of thermal noise from atmospheric emission. This emission is temporally variable, on the order of minutes, in both level and structure. Because of this, a significant number of intermittent exposures off-target (in our case 50% of our requested time) are required in order to approximately reconstruct the "sky". In this way, the constantly varying sky background can be subtracted as quickly as possible and asymmetries in the background can be minimized. Even after removing the sky flux, the signal-to-noise-ratios are largely impacted, especially for low surface brightness targets. On the technical side, the instrument used for our observations, WIRCam on CFHT, has a low dynamic range relative to an optical CCD: the short-

est and longest possible exposures in K-band merely differ by a factor of five, so any objects which are just a few times brighter than the sky background become prone to inescapable saturation themselves.

2.2 Data Reduction

2.2.1 Pre-Processing

Our CFHT observations aimed at reaching a signal-to-noise ratio of 25 at 2.5 magnitudes below the main sequence turn-off of each cluster. To accomplish this, exposure times as given in Table 2.2.1 were observed where the observations were chosen to be primarily longer exposures (20 seconds in K and 40 sec in J), together with several of the shortest possible exposures (5 sec in J and K) to avoid saturation of the brightest stars. The latter was critical in order to calibrate our fields to 2MASS-photometry which has sufficient precision for point sources down to the base of the giant branch at the distances of our clusters.

As previously mentioned, atmospheric emission in the infrared is both spatially and temporally variable — varying approximately 10% in 10 minutes. Therefore the observing strategy determines how a sky image can be constructed and subtracted from the images. With the quality of the processed images being completely dominated by how this subtraction is done, our program imaged an equal number of sky frames off-target, as science frames on-target in order to minimize the effects of the sky in our photometry. We also chose a large dither pattern in order to remove bad pixels when median combining the frames.

Once observed, images were pre-processed at CFHT using the WIRCam pipeline. This included flat fielding, bias and dark subtraction, as well as the sky-subtraction. Upon receiving the pre-processed images, we median stacked them in groups according to exposure time. This was done both to increase the signal to noise ratio and to remove bad pixels.

2.2.2 Instrumental Photometry

Instrumental magnitudes for all stars were obtained by using point spread function (PSF) modeling and fitting techniques in the DAOPHOT/ALLSTAR packages written by Peter Stetson (Stetson 1987). In overview, these programs work by detecting

Cluster	Exposure time in J (sec)	Exposure time in K (sec)
M15	4761	1913
M92	5765	2112
M13	3029	1112
M71	221	111
NGC 6791	251	109

Table 2.1 Total exposure times in seconds for our CFHT observations in J and K. A near equal amount of time was observed off sky in order to have adequate sky subtraction.

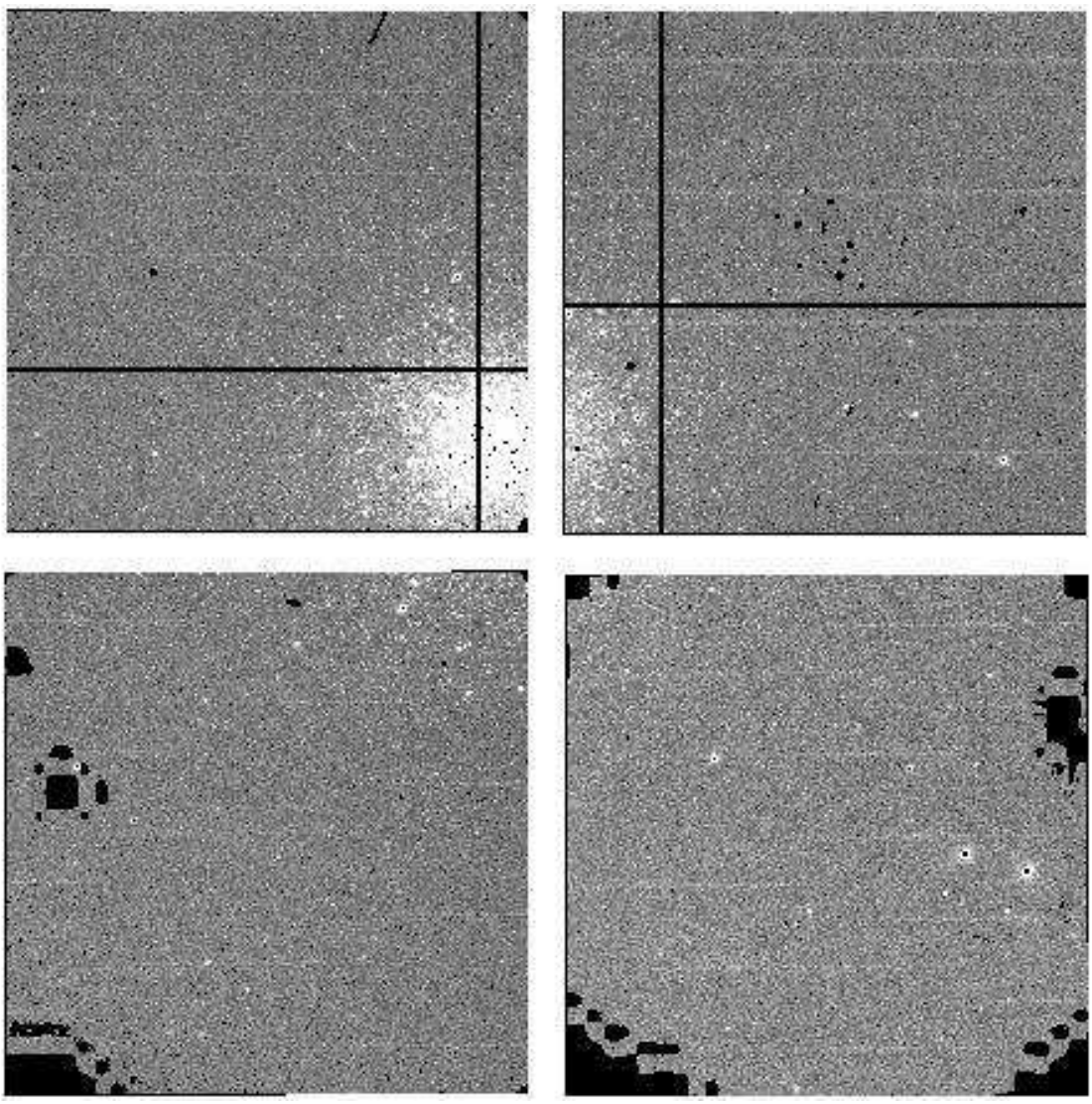

Figure 2.1 CFHT WIRCam J image of M13 showing our observed field with the 4 chips before stacking. Black areas are bad pixel regions which were removed by median-stacking all images.

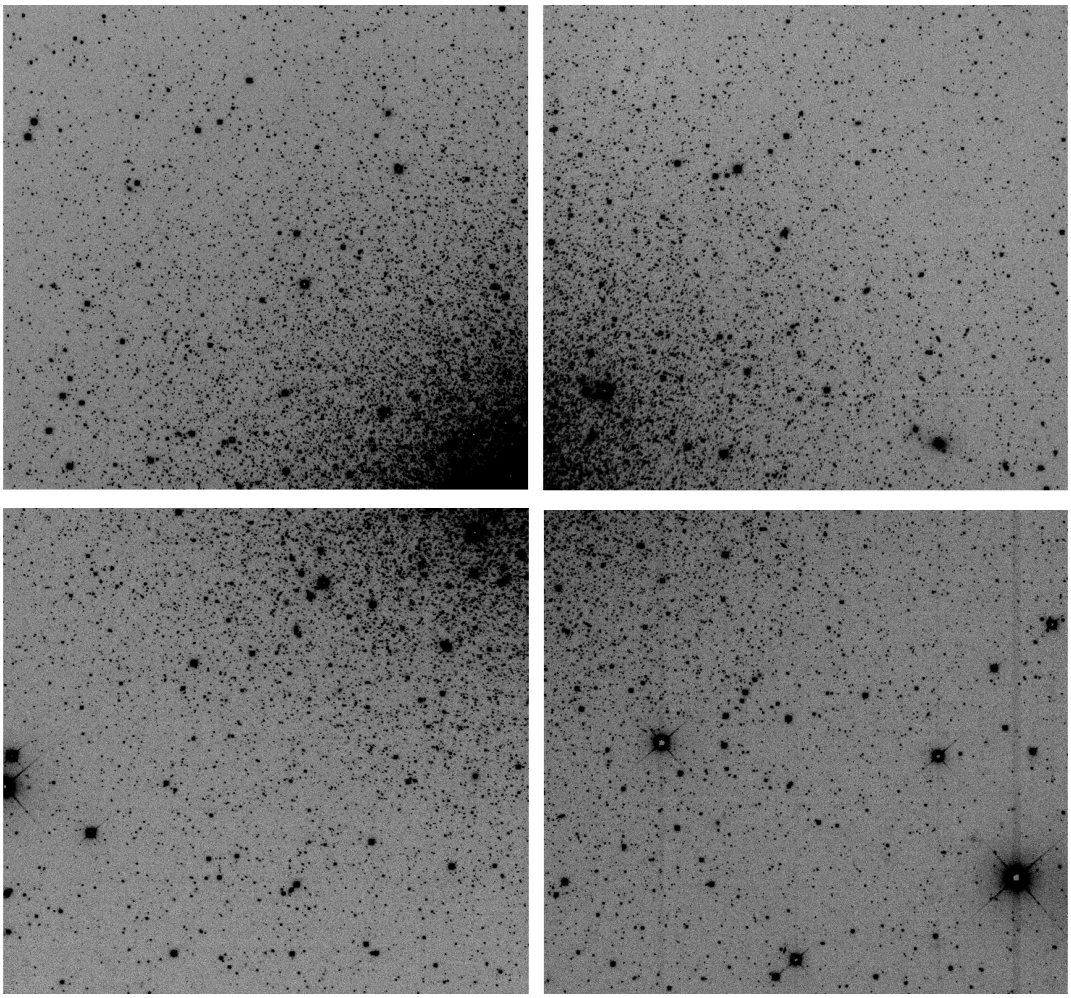

Figure 2.2 One of the Final stacked images of M13 which was used for the J photometry.

stars on a specific image, building a PSF model from a few isolated, bright stars and then subtracting this PSF model from all stars detected. For a more detailed description on how these programs work, see Stetson (1987 and references therein).

Due to the large number of fields, a shell script was developed which executed DAOPHOT/ALLSTAR on each frame separately. Since PSFs are crucial for accurate subtraction, these were always built interactively. Once frames were run through ALLSTAR each star-subtracted image was visually inspected to ensure an accurate PSF model was constructed, and that all usable stars were found and subtracted.

2.2.3 Astrometry

Up to this point in the processing of images, the positions of each star have been defined in CCD (x,y) coordinates measured relative to the bottom left corner of the image. This coordinate system has suited our purposes so far, but we want to be able to compare observations of stars taken using different telescope pointings and different CCDs, which have different (x,y) positions for the same star. Therefore, we want to transform all the CCD-based (x,y) coordinates to a standard coordinate system. For this purpose, we chose the USNO guide star catalog (Monet et al. 2003).

DAOMATCH was used to find initial positional transformations which solve for offset, scale, and rotational differences between the CCD based coordinate system and the USNO system. These initial transformations are then fed through DAOMASTER to improve their precision and accuracy by employing a a set of higher order polynomials that account for effects due to optical distortions, filter induced scale differences, and/or differential refraction in the CCD images. These transformations are iterated upon with a matching tolerance gradually decreased until convergence is reached; then a master list for all stars in the cluster is constructed which gives the raw magnitudes of each star as measured in each frame.

2.2.4 Photometric Calibrations

The most crucial step in accurate cluster photometry is the calibration of the observed instrumental magnitudes into a standard photometric system. To do this in the near-infrared, a number of stars with observed 2MASS J and K magnitudes must be identified in the CFHT frames to use as *standard stars*. Unlike optical photometry, where one would separately observe standard star fields, the 2MASS All-Sky Point Source Catalog contains enough stars in each of our clusters which can be used as

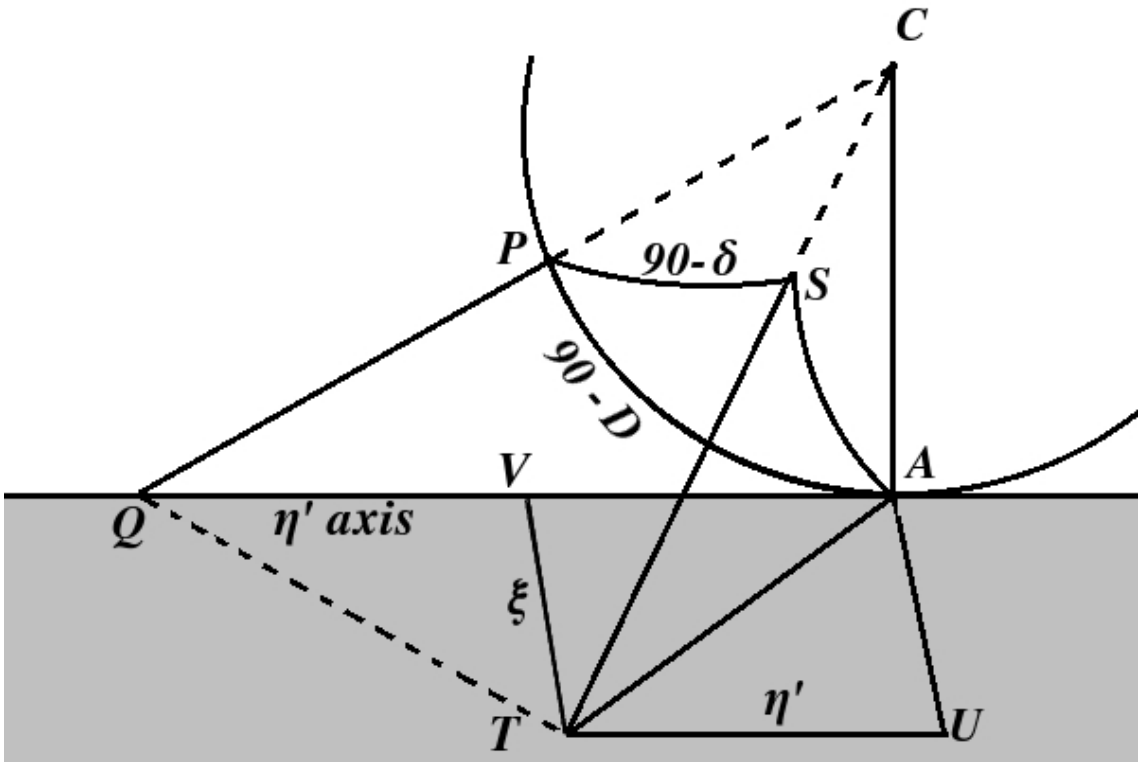

Figure 2.3 Celestial sphere with center, C, and the tangent plane at A, the center of our projection. Star S is projection onto the tangent plane to point T, which is obtained by joining C to S and onto the tangent plane. Adapted from Smart (1965).

standards. For example, M13 has 3221 stars in the 2MASS All-Sky Point Source Catalog within 30 arcmin of its center. Of these, we selected stars with the lowest claimed photometric errors (typically errors < 0.02) for the calibration of our frames.

Before any of the photometric equations can be solved, one must first transform the spherical coordinates (right ascension and declinations) of the 2MASS standard stars, into the x,y coordinate system of our CFHT frames. This is done by projecting the right ascension (α) and declination (δ) of each observed star onto a standard flat coordinate system in (ξ, η) shown schematically in Figure 2.3. This shows the celestial sphere with center, C, and the tangent plane at A, the center of our projection. Star S is projected onto the tangent plane to point T, which is obtained by joining C to S and onto the tangent plane. Point P in the same figure is the north celestial pole, and therefore AP is the meridian of A and it projects a straight line onto the tangent plane AQ. We then define AQ as the η'-axis of the tangent plane. The ξ'-axis is taken

to be AU, which is drawn perpendicular to AQ. Defining (A,D) as the right ascension and declination, respectively, of the point A which is the center of our projection, we can obtain equations for the standard ξ and η based on the spherical coordinates of our both our projection center (A,D) and our star (α,δ):

$$\xi = \frac{sin(\alpha - A)/tan\delta}{sinD + cosDcos(\alpha - A)/tan\delta} = \frac{sin(\alpha - A)}{sinDtan\delta + cosDcos(\alpha - A)} \tag{2.1}$$

and

$$\eta = \frac{cosD - sinDcos(\alpha - A)/tan\delta}{sinD + cosDcos(\alpha - A)/tan\delta} = \frac{cosDtan\delta - sinDcos(\alpha - A)}{sinDtan\delta + cosDcos(\alpha - A)}. \tag{2.2}$$

Finally, a correction is applied to ξ and η, since a distortion arises as a star approaches 90 degrees from the center of the celestial sphere. This is found by calculating ρ, the length of the line connecting TA. Both our η and ξ are multiplied by $\rho/tan\rho$. This is 1 at small values of ρ (i.e. small distance from A), and goes to 0 as ρ approaches $\pi/2$.

Our final x and y coordinates then become:

$$X = \frac{\rho}{tan\rho}\xi \tag{2.3}$$

$$Y = \frac{\rho}{tan\rho}\eta \tag{2.4}$$

where ρ is given as:

$$\rho = \sqrt{\xi^2 + \eta^2} \tag{2.5}$$

Once the 2MASS stars are transformed into the same X and Y coordinate system as our CFHT data, we can then proceed with the standardization of our instrumental magnitudes. This is done by using the 2MASS data as our standard library and then using DAOMASTER to select our J and K photometry of the same stars measured in our CFHT frames.

Since our cluster field contains thousands of stars, we initially transform 100 or so into the standard system so that they can serve as local zero-point standards (see Stetson and Harris 1988 for a description on local secondary standards). This is accomplished via a program called COLLECT which generates a .obs file.

Next we use CCDSTD which takes the observed instrumental magnitudes for standard stars from the file created by COLLECT, collects the standard photometric indices for the same stars from the standard library file of 2MASS stars, and transforms the former into the system of the latter, by least-squares computation of the transformation and extinction coefficients.

CCDAVE takes all available observations of each star and computes the best average photometric indices on the standard system using the coefficients from CCDSTD. The output of CCDAVE produces a .net file which contains the final photometry of all stars which were in the .obs files from COLLECT.

Since we want to calibrate all the stars in our cluster the final step is to run the program NEWTRIAL. NEWTRIAL takes the standard 2MASS photometry of the local standards and the calibration equations generated by CCDSTD to compute new photometric zero-points for each frame.

2.2.5 Photometric Consistency

One can check the overall quality of our transformed magnitudes by comparing stars in common between our fields and the 2MASS catalog. Such comparisons for each cluster are shown in Figures 2.5-2.12 where the differences between the standard 2MASS magnitudes and our final calibrated ones are plotted against both magnitude and colour. The range of magnitudes plotted are based on the photometric limits of 2MASS at the faint end, and the saturation limit of our observations at the bright end (indicated by the axis of each plot). 2MASS has a photometric sensitivity of 10-sigma at J= 15.8 and K= 14.3 mag, and when defining the calibration stars we did not use stars below these values, with the exception of M13, for which, due to lack of giant stars in our frames, we had to use K magnitudes down to 15 mag. The saturation limit of our observations was dependent on the seeing during the night each cluster was observed. Only stars fainter than the magnitude at which WIRCam began responding non-linearly were used for calibration purposes.

Reassuringly, the horizontal lines corresponding to zero difference appear to pass through the densest concentration of points in all plots. Moreover, there seem to be no strong systematic trends as a function of colour that would indicate the need for additional colour terms in the photometric solutions.

2.2.6 Photometric Accuracy

The accuracy of the photometry is a function of magnitude: errors are lowest for the brightest objects and they increase for fainter objects where photon counting begins to dominate over systematic errors. We provide an example of how the accuracy varies as a function of magnitude for NGC6791 in Figure 2.13. This figure plots the J band photometric error, σ_J, against V-band magnitude to compare with the $(V-J)$-M_V colour-magnitude diagram in Figure 3.2: photometry of stars from 2MASS which are brighter than V=17.5 (indicated by the solid black line in Figure 2.13) are plotted in the colour magnitude diagram in Figure 3.2, and stars fainter than this limit are taken from our CFHT photometry. The photometry is at the 2% level for stars brighter than V=18.25, and we plot the CMDs to a V magnitude of 20, where the photometric errors are 10%. All of our CMDs were plotted to a photometric accuracy of 10 %, and all bright stars are at the 2% level.

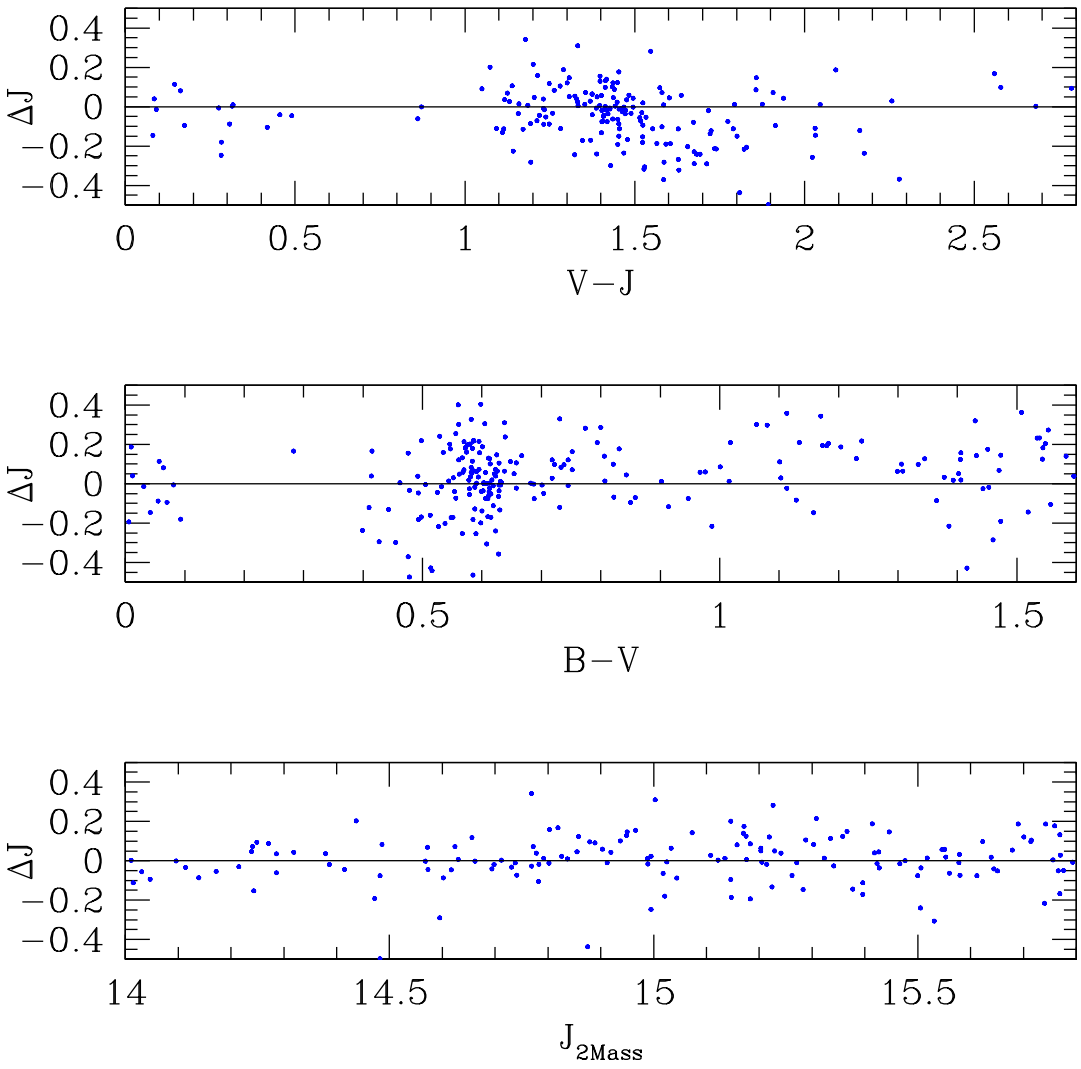

Figure 2.4 J-band photometric differences for stars observed in both 2MASS and our CFHT fields for M92.

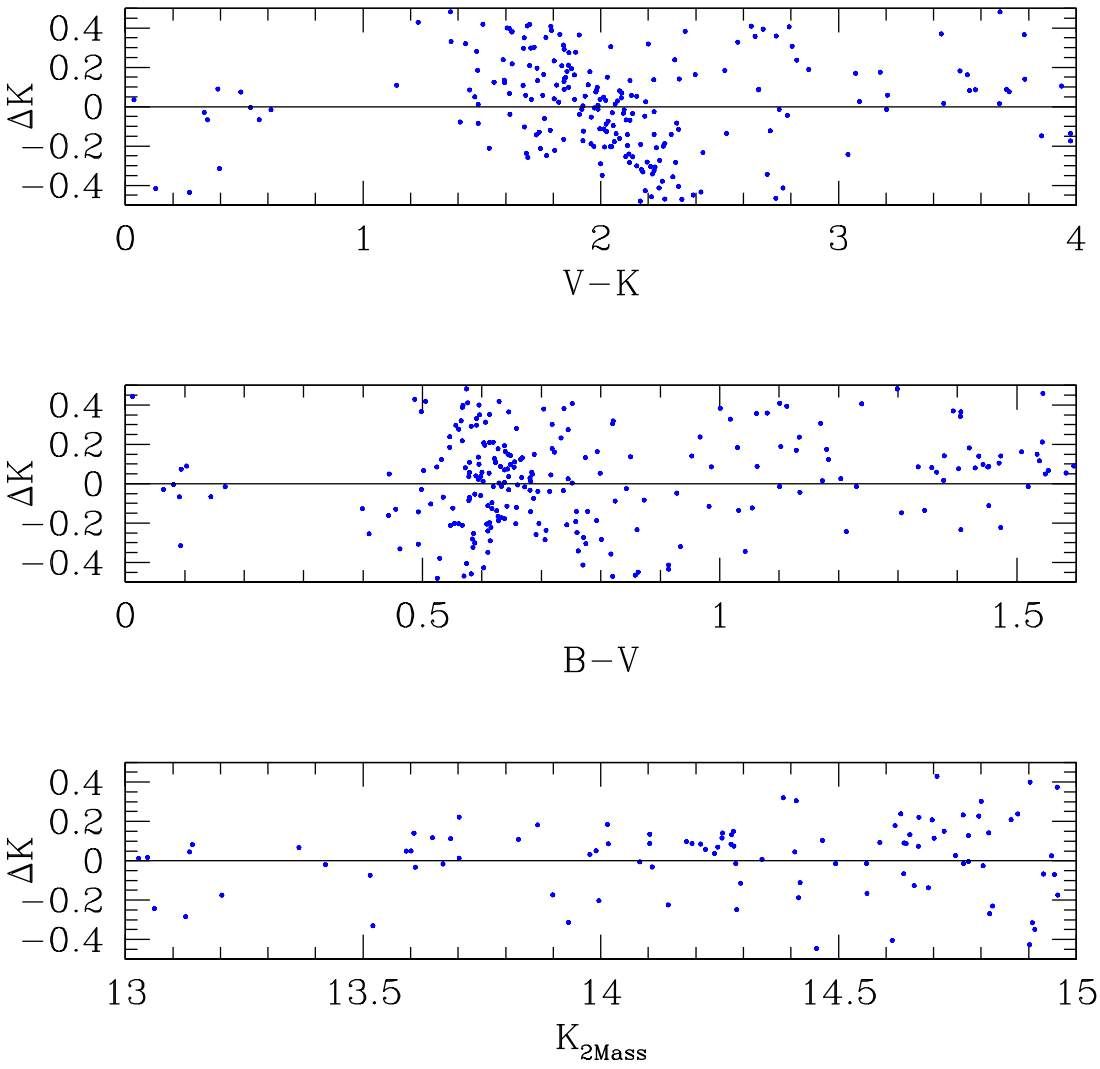

Figure 2.5 *K*-band photometric differences for stars observed in both 2MASS and our CFHT fields for M92.

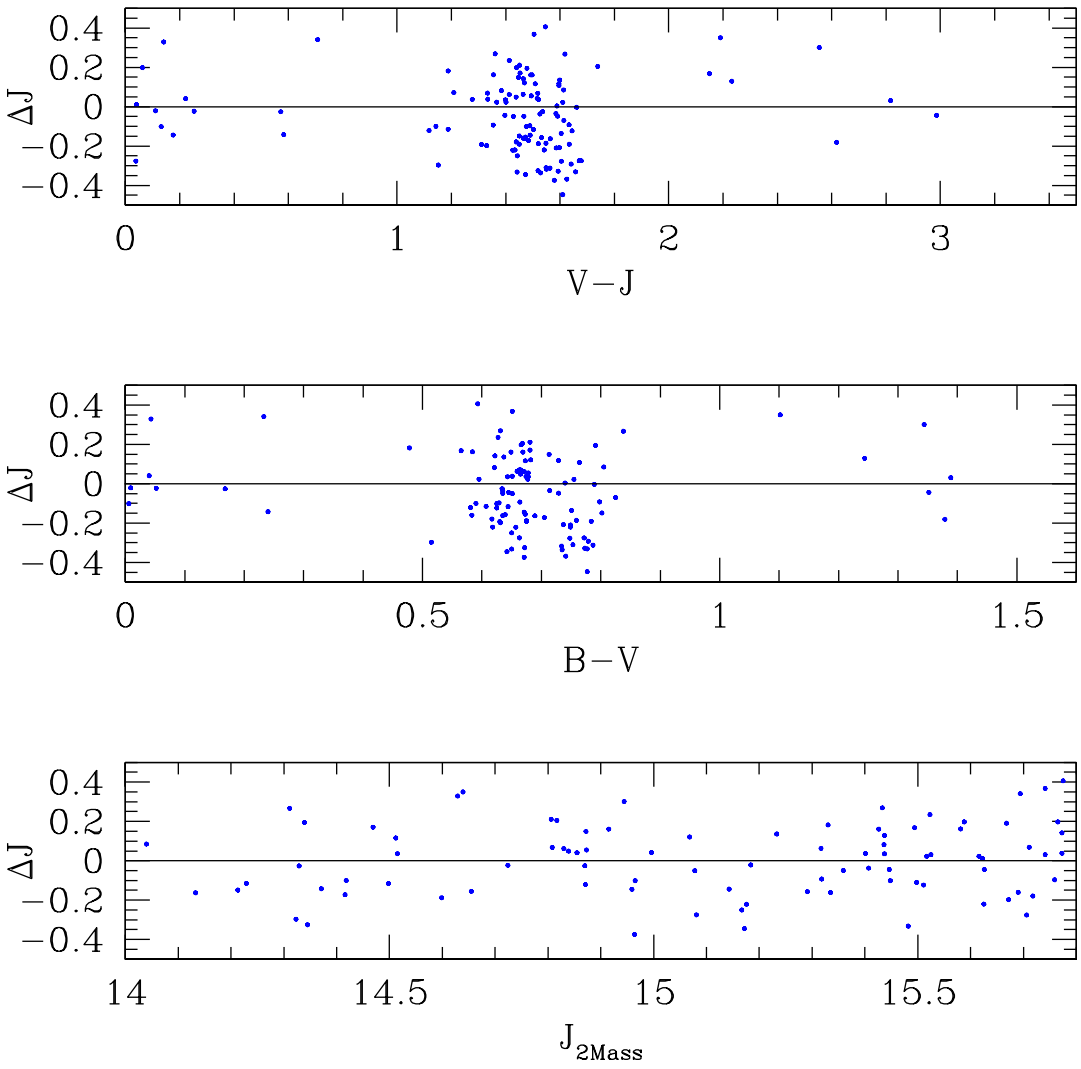

Figure 2.6 J-band photometric differences for stars observed in both 2MASS and our CFHT fields for M13.

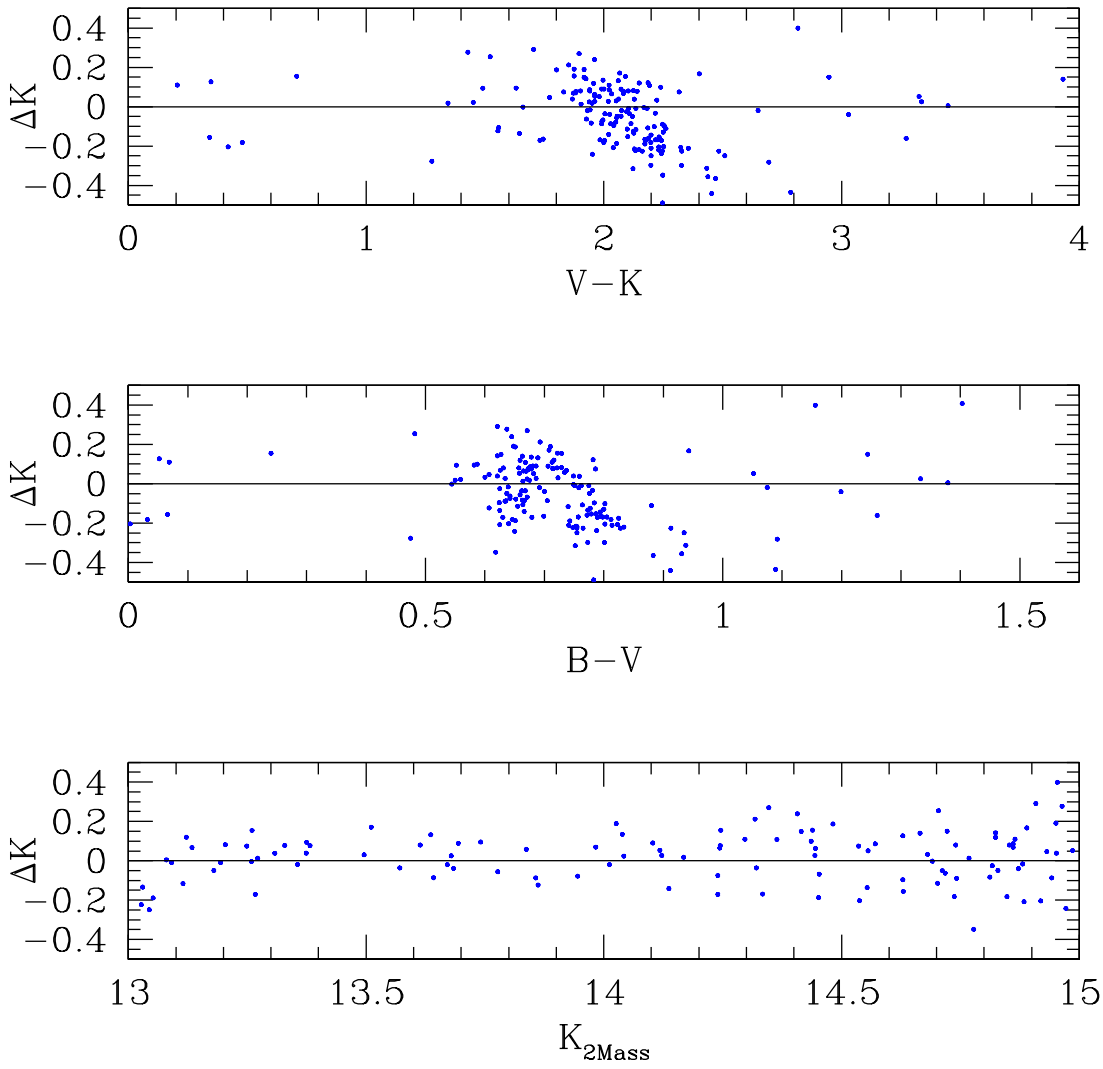

Figure 2.7 *K*-band photometric differences for stars observed in both 2MASS and our CFHT fields for M13.

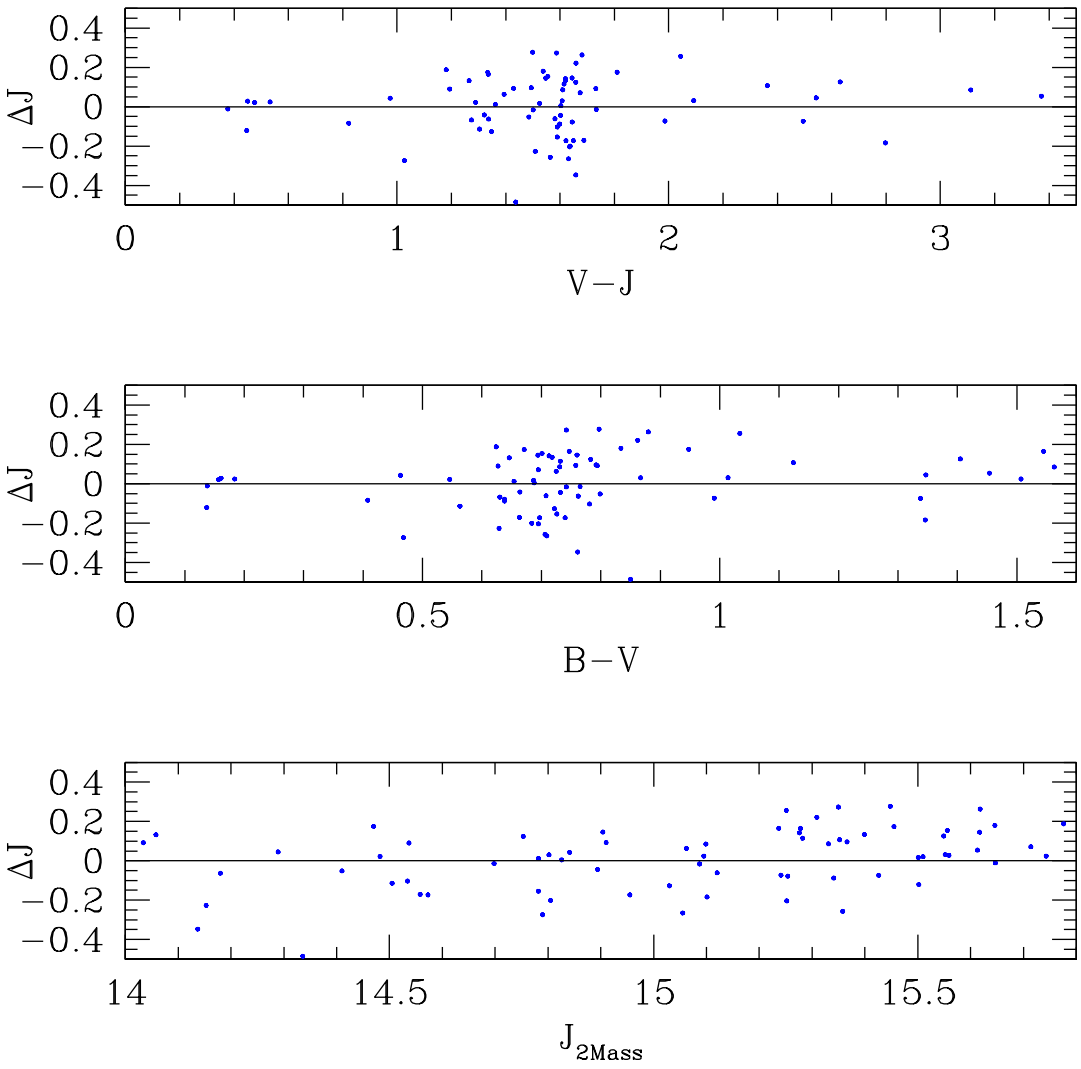

Figure 2.8 J-band photometric differences for stars observed in both 2MASS and our CFHT fields for M15.

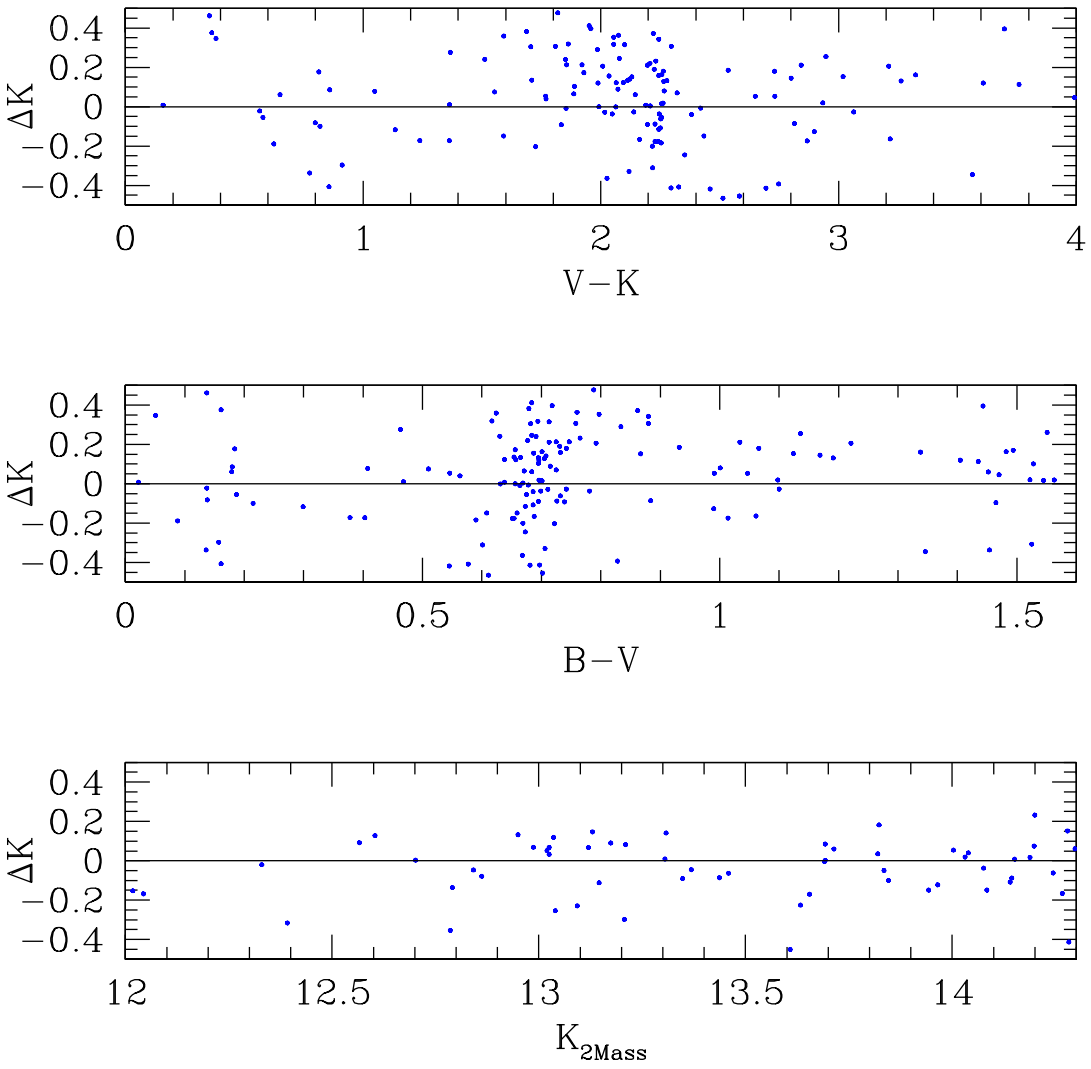

Figure 2.9 *K*-band photometric differences for stars observed in both 2MASS and our CFHT fields for M15.

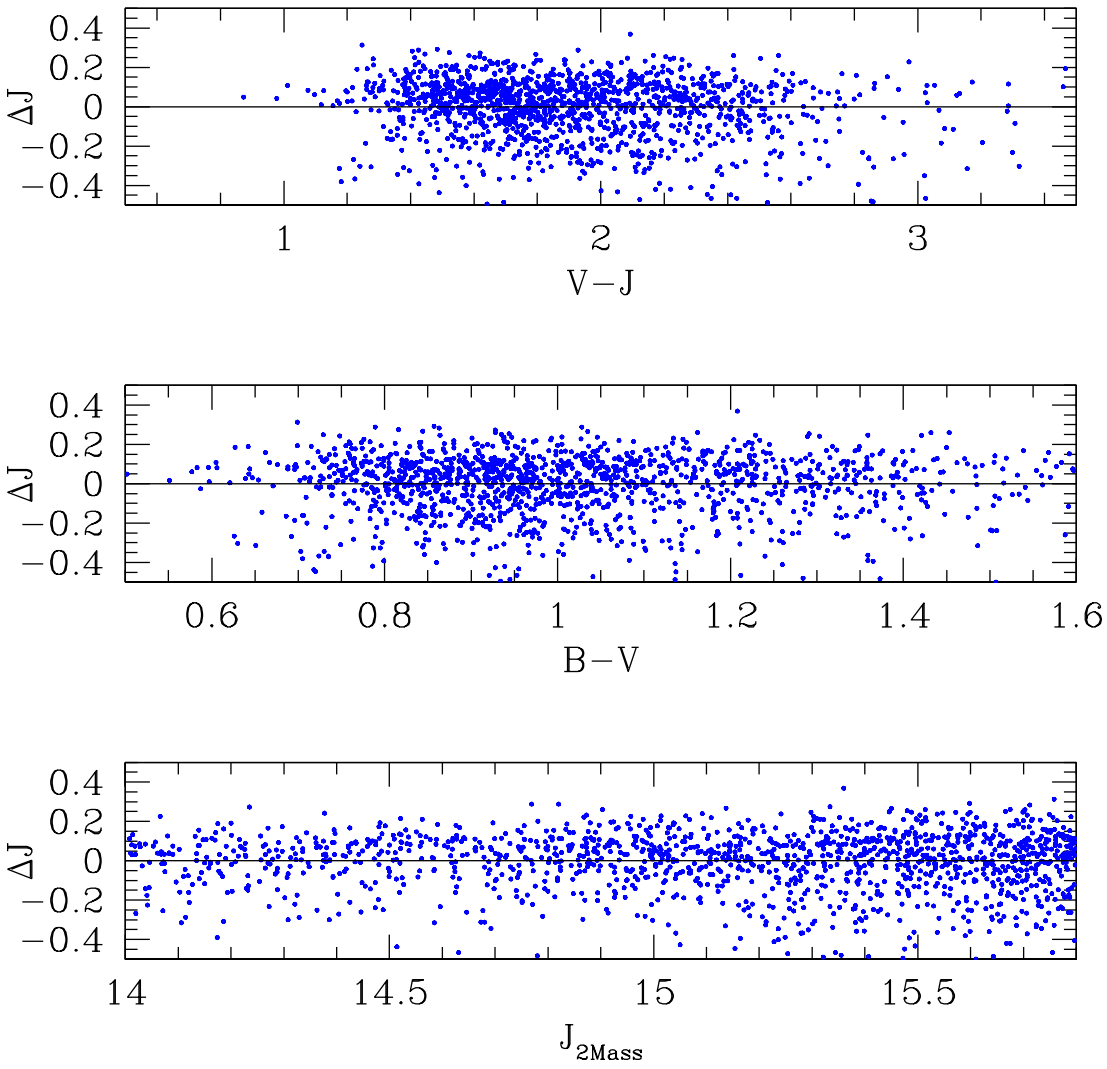

Figure 2.10 J-band photometric differences for stars observed in both 2MASS and our CFHT fields for M71.

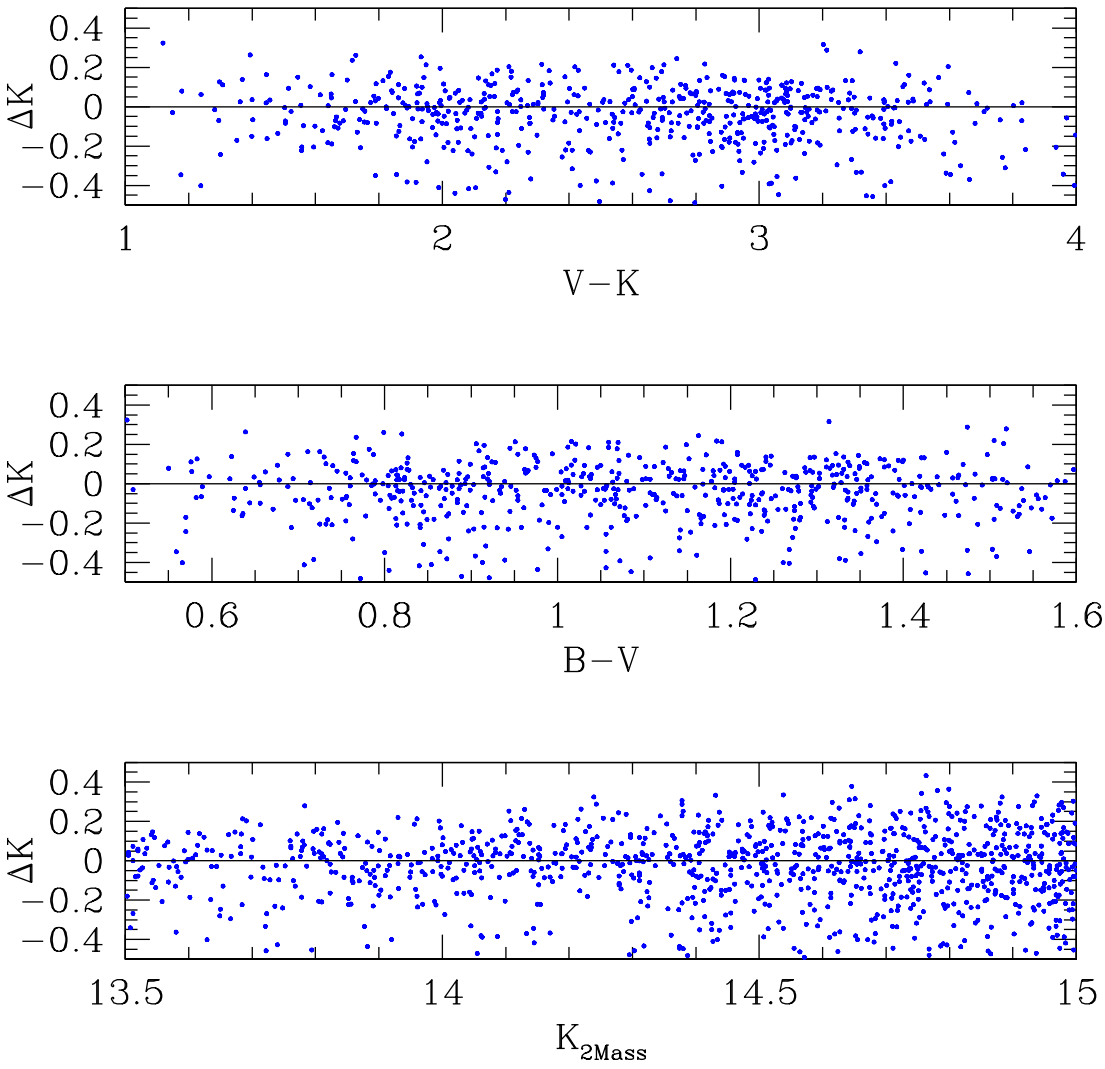

Figure 2.11 K-band photometric differences for stars observed in both 2MASS and our CFHT fields for M71.

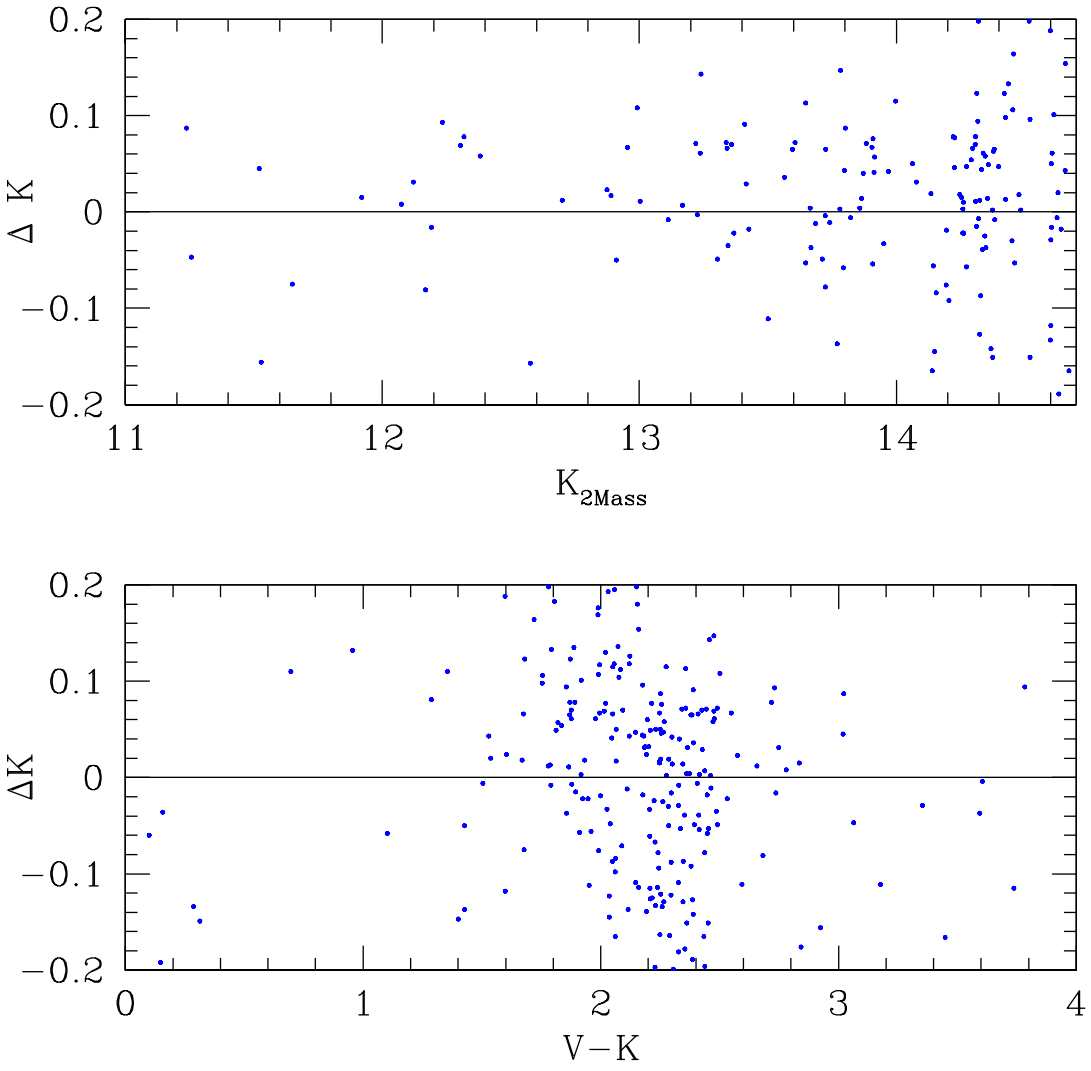

Figure 2.12 *K*-band photometric differences for stars observed in both 2MASS and our VLT fields for NGC 1851.

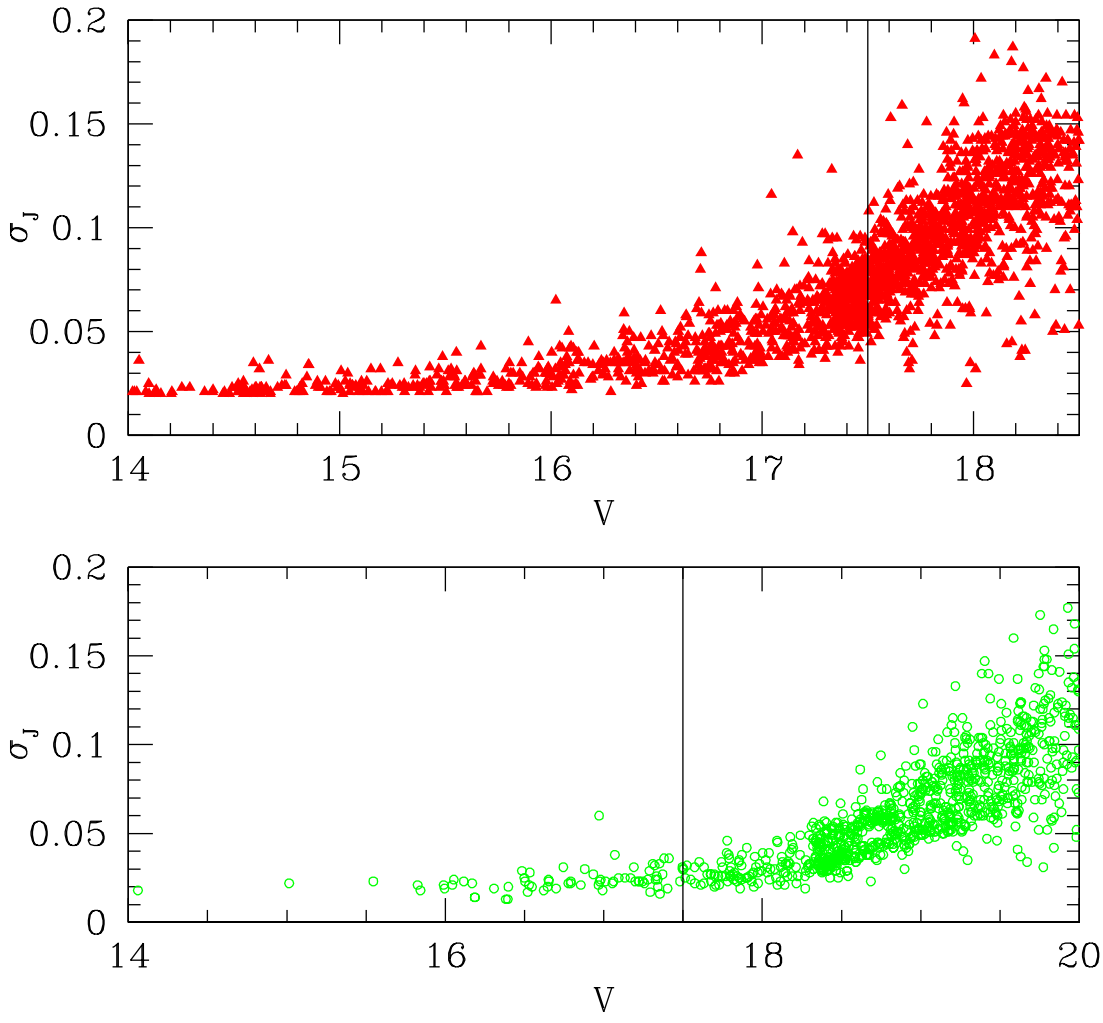

Figure 2.13 J-band photometric error as a function of magnitude for NGC6791 for the 2MASS photometry (upper panel) and the CFHT photometry (lower panel).

Chapter 3

The Colour-Magnitude Diagrams and Fiducials

3.1 Introduction

Spanning the large distribution in metallicity from [Fe/H]= -2.4 to $+0.3$, the fiducial sequences of NGC6791, M71, NGC1851, M13, M15 and M92 presented in this chapter serve as a set of empirical isochrones which can be used as calibrators for stellar evolutionary models, and as tests of the colour-$T_{\rm eff}$ relations that transform theoretical stellar temperatures to the observed colour planes.

To produce the CMDs from which these fiducial sequences were derived, our final photometry of each cluster was combined with V-band data provided by Peter Stetson to generate $(V-J)$-V and $(V-K)$-V CMDs. Our CMD of NGC1851, which is from VLT observations, extends from the RGB tip to $\sim$ 3 magnitudes below the main sequence turn-off. For our remaining five clusters, which were observed using CFHT, we were able to obtain only observations for magnitudes fainter than the base of the RGB. Despite observing these clusters with the shortest exposures possible on WIRCam, the upper giant branch stars were saturated in all of our frames. This was due in part to the seeing being 0.3 to 0.5 arcseconds better than we had requested during the nights of observation, and therefore resulted in a more concentrated PSF.

Thus, in order to populate the RGBs of our CFHT clusters, we queried the 2MASS catalog for all stars observed within 30 arcmin of the center of each cluster. With a photometric sensitivity of 10 sigma at J= 15.8 and K_S= 14.3 mag, 2MASS observations extend to the base of the giant branch for each of our target clusters. The

Cluster	Type	α	δ	[Fe/H]	(m-M)$_V$	E($B-V$)
M15	globular	21:29:58	+12:10:01	−2.42	15.37	0.075
M92	globular	17:17:07	+43:08:12	−2.38	14.67	0.023
M13	globular	16:41:41	+36:27:37	−1.60	14.48	0.016
NGC 1851	globular	05 14 06	- 40 02 50	−1.36	15.51	0.037
M71	globular	19:53:46	+18:46:42	−0.74	13.79	0.220
NGC 6791	open	19:20:53	+37:46:30	+0.3	13.55	0.155

Table 3.1 Properties of Galactic star clusters in our survey. [Fe/H] values for the globular clusters M15, M92, M13 and M71 are from Kraft and Ivans (2003). For NGC1851, the Zinn and West (1984) [Fe/H] value is given. In the case of the open cluster NGC6791, we adopted the latest [Fe/H] estimate from Boesgaard et al. (2009). Adopted reddenings are those estimated by Schlegel et al. (1998) except for the historically controversial value for M15 and the highly reddened disc cluster M71 (see the text for further discussion about these clusters). Refer to the text for sources of distance moduli.

2MASS photometry for giant branch stars in each cluster was then combined with Peter Stetson's V band photometry.

Although it is ideal to have homogeneous observations for the entire range in cluster magnitude, the zero points of our WIRCam photometry were set using 2MASS observations from the same catalog which we used to populate the giant branches. Therefore in principle one should expect no differences between these observations. However, in practice one needs to keep in mind uncertainties in the zero-points when employing the resulting colour-magnitude diagrams and fiducials (see Chapter 2 for further details).

We present our observed colour-magnitude diagrams in Figures 3.1 - 3.6 with 2MASS photometry plotted in red, CFHT/WIRCam photometry plotted in green, and VLT/HAWK-I photometry plotted in blue. When mapping this photometry to the absolute $(V-K)_0$-M_V and $(V-J)_0$-M_V planes for comparisons with isochrones, the reddening values and distance moduli given in Table 3.1 were adopted. The following sections provide a brief discussion on the choice of adopted distance moduli.

3.1.1 NGC6791

As the most-metal rich target in our sample, the open cluster NGC6791 provides an important test for both stellar evolutionary models and colour-$T_{\rm eff}$ relations at high metallicities. While K-band observations for this cluster were not obtained due to poor weather conditions, we present our $(V-J)$-V CMD of this cluster in Figure

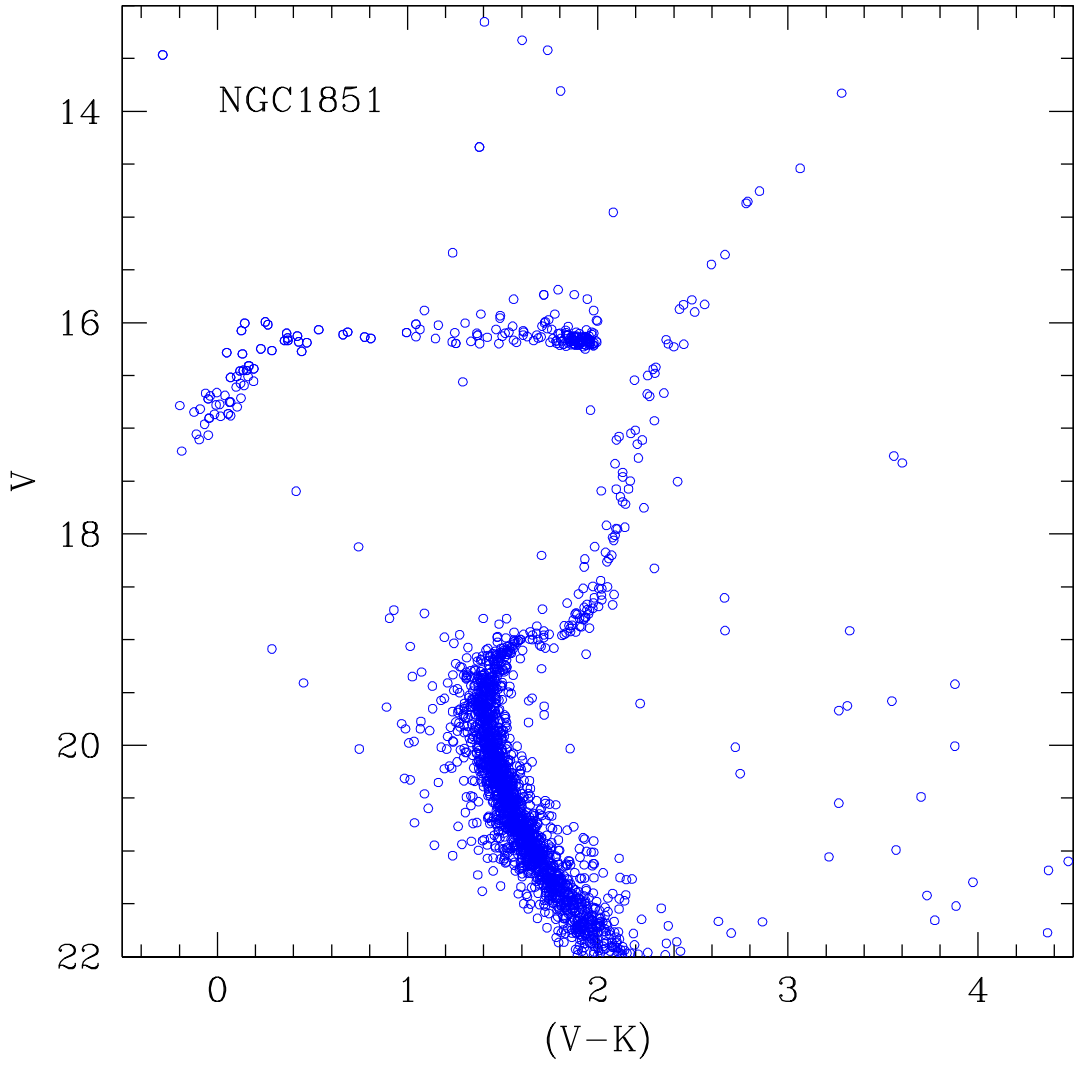

Figure 3.1 NGC 1851 M_V-$(V-K)_0$ CMD from VLT HAWK-I data. The data, provided by our Italian collaborators, was combined with optical photometry provided by Peter Stetson.

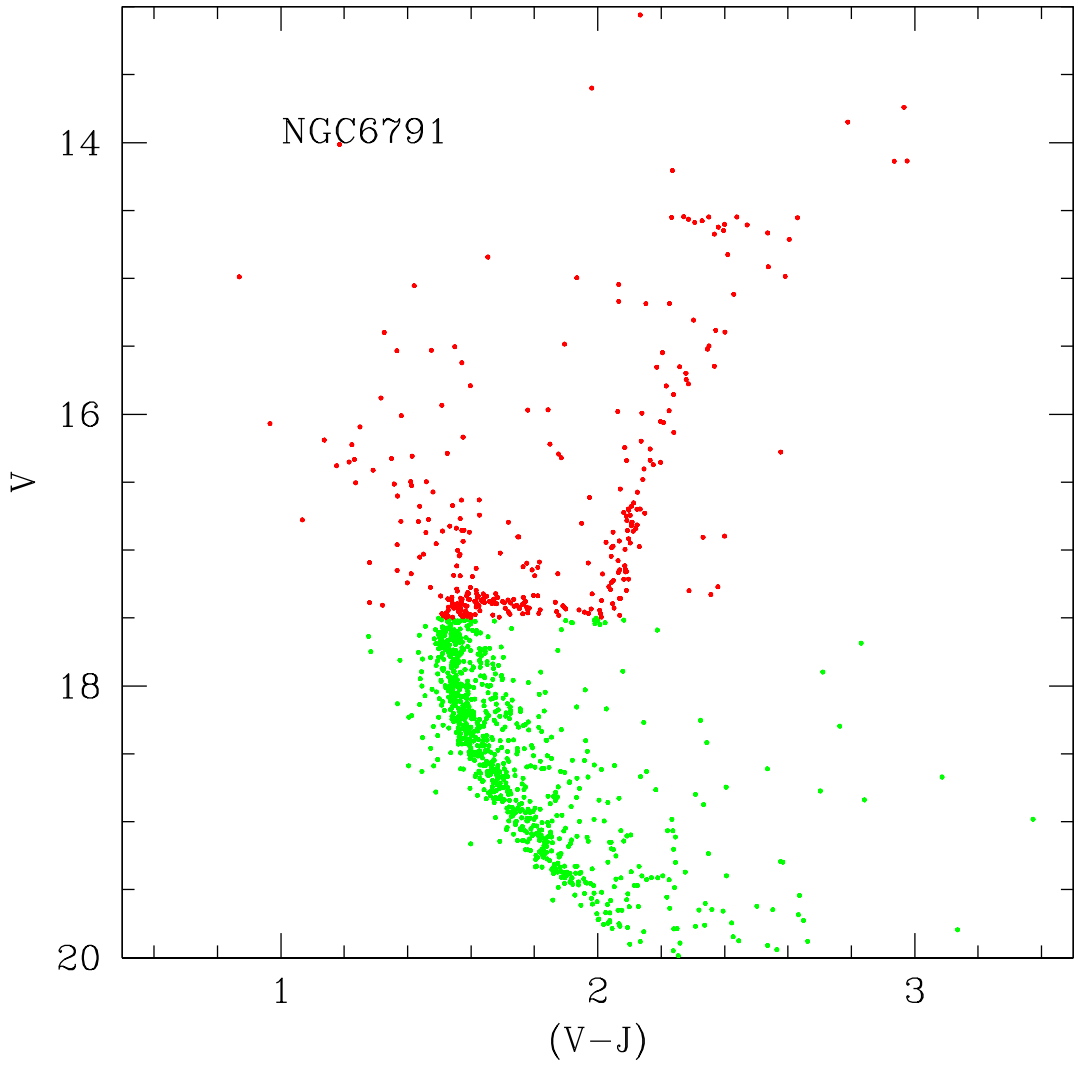

Figure 3.2 NGC6791 M_V-$(V-J)$ CMDs. Our CFHT/WIRCam data is plotted in green and 2MASS observations are shown in red. The colour indices were derived using Peter Stetson's V photometry. Only J photometry was obtained with CFHT for this cluster.

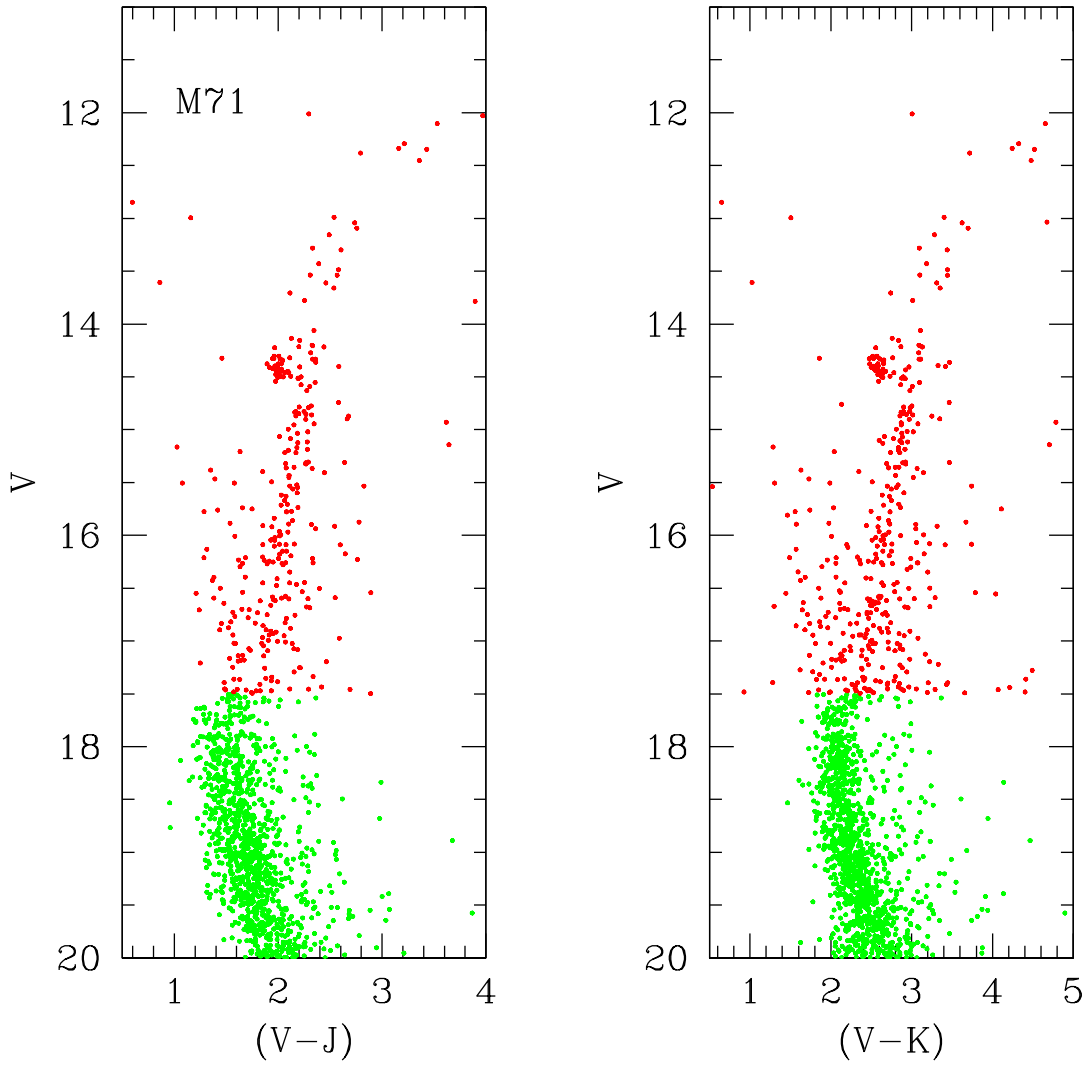

Figure 3.3 M71 $(V-J)$ and $(V-K)$ CMDs. J and K photometry is from CFHT/WIRCam (green points) and 2MASS (red points) and combined with Peter Stetson's V photometry.

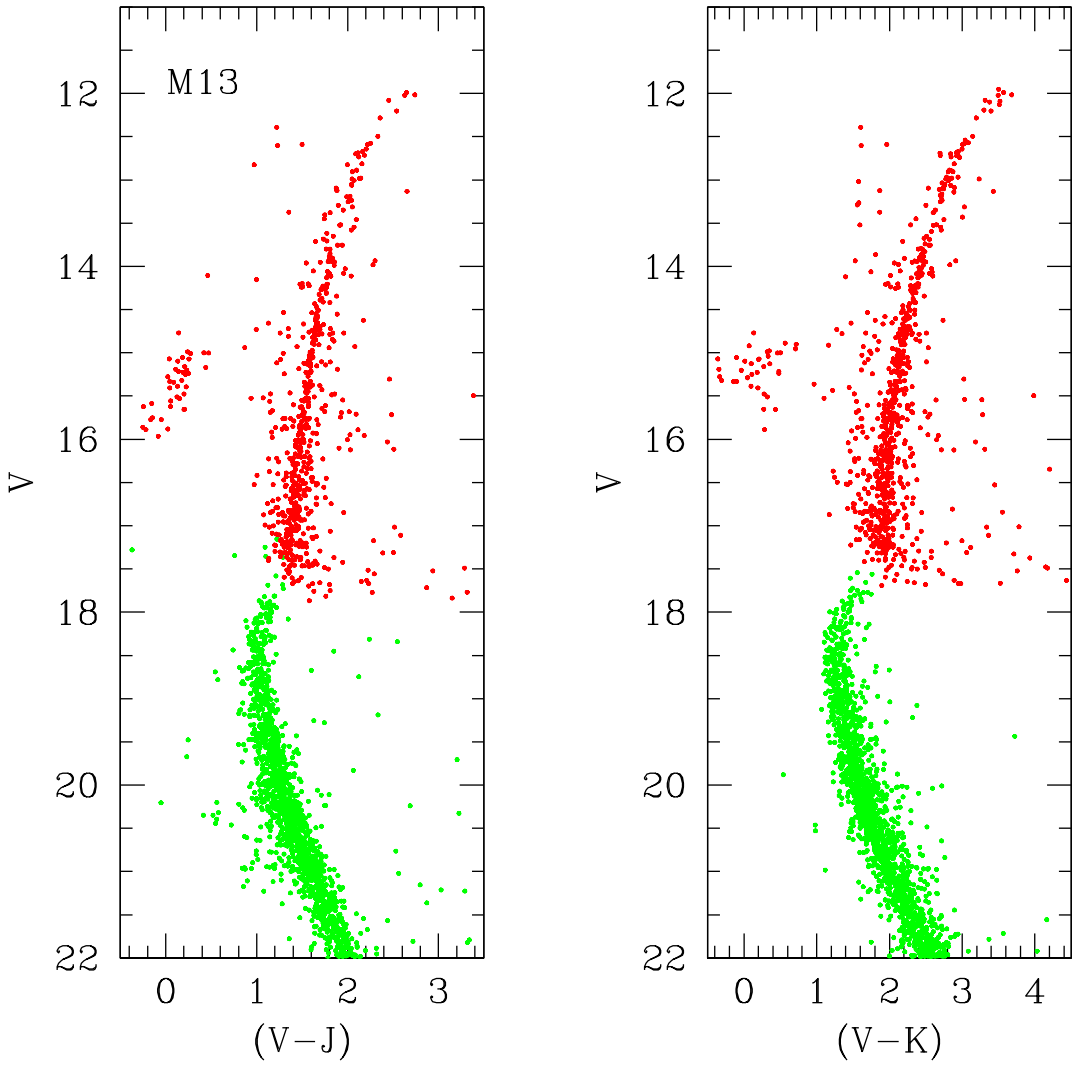

Figure 3.4 M13 $(V-J)$ and $(V-K)$ CMDs. J and K photometry is from CFHT/WIRCam (green points) and 2MASS (red points) and combined with Peter Stetson's V photometry.

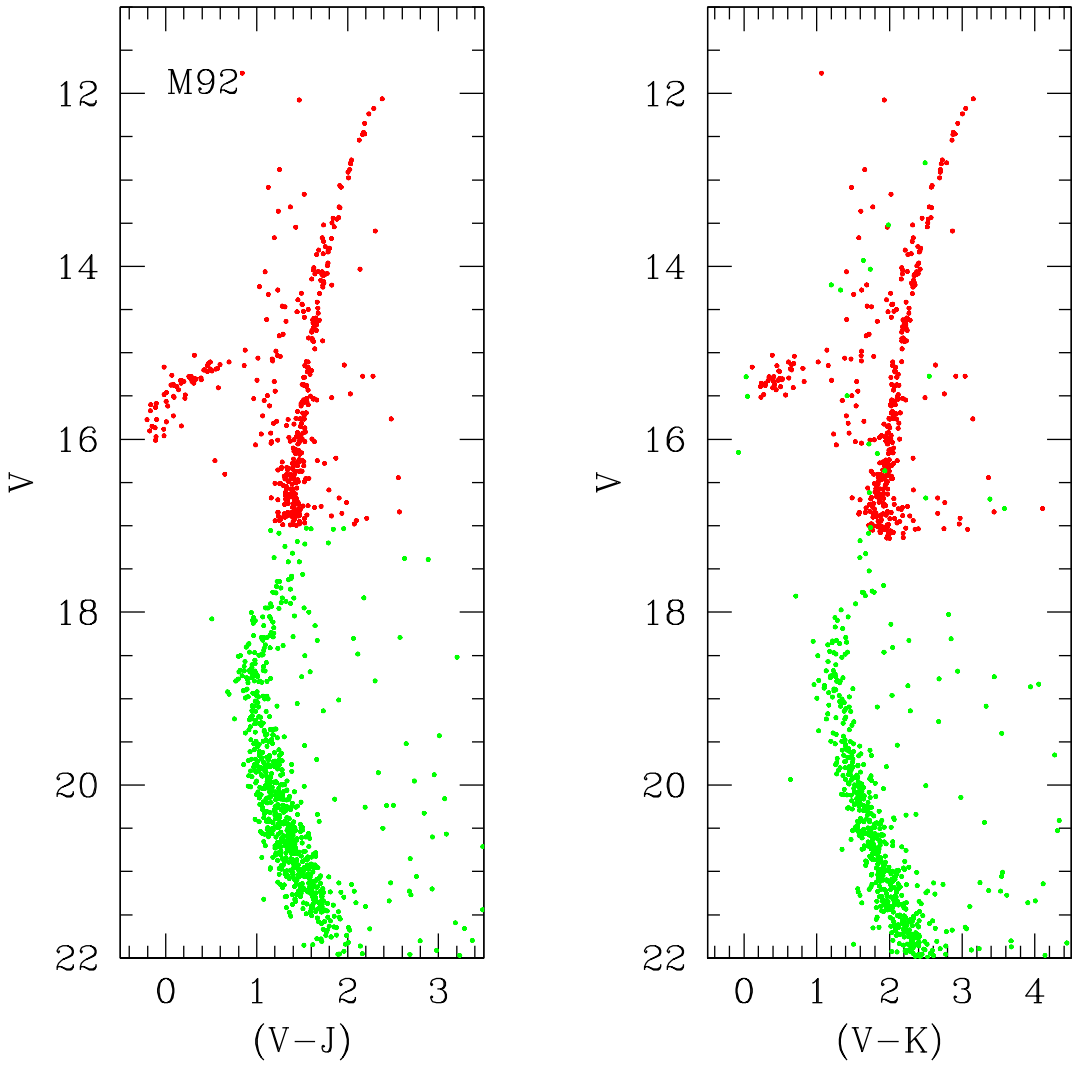

Figure 3.5 M92 $(V-J)$ and $(V-K)$ CMDs. J and K photometry is from CFHT/WIRCam (green points) and 2MASS (red points) and combined with Peter Stetson's V photometry.

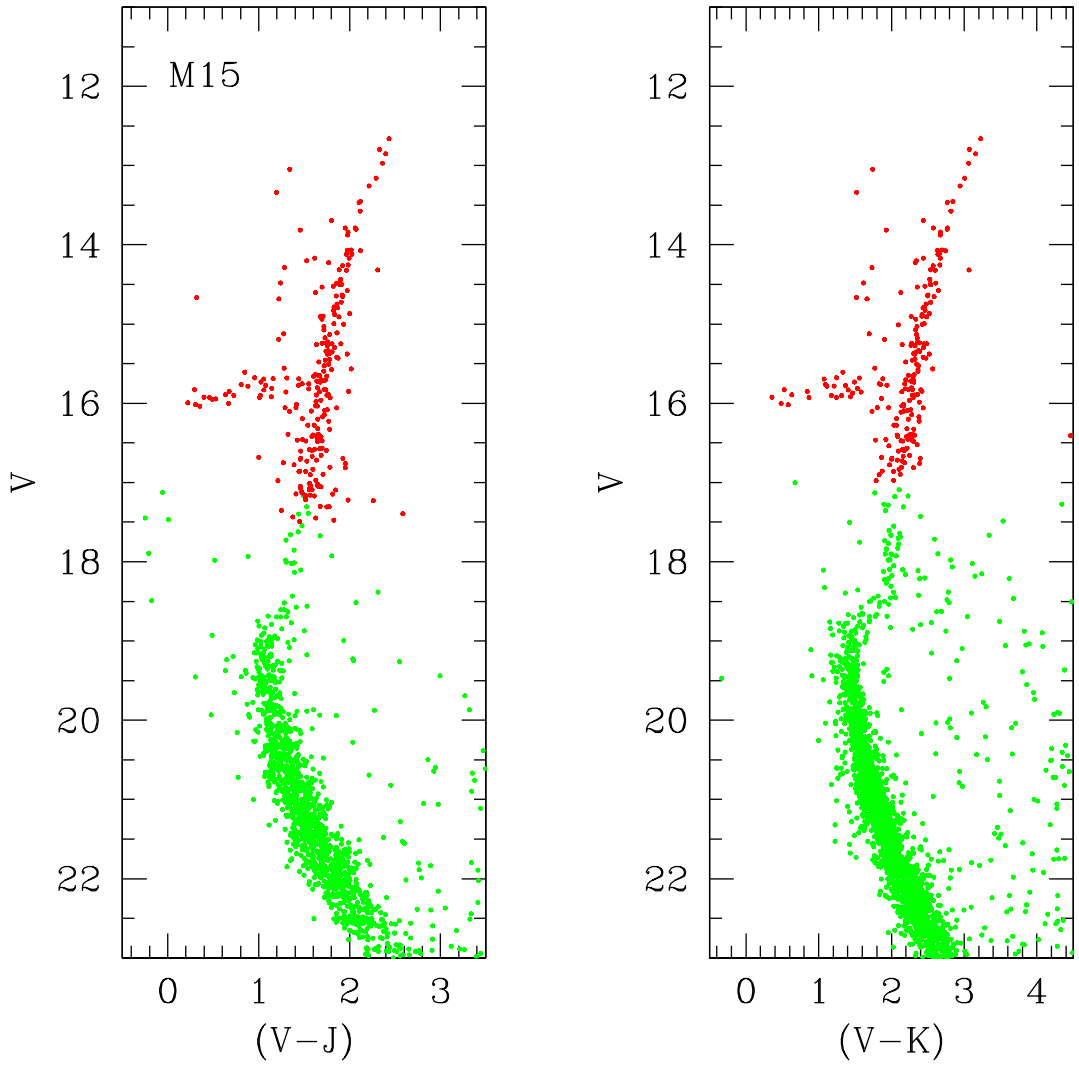

Figure 3.6 M15 $(V-J)$ and $(V-K)$ CMDs. J and K photometry is from CFHT/WIRCam (green points) and 2MASS (red points) and combined with Peter Stetson's V photometry.

3.2. When making comparisons of the CMD of NGC6791 with theoretical isochrones, we adopt the distance modulus of (m-M)$_V$=13.55 derived by Sandage, Lubin, and VandenBerg (2003).

3.1.2 M71

M71 represents the metal-rich end of our sample of globular clusters. The colour-magnitude diagram in Figure 3.3 reflects the low Galactic latitude of this cluster: contamination from field stars is inevitable even after plotting only those stars contained within a small radius of the cluster center. Furthermore, the Schlegel et al. (1998) maps reveal that the reddening is differential across the cluster, contributing to the spread in colour at any given magnitude and hindering the definition of tight sequences for this cluster in any photometric band. When comparing the CMDs to isochrones, we use an apparent distance modulus of (m-M)$_V$ =14.48 for M71 from mean horizontal branch luminosity determination by Harris (1996).

3.1.3 NGC1851 and M13

Together, NGC1851 and M13 fill in the intermediate metallicity range of our sample, with [Fe/H]= -1.36 and -1.60 respectively. Derived from VLT HAWK-I K band images, Figure 3.1 shows our $(V-K)-V$ CMD of NGC1851. For this cluster we have adopted a distance modulus (m-M)$_V$ = 15.51 derived from the study of its RR Lyrae stars by Cassisi, De Santis and Piersimoni (2001). In the case of M13, we use an apparent distance modulus of (m-M)$_V$ =14.48 as derived by by Harris (1996).

3.1.4 M15 and M92

M15 and M92 constitute the most metal poor clusters in our sample. For M92, Carretta and Gratton (1997) derive [Fe/H]= -2.16 from Fe I lines, while more recently Kraft and Ivans (2003) derive a value of -2.38 from Fe II lines. In the case of M15, Kraft and Ivans (2004) give -2.42 for M15 and Carretta and Gratton (1997) derive -2.12. Three-dimensional model atmosphere work by Collet et al. (2007) shows that Fe II lines should provide the most accurate iron abundance determinant. For this reason, we have adopted the Kraft and Ivans values of [Fe/H]= -2.4 for both M15 and M92.

For distance moduli, we have adopted (m - M)$_V$ = 14.67 for M92 derived by Pont et al. 1998 using Hipparcos subdwarfs, and (m - M)$_V$ = 15.37, for M15 from Harris (1996).

3.2 Reddening Estimates Based on Near-Infrared CMDs

The sensitivity to reddening of a particular band pass is determined by the nature of the interstellar dust. In the Milky Way, reddening decreases towards longer wavelengths as a result of the grain size distribution favoring smaller particles. Therefore near-infrared photometry is less sensitive to interstellar extinction than classical broadband filters at optical wavelengths. For example, McCall et al. (2004) have derived the relationship between total extinction, A_λ and the difference in extinction between B and V, E(B-V) = $A_B - A_V$ for the three filters we are concerned with in this chapter:

$$A_V = 3.07\ E(B-V), \tag{3.1}$$

$$A_J = 0.819\ E(B-V),\ \text{and} \tag{3.2}$$

$$A_K = 0.35\ E(B-V). \tag{3.3}$$

Because of its large span in wavelength, E$(V-K)$ is much larger than E$(B-V)$; to be specific E$(V-K) = A_V - A_K = 2.72$ E$(B-V)$. Therefore when a CMD is transformed from the observed $(V-K)$ to the absolute $(V-K)_0$ colour, small shifts in the adopted reddening become amplified by a factor of nearly 3 relative to the classical $(B-V)$ colour axis. Therefore our $(V-K)$ observations can be used to provide powerful constraints for M15, NGC6791 and the disc cluster M71, which have historically been quite controversial. Knowing precise values for the interstellar reddenings of these clusters has implications for their distance determinations and consequently their ages.

3.2.1 M15

Reddening estimates for M15 range in the literature from ~ 0.07 to ~ 0.15. Sandage, Katem and Sandage (1981) derived E$(B-V)$=0.11, which is consistent with the

Schlegel et al. (1998) value of 0.11 mag. However since the Schlegel et al. maps measure line-of-sight Galactic reddenings, one cannot be certain that the line of sight reddening of M15 is entirely due to foreground material (i.e., background gas/dust may account for some fraction of the Schlegel et al. reddening). In fact, if the higher reddening estimate is adopted, agreement between theory and observations of pulsating stars in M15 cannot be found (Bono et al. 1995). Indeed, the study of RR Lyraes by Cacciari et al. (1984) suggest that E$(B-V) = 0.07$ for M15.

Figure 3.7 demonstrates how an adopted reddening of E$(B-V)$= 0.075 for M15 allows for excellent agreement between the main-sequence of the CMD and Victoria isochrones. To demonstrate that this determination is weakly dependent on the colour-$T_{\rm eff}$ relation used, Victoria isochrones were converted to the $(V-K)_0 - M_V$ plane using both MARCS and PHOENIX transformations. These transformations give nearly identical results, making a strong case for the lower reddening value of M15. Indeed, if a higher reddening were to be adopted it would imply that M15 has a much bluer RGB than M92, despite both clusters having essentially the same metallicity and age.

3.2.2 NGC6791

In consequence of its large distance and low Galactic latitude, reddening estimates of NGC6791 vary considerably in the literature. As discussed by Chaboyer et al. (1999), the derived reddenings for NGC6791 span the range $0.09 \leq$ E$(B-V) \leq 0.26$. Kaluzny & Rucinski (1995) have used subdwarf-B stars to provide a tight constraint on the reddening, finding E$(B-V) = 0.17 \pm 0.01$. This agrees well with the Schlegel et al. (1998) estimate of E$(B-V) = 0.155$ mag, which is also favored by the comparison of the NGC6791 CMD with that for solar neighborhood stars from Hipparcos data (see Sandage, Lubin, and VandenBerg 2003). Indeed, the adoption of (m-M)$_V = 13.55$ and E$(B-V)$= 0.155, as deduced by Sandage et al., results in excellent agreement between our NGC6791 $M_V - (V-J)_0$ CMD and the latest Victoria isochrones (Figure 3.8). Note that our J photometry also provides a strong argument for a high reddening value. Because E$(V-J) = 2.25$ E$(B-V)$, small adjustments in E$(B-V)$ become magnified in the $(V-J) - M_V$ plane. Consequently, consistent fits of isochrones to the $(V-J)_0$-M_V and $(B-V)_0$-M_V planes are obtained only if E$(B-V) \approx 0.155$.

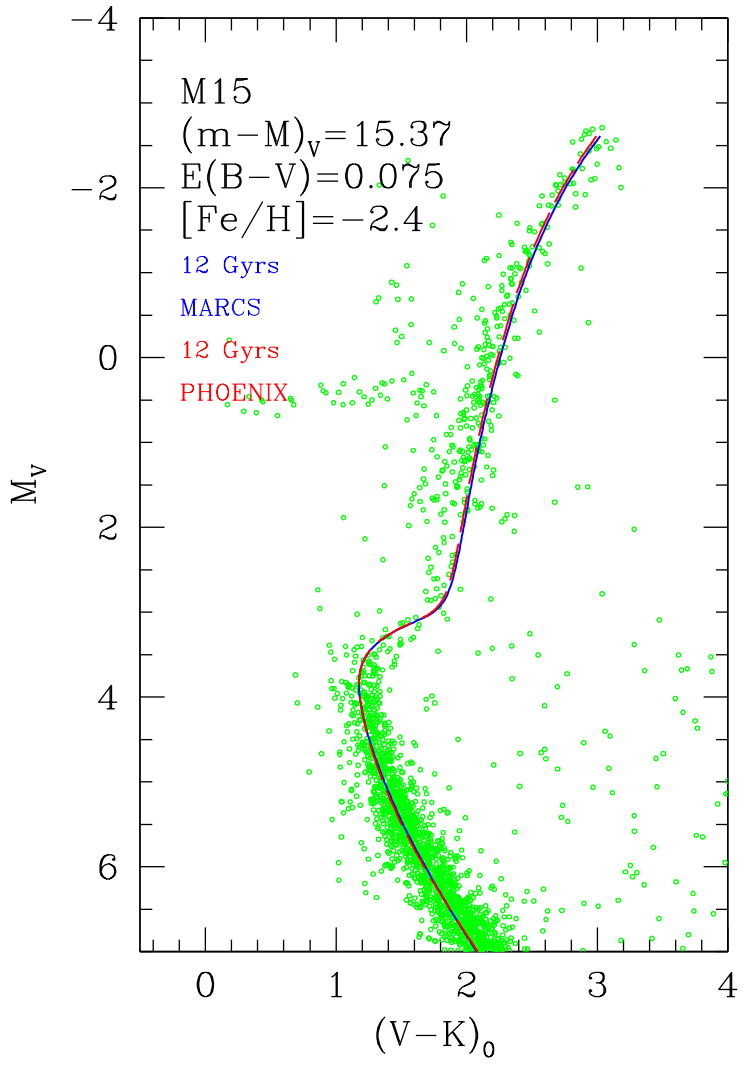

Figure 3.7 Comparison of our M15 $(V-K)_0 - M_V$ CMD with 12 Gyr Victoria isochrones transformed to the observational plane using two different colour-temperature relations: MARCS colour transformations (solid blue line) and PHOENIX models (red dashed line). Fits to the main sequence stars in both cases are consistent with a reddening of E$(B-V)$= 0.075.

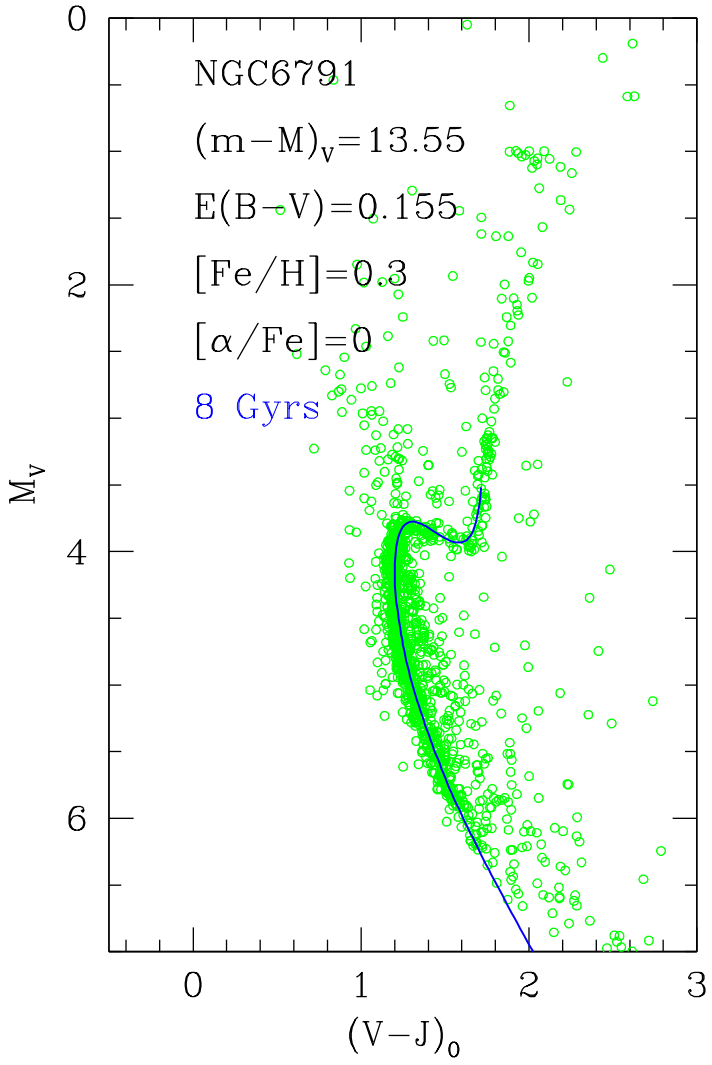

Figure 3.8 Comparison of our NGC6791 $(V-J)_0 - M_V$ CMD and an 8 Gyr Victoria isochrone segment transposed to the observational plane using MARCS colour transformations. A reddening of E$(B-V)$= 0.155 derived by Sandage, Lubin, and VandenBerg (2003) as well as Schlegel et al. (1998), results in excellent agreement between the theoretical and observed main sequence.

3.2.3 M71

Situated in the disc of our galaxy, M71 has a considerable, though poorly known, interstellar reddening: estimates in the literature range from E($B-V$)= 0.21 to 0.32. Kron and Guetter (1976) have quoted the lower value based on six colour photometry of the cluster, in good agreement with Harris (1996) who obtained E($B-V$)= 0.25. Near the upper extreme of reddening estimates for M71, the Schlegel et al. (1998) dust maps indicate a mean line-of-sight reddening of E($B-V$)= 0.305, but as mentioned above, this estimate may not be entirely due to foreground material. Thus, because of its low Galactic latitude ($b = -4.6°$), M71 poses a challenge for reddening determinations.

Through comparison of our $(V-K)_0 - M_V$ CMD with isochrones, we find that adopting E($B-V$) = 0.22 provides the best match of theoretical predictions to M71. Figure 3.9 shows excellent agreement between the main sequence of M71 and a 10 Gyr Victoria isochrone transposed to the observational plane using MARCS colour transformations.

3.3 Defining the Fiducials

Fiducial sequences are ridge lines of the stellar loci in colour-magnitude space. The definition of these fiducials from cluster photometry is often through visual inspection on the CMD, since automated scripts typically give poor results in regions of low star counts and where the magnitude depends weakly on colour (e.g., the subgiant branch). Moreover, contamination from field, AGB, and binary stars as well as horizontal branch stars can significantly skew the computed line. For these reasons we have derived all fiducials by dividing the magnitude axis into small (typically ~ 0.15 but smaller in regions of nearly constant magnitude) bins and then estimating the median colour of those stars which we judge to belong to the loci.

Figures 3.7 through 3.12 present the CMDs of each cluster in our sample along with their derived fiducial sequences spanning the main sequence, subgiant branch and red giant branch (tabulated in Tables 3.2-3.7). In the case of M13, M92 and M15 there were insufficient points to define the fiducial for the subgiant branch and isochrones were used in these areas (such points are marked with an asterisk in the tables).

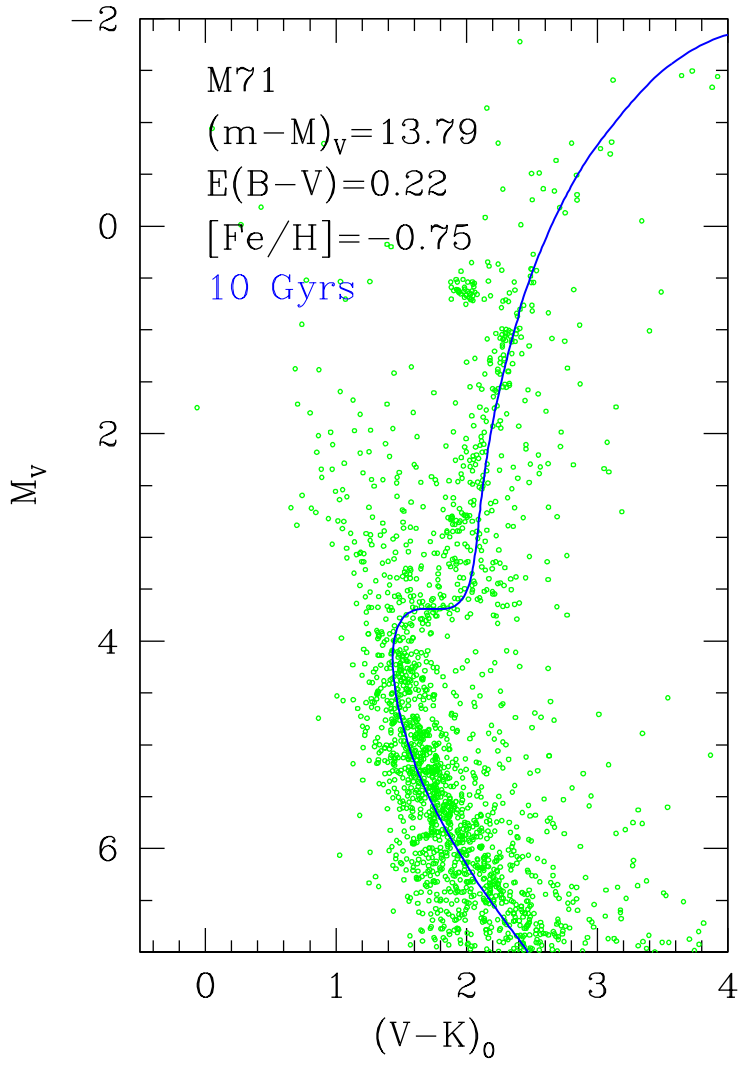

Figure 3.9 Comparison of our M71 $(V-K)_0 - M_V$ CMD and a 8 Gyr VandenBerg main sequence isochrone segment transposed to the observational plane using MARCS colour transformations. With our adopted reddening of E$(B-V)$= 0.22, excellent agreement is found between the theoretical and observed main sequence.

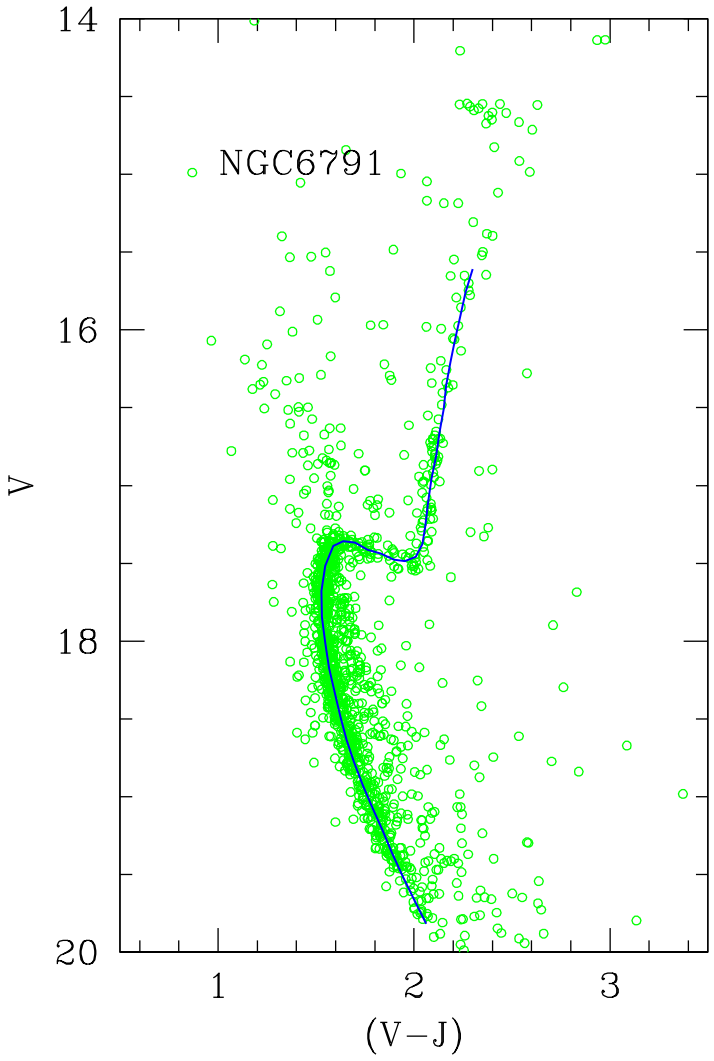

Figure 3.10 NGC6791 M_V-$(V-J)$ fiducial overlying the CMD from Figure 3.2.

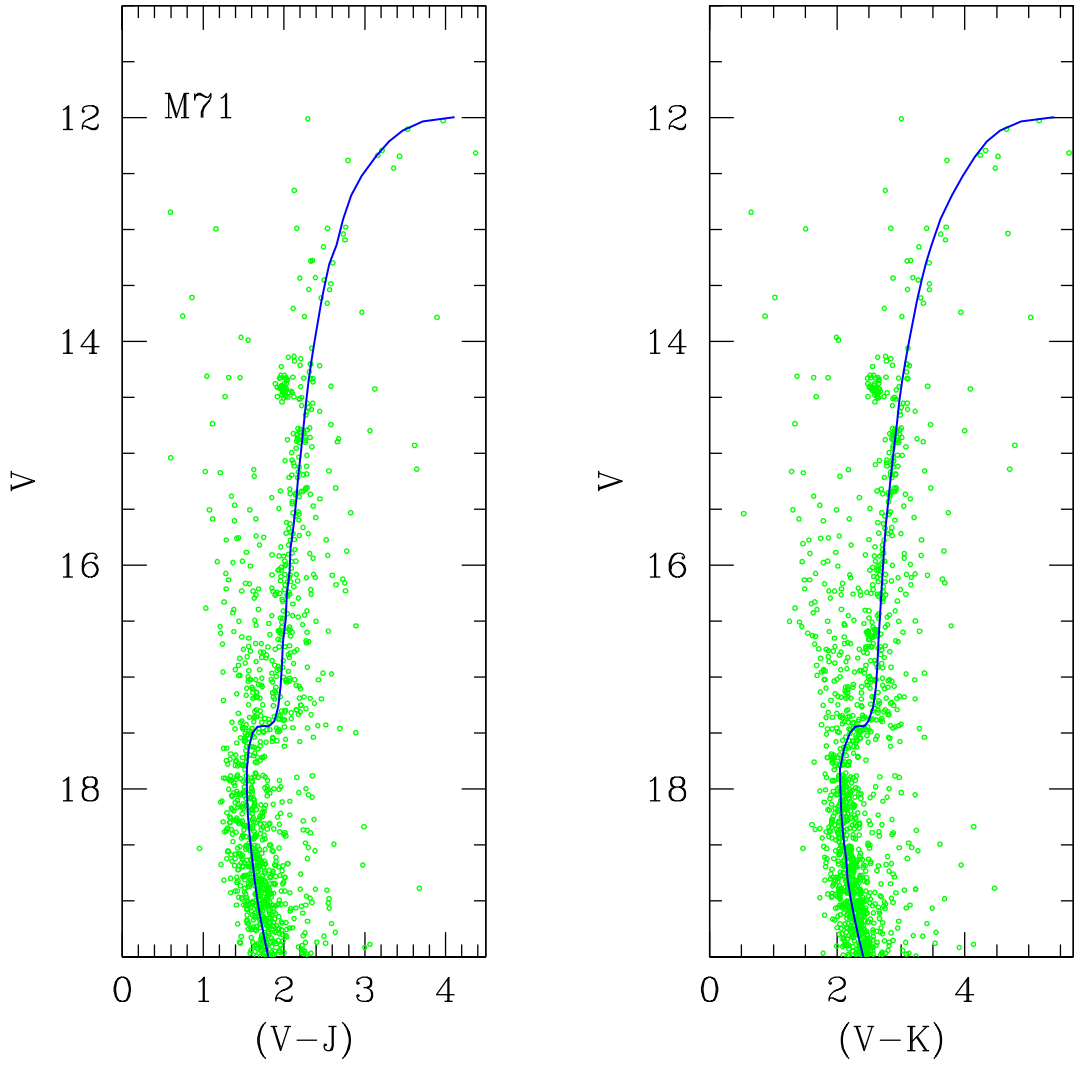

Figure 3.11 M71 M_V-$(V-K)$ and M_V-$(V-J)$ fiducials overlying the CMDs from Figure 3.3.

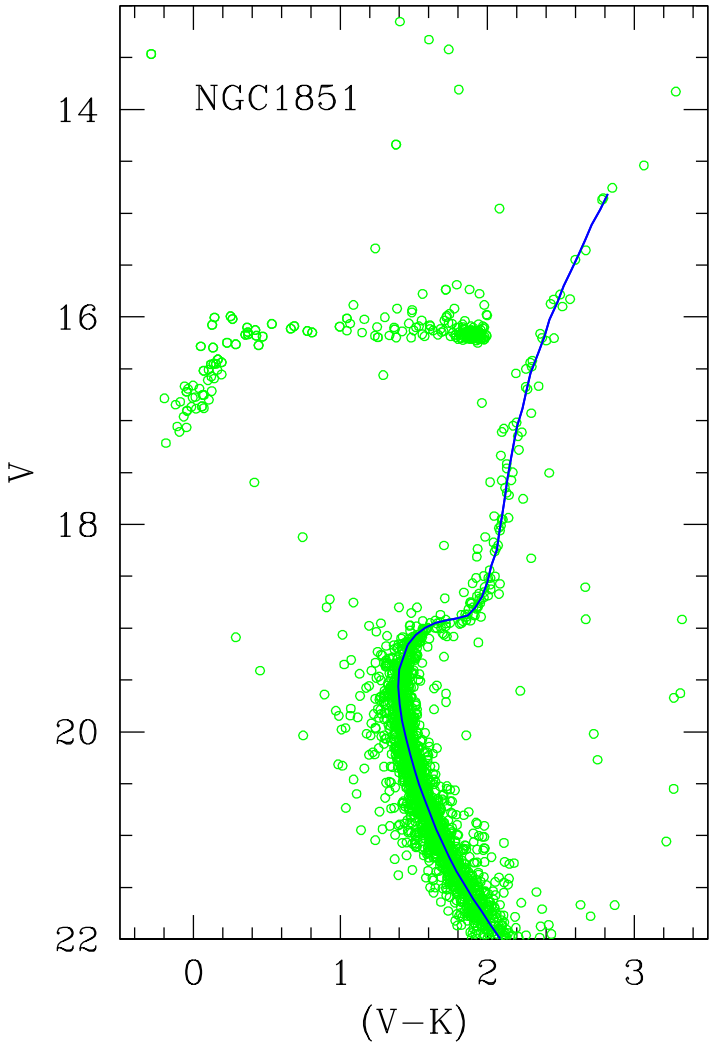

Figure 3.12 NGC1851 M_V-$(V-K)$ fiducial overlying the CMD from Figure 3.1.

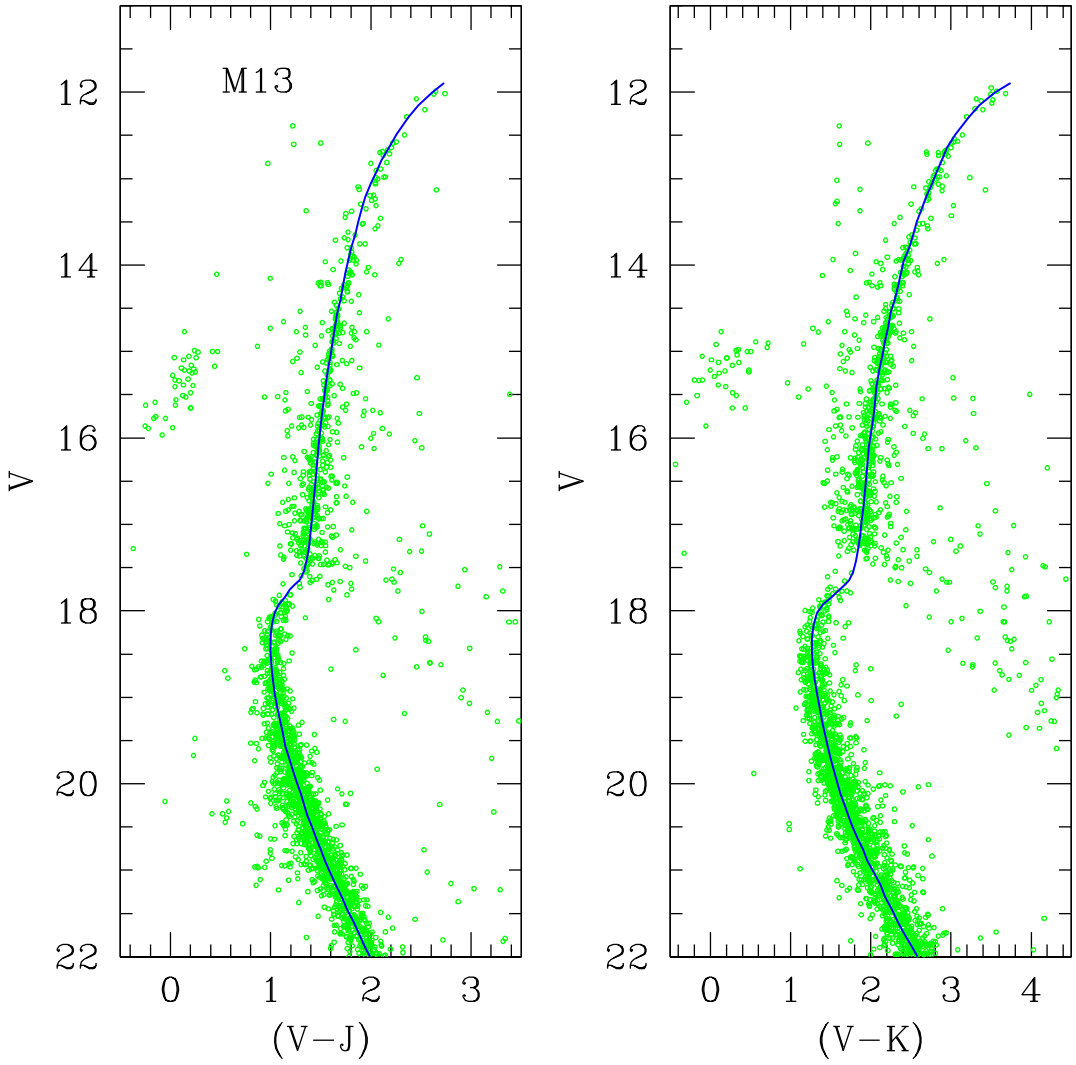

Figure 3.13 M13 M_V-$(V-K)$ and M_V-$(V-J)$ fiducials overlying the CMDs from Figure 3.4.

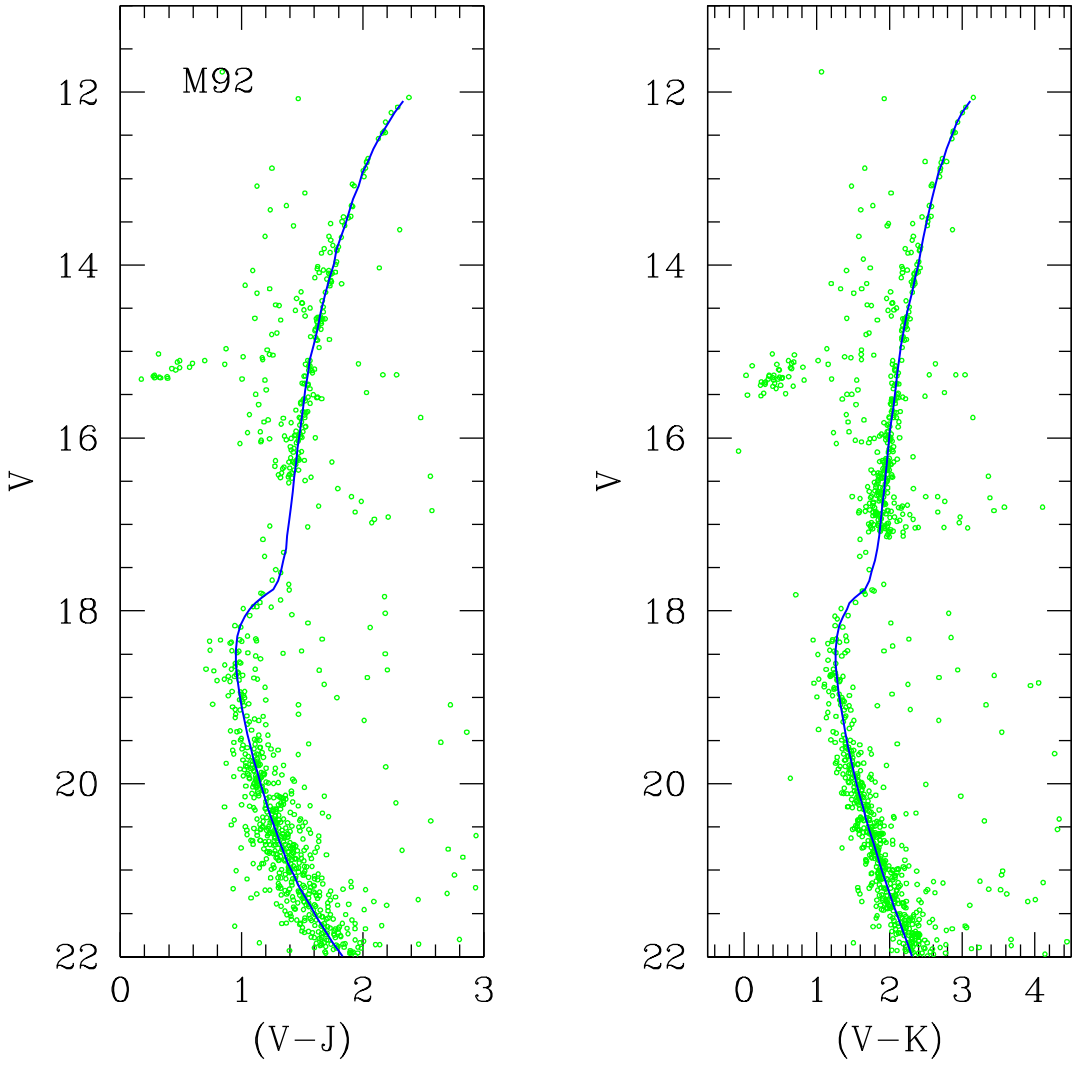

Figure 3.14 M92 M_V-$(V-K)$ and M_V-$(V-J)$ fiducials overlying the CMDs from Figure 3.5.

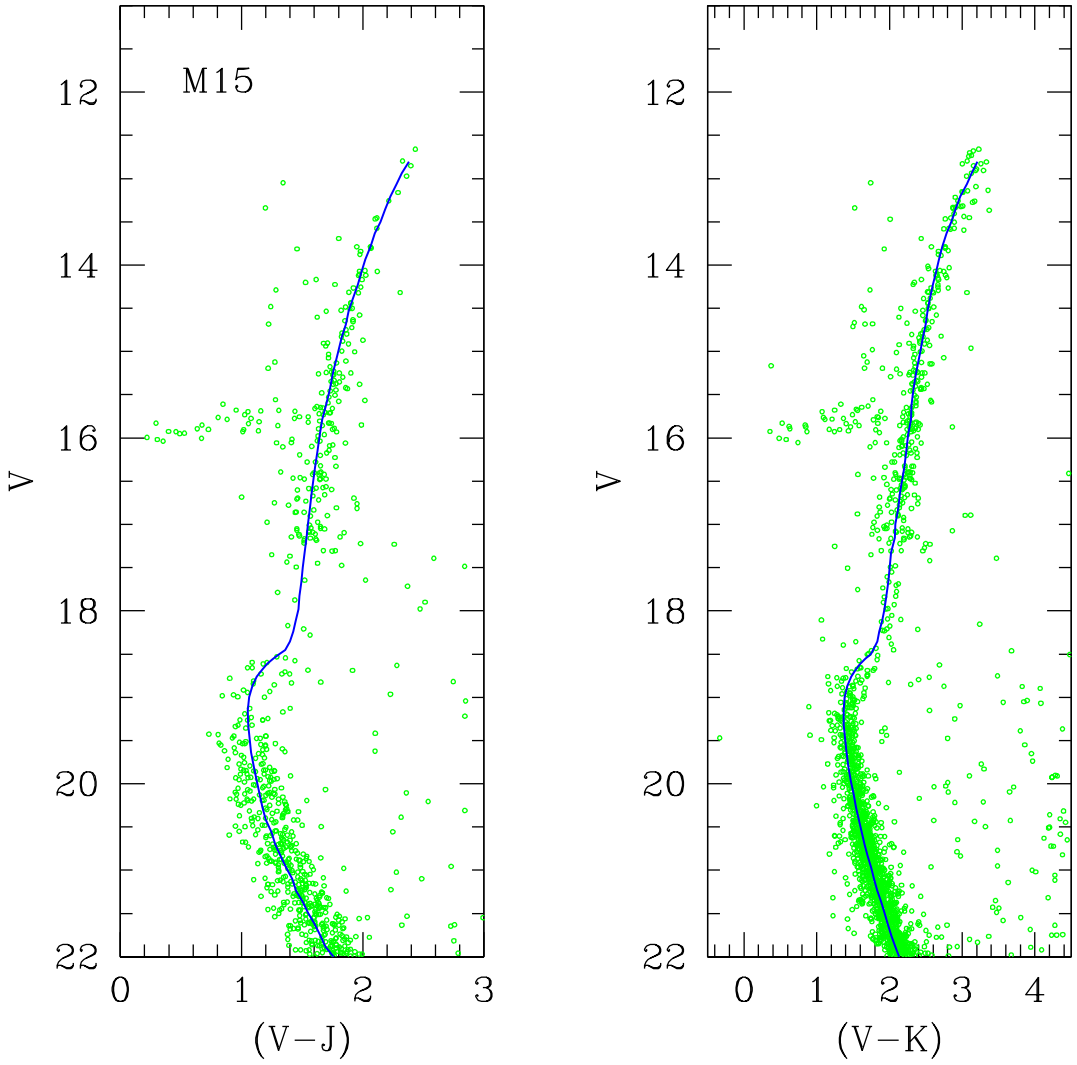

Figure 3.15 M15 M_V-$(V-K)$ and M_V-$(V-J)$ fiducials overlying the CMDs from Figure 3.6.

V	$(V-J)$
19.817	2.062
19.659	2.001
19.515	1.944
19.363	1.889
19.215	1.840
19.067	1.787
18.924	1.738
18.771	1.692
18.633	1.656
18.486	1.625
18.331	1.595
18.172	1.567
18.011	1.548
17.845	1.529
17.676	1.528
17.516	1.548
17.388	1.588
17.357	1.639
17.367	1.699

V	$(V-J)$
17.411	1.762
17.437	1.831
17.476	1.897
17.485	1.953
17.459	2.011
17.376	2.043
17.263	2.058
17.109	2.071
16.959	2.091
16.809	2.114
16.659	2.130
16.509	2.152
16.359	2.164
16.209	2.186
16.059	2.211
15.909	2.236
15.759	2.264
15.609	2.299

Table 3.2 Fiducial sequence for the open cluster NGC6791 as shown in Figure 3.10.

V	$(V-J)$	$(V-K)$	V	$(V-J)$	$(V-K)$
19.505	1.805	2.408	15.854	2.080	2.734
19.338	1.757	2.338	15.627	2.120	2.766
19.168	1.712	2.273	15.426	2.152	2.798
18.991	1.670	2.214	15.217	2.177	2.835
18.807	1.635	2.163	14.986	2.209	2.880
18.622	1.604	2.138	14.736	2.247	2.935
18.429	1.576	2.099	14.538	2.274	2.974
18.232	1.555	2.068	14.356	2.306	3.020
18.029	1.542	2.051	14.177	2.342	3.071
17.824	1.542	2.040	13.993	2.381	3.129
17.634	1.563	2.110	13.818	2.422	3.187
17.500	1.611	2.199	13.646	2.465	3.250
17.445	1.673	2.278	13.459	2.516	3.324
17.439	1.745	2.353	13.305	2.562	3.390
17.441	1.814	2.424	13.139	2.648	3.481
17.396	1.882	2.492	12.906	2.733	3.619
17.267	1.931	2.564	12.693	2.833	3.800
17.084	1.959	2.606	12.523	2.962	3.970
16.885	1.977	2.631	12.347	3.137	4.164
16.688	1.989	2.649	12.212	3.300	4.350
16.485	2.021	2.667	12.116	3.469	4.552
16.268	2.035	2.687	12.035	3.717	4.883
16.060	2.070	2.709	11.997	4.109	5.401

Table 3.3 Fiducial sequences for the globular cluster M71 as shown in Figure 3.11.

V	$(V-K)$	V	$(V-K)$
21.993	2.087	18.806	1.914
21.856	2.020	18.695	1.963
21.729	1.959	18.557	1.998
21.609	1.904	18.401	2.024
21.473	1.844	18.245	2.064
21.344	1.789	18.083	2.081
21.212	1.741	17.917	2.099
21.077	1.696	17.740	2.117
20.938	1.652	17.570	2.136
20.797	1.611	17.410	2.155
20.655	1.573	17.237	2.177
20.510	1.536	17.050	2.202
20.360	1.502	16.885	2.237
20.212	1.472	16.720	2.262
20.052	1.444	16.540	2.292
19.893	1.419	16.342	2.348
19.731	1.402	16.180	2.389
19.564	1.393	16.027	2.420
19.399	1.400	15.857	2.475
19.159	1.457	15.702	2.519
19.063	1.511	15.558	2.568
18.996	1.575	15.403	2.617
18.952	1.644	15.262	2.665
18.923	1.725	15.113	2.708
18.906	1.797	14.964	2.768
18.876	1.868	14.815	2.818

Table 3.4 Fiducial sequence for the globular cluster NGC1851 as shown in Figure 3.12.

V	$(V-J)$	$(V-K)$	V	$(V-J)$	$(V-K)$
22.039	2.011	2.606	17.548	1.331*	1.782*
21.884	1.939	2.513	17.420	1.360*	1.814*
21.740	1.883	2.416	17.271	1.381*	1.844*
21.606	1.832	2.344	17.112	1.397	1.868
21.460	1.766	2.267	16.952	1.411	1.888
21.306	1.709	2.176	16.786	1.424	1.907
21.173	1.653	2.120	16.433	1.451	1.945
21.030	1.596	2.042	16.104	1.478	1.974
20.891	1.541	1.958	15.747	1.511	2.031
20.761	1.501	1.901	15.585	1.527	2.055
20.640	1.455	1.838	15.408	1.546	2.072
20.502	1.414	1.771	15.214	1.569	2.104
20.372	1.368	1.720	15.036	1.601	2.145
20.249	1.334	1.672	14.880	1.620	2.173
20.112	1.299	1.622	14.715	1.643	2.215
19.979	1.260	1.580	14.546	1.667	2.249
19.839	1.220	1.538	14.393	1.697	2.298
19.700	1.182	1.498	14.238	1.722	2.342
19.560	1.146	1.461	14.088	1.748	2.379
19.411	1.119	1.424	13.945	1.774	2.415
19.263	1.095	1.389	13.800	1.802	2.475
19.113	1.063	1.357	13.646	1.843	2.529
18.962	1.042	1.329	13.499	1.875	2.573
18.800	1.024	1.302	13.360	1.907	2.628
18.637	1.008	1.280	13.211	1.944	2.689
18.472	0.999	1.267	13.051	1.999	2.768
18.306	0.999	1.268	12.923	2.053	2.818
18.152	1.014	1.288	12.787	2.104	2.885
18.022	1.043	1.330	12.642	2.182	2.952
17.923	1.083*	1.406*	12.487	2.258	3.058
17.842	1.139*	1.506*	12.289	2.373	3.223
17.751	1.192*	1.612*	12.152	2.474	3.352
17.692	1.242*	1.684*	12.005	2.612	3.547
17.642	1.290*	1.734*	11.895	2.729	3.741

Table 3.5 Fiducial sequences for the globular cluster M13 as shown in Figure 3.13. Due to the lack of sufficient data at some magnitudes, isochrones were used to determine the fiducial points indicated by asterisks. Therefore these points have large uncertainties associated with them.

V	$(V-J)$	$(V-K)$	V	$(V-J)$	$(V-K)$
21.994	1.833	2.309	17.541	1.326*	1.758*
21.836	1.752	2.241	17.418	1.346*	1.800*
21.688	1.684	2.177	17.279	1.368*	1.832*
21.550	1.621	2.119	17.130	1.376*	1.857*
21.420	1.570	2.064	16.970	1.391*	1.880*
21.187	1.474	1.969	16.801	1.406*	1.901*
21.064	1.433	1.920	16.623	1.421*	1.922*
20.924	1.384	1.867	16.453	1.435*	1.942*
20.792	1.347	1.818	16.292	1.448	1.961
20.667	1.314	1.772	16.118	1.463	1.982
20.537	1.280	1.725	15.929	1.479	2.005
20.403	1.247	1.678	15.637	1.507	2.054
20.273	1.216	1.635	15.456	1.525	2.080
20.142	1.186	1.593	15.256	1.547	2.109
20.000	1.155	1.549	15.089	1.565	2.136
19.859	1.127	1.509	14.925	1.595	2.162
19.716	1.099	1.470	14.744	1.627	2.201
19.572	1.073	1.432	14.541	1.653	2.247
19.422	1.047	1.396	14.321	1.692	2.308
19.267	1.023	1.361	14.140	1.727	2.357
19.105	1.000	1.328	13.984	1.761	2.399
18.938	0.980	1.300	13.827	1.783	2.433
18.780	0.965	1.278	13.682	1.818	2.467
18.617	0.953	1.261	13.528	1.857	2.505
18.451	0.951	1.259	13.379	1.889	2.544
18.294	0.963	1.276	13.236	1.920	2.583
18.164	0.990*	1.314*	13.085	1.964	2.626
18.062	1.026*	1.365*	12.933	1.999	2.675
17.981	1.068*	1.415*	12.798	2.046	2.730
17.912	1.113*	1.450*	12.655	2.086	2.787
17.852	1.163*	1.521*	12.503	2.147	2.854
17.803	1.210*	1.589*	12.362	2.208	2.922
17.751	1.261*	1.662*	12.235	2.262	2.998
17.652	1.300*	1.723*	12.103	2.332	3.108

Table 3.6 Fiducial sequences for the globular cluster M92 as shown in Figure 3.14. Due to the lack of sufficient data at some magnitudes, isochrones were used to determine the fiducial points indicated by asterisks. Therefore these points have large uncertainties associated with them.

V	$(V-J)$	$(V-K)$	V	$(V-J)$	$(V-K)$
22.010	1.764	2.140	17.979	1.468*	1.932*
21.887	1.694	2.079	17.830	1.476*	1.957*
21.764	1.653	2.030	17.670	1.491*	1.980*
21.624	1.604	1.977	17.501	1.506*	2.001*
21.492	1.547	1.928	17.323	1.521	2.022
21.367	1.504	1.882	17.153	1.535	2.072
21.237	1.450	1.835	16.992	1.548	2.081
21.103	1.417	1.788	16.818	1.563	2.122
20.973	1.366	1.745	16.629	1.579	2.145
20.842	1.326	1.703	16.337	1.607	2.204
20.700	1.277	1.659	16.156	1.625	2.230
20.559	1.247	1.619	15.956	1.647	2.259
20.416	1.199	1.580	15.789	1.665	2.296
20.272	1.173	1.542	15.625	1.695	2.302
20.122	1.147	1.506	15.444	1.727	2.331
19.967	1.123	1.471	15.241	1.753	2.367
19.805	1.100	1.438	15.021	1.792	2.418
19.638	1.080	1.410	14.840	1.827	2.457
19.480	1.065	1.388	14.684	1.861	2.499
19.317	1.053	1.371	14.527	1.883	2.523
19.151	1.051	1.369	14.382	1.918	2.557
18.994	1.063	1.386	14.228	1.957	2.595
18.864	1.090	1.424	14.079	1.989	2.644
18.762	1.126	1.475	13.936	2.020	2.683
18.681	1.168*	1.535	13.785	2.064	2.726
18.612	1.213*	1.600	13.633	2.099	2.785
18.552	1.263*	1.671	13.498	2.146	2.850
18.503	1.310*	1.739	13.355	2.186	2.907
18.451	1.361*	1.772	13.203	2.227	2.976
18.352	1.400*	1.833	13.062	2.278	3.062
18.241	1.426*	1.858*	12.935	2.322	3.128
18.118	1.446*	1.900*	12.803	2.382	3.208

Table 3.7 Fiducial sequences for the globular cluster M15 as shown in Figure 3.15. Due to the lack of sufficient data at some magnitudes, isochrones were used to determine the fiducial points indicated by asterisks. Therefore these points have large uncertainties associated with them.

Chapter 4

Implications of Near-IR Photometry for Colour-$T_{\rm eff}$ Relations and Stellar Models

4.1 Introduction

In this age of precise stellar photometry, colour-$T_{\rm eff}$ relations play an essential and critical role in bridging the gap between theory and observation. Stellar population studies rely on the accuracy of these relations (and of theoretical stellar models) in order to derive star formation histories, metallicities and ages of systems based on isochrone fits to the observed CMDs. While considerable work has been carried out to test and refine the colour transformations for the $UBVRI$ and Strömgren filter systems (e.g., VandenBerg & Clem 2003; Clem et al. 2004), very little has been done to date on the colour-$T_{\rm eff}$ relations for the near-infrared.

In this chapter, local Population II subdwarf standards are used to test the reliability of the VJK_s transformations based on the latest MARCS model atmospheres (Gustaffson et al. 2008). Using the same transformations, the latest Victoria isochrones are then transposed to the $(V-J)-M_V$ and $(V-K)-M_V$ planes and compared with our CMDs in order to assess how well the former reproduce the latter.

Transforming isochrones from the theoretical $T_{\rm eff}$-M$_{bol}$ plane to an observed colour-magnitude plane requires a set of bolometric corrections and a colour-$T_{\rm eff}$ relation to link the fundamental stellar parameters to photometric indices. In this chapter we investigate the colour-$T_{\rm eff}$ relations derived by Luca Casagrande (in preparation) from

synthetic spectra based on MARCS model atmospheres (Gustafsson et al. 2008). $T_{\rm eff}$, $\log g$, and chemical composition are the main parameters governing the atmospheric models and non-linear combinations of them characterize the features of a stellar spectrum. MARCS models consist of plane-parallel (for dwarf stars) and spherical (for giant stars), line-blanketed, flux-constant stellar atmospheres for a large range in $T_{\rm eff}$, $\log g$ and [Fe/H]. The resulting spectra are then convolved with the appropriate photometric filter transmission profiles. Thus the accuracy of theoretical colour-$T_{\rm eff}$ relations relies heavily on whether or not the synthetic spectra are able to reproduce the observed spectra of stars, and how well the filter transmission functions are defined. Empirical colour-$T_{\rm eff}$ relations (for a brief description, see Chapter 1) have the advantage of being largely model independent, but they are based on a very limited sample of stars for which reasonably well determined values of surface gravity and metallicity exist. Large grids of theoretical colours have an advantage over empirical colour-$T_{\rm eff}$ relations, as the desired photometric indices of any given star or isochrone can be obtained simply by interpolating in a grid of synthetic colours that has been calculated for wide-ranging values of [Fe/H], $\log g$, and $T_{\rm eff}$.

4.2 Testing the Colour-$T_{\rm eff}$ Relations using Subdwarfs

The goal of this section is to investigate whether the predicted MARCS indices can reproduce the observed colours of a well-studied sample of metal-poor halo stars (called subdwarfs) having accurate estimates of $T_{\rm eff}$, $\log g$, and [Fe/H]. Our subdwarf sample consists of those stars whose orbits have brought them near enough to the Sun to have precise trigonometric parallaxes $\sigma_\pi/\pi \lesssim 0.2$. These nearby stars are exceedingly useful as their M_V values can be readily calculated from their apparent magnitude, V, and Hipparcos parallax, π in arc-seconds, using the following equation:

$$M_V = V - 5 + 5\log(\pi). \tag{4.1}$$

Subdwarfs with absolute magnitudes fainter than $M_V \gtrsim 4.6$ are of special importance because their locations on the CMD are insensitive to age. This means that any colour difference seen between two stars of the same magnitude can be attributed primarily to a difference in chemical composition. Tables 4.1 and 4.2 show the Hipparcos subdwarfs used for analysis in this chapter. The former contains all subdwarfs

Star	$(V-J)_{2MASS}$	$(V-K)_{2MASS}$	[Fe/H]	$\log g$	$T_{\rm eff}$	$(V-J)_{MARCS}$	$(V-K)_{MARCS}$
BD+174708	1.03	1.39	-1.65	4.09	6050	1.07	1.44
BD+023375	1.15	1.45	-2.17	4.2	6018	1.09	1.48
BD+262606	1.06	1.38	-2.29	4.23	6146	1.04	1.40
BD+511696	1.24	1.61	-1.26	4.87	5708	1.21	1.64
BD+660268	1.38	1.85	-1.92	5.0	5362	1.38	1.87
BD+720094	0.98	1.32	-1.62	4.48	6346	0.96	1.28
HD 3567	1.04	1.37	-1.17	4.22	6100	1.04	1.39
HD 16031	0.98	1.32	-1.66	4.33	6194	1.02	1.36
HD 74000	0.96	1.28	-1.92	4.55	6275	0.99	1.33
HD 84937	0.98	1.27	-2.04	4.06	6344	0.96	1.28
HD 94028	1.08	1.38	-1.38	4.54	6060	1.07	1.43
HD 122196	1.11	1.46	-1.75	4.12	5976	1.10	1.49
HD 188510	1.26	1.71	-1.37	5.0	5628	1.25	1.69
HD 194598	1.01	1.35	-1.01	4.65	6047	1.06	1.42
HD 201891	1.12	1.44	-0.94	4.97	5974	1.09	1.46
HD 64090	1.32	1.74	-1.6	4.99	5515	1.30	1.77
HD 103095	1.49	2.05	-1.22	4.92	5124	1.52	2.07
HD 108177	0.99	1.31	-1.55	4.5	6178	1.02	1.37
HD 019445	1.09	1.39	-1.91	4.78	6080	1.07	1.44
HD 25329	1.75	2.32	-1.69	4.65	4849	1.69	2.31
HD 034328	1.1	1.42	-1.44	4.89	5986	1.10	1.47
HD 094028	1.07	1.37	-1.32	4.54	6060	1.06	1.43
HD 103095	1.48	2.05	-1.24	4.92	5124	1.52	2.07
HD 126681	1.24	1.65	-1.09	4.95	5625	1.25	1.69
HD 134439	1.61	2.14	-1.30	4.74	5106	1.52	2.09
HD 134440	1.71	2.32	-1.28	4.74	4879	1.68	2.31
HD 145417	1.66	2.26	-1.64	4.50	4953	1.62	2.22
HD 188510	1.28	1.72	-1.37	4.99	5628	1.25	1.69
HD 193901	1.14	1.5	-1.00	4.79	5796	1.17	1.57
HD 194598	1.02	1.37	-1.02	4.65	6047	1.06	1.42
HD 201891	1.14	1.45	-0.97	4.97	5974	1.09	1.46

Table 4.1 Photometric and spectroscopic properties of our adopted subdwarf sample. $(V-J)_{2MASS}$ and $(V-K)_{2MASS}$ are from the 2MASS (J and K) and Hipparcos (V) catalogs. [Fe/H] , $T_{\rm eff}$ and $\log g$ values are taken from Gratton et al. (1996) and Carretta et al. (2000). $(V-J)_{MARCS}$ and $(V-K)_{MARCS}$ are generated by interpolating the given values of [Fe/H] , $T_{\rm eff}$ and $\log g$ through the MARCS grids.

Star	M_V	σ_{Mv}	$T_{\rm eff}$	$\log g$	[Fe/H]	V	V-J	V-K_S	J-K_S
HD 019445	5.088	0.096	6080	4.78	-1.91	8.026	1.076	1.386	0.310
HD 025329	7.187	0.043	4849	4.65	-1.69	8.519	1.749	2.319	0.570
HD 034328	5.230	0.151	5986	4.89	-1.44	9.416	1.096	1.416	0.320
HD 094028	4.622	0.128	6060	4.54	-1.32	8.202	1.072	1.372	0.300
HD 103095	6.610	0.020	5124	4.92	-1.24	6.420	1.480	2.050	0.570
HD 126681	5.713	0.164	5625	4.95	-1.09	9.301	1.261	1.671	0.410
HD 134439	6.784	0.087	5106	4.74	-1.30	9.118	1.608	2.138	0.530
HD 134440	7.111	0.108	4879	4.74	-1.28	9.474	1.714	2.324	0.610
HD 145417	6.858	0.024	4953	0.00	-1.64	7.549	1.659	2.259	0.600
HD 188510	5.868	0.100	5628	4.99	-1.37	8.851	1.281	1.721	0.440
HD 193901	5.441	0.118	5796	4.79	-1.00	8.644	1.144	1.504	0.360
HD 194598	4.625	0.150	6047	4.65	-1.02	8.356	1.026	1.376	0.350
HD 201891	4.646	0.078	5974	4.97	-0.97	7.390	1.140	1.450	0.310

Table 4.2 Properties of selected Hipparcos subdwarfs used in our analysis which had J and K photometry measured with 2MASS, M_V greater than 4.6 and σ_{M_V} less than 0.2. [Fe/H] values are from Carretta et al (2000), whereas fully consistent $T_{\rm eff}$ and $\log g$ values are taken from Gratton et al. (1996).

with measured 2MASS colours and Gratton et al. (1996) physical parameters. The latter table is a subset of these stars which have very low errors in parallax equivalent to $\sigma_{M_V} \lesssim 0.2$.

4.2.1 Effective Temperature Scale of the Subdwarfs

Since $T_{\rm eff}$ is the most critical parameter in determining the colour of a star, the choice in temperature scale will have a large impact on the synthetic colours derived for the subdwarfs. For our analysis we have adopted the spectroscopic $T_{\rm eff}$ measurements of Gratton et al. (1996) calculated using ATLAS9 model atmospheres to fit the flux distributions of observed stellar spectra. This choice was based on investigations into several different $T_{\rm eff}$ scales, with the Gratton et al. (1996) estimates giving the most consistent comparisons with model predictions (e.g., see Bergbusch & VandenBerg 2001). The empirical $T_{\rm eff}$ scales of Cenarro et al. (2007), Alonso et al. (1996) and Melendez et al. (2006) resulted in temperatures which were ≈ 100 K cooler than the models (see VandenBerg 2008 for further discussion).

Granted, a possible interpretation of these results is that the $T_{\rm eff}$ scale of the stellar models is too hot by $\sim$ 100K. However, the latest empirical $(V-K)$ versus $T_{\rm eff}$ relation by Casagrande et al. (in preparation) suggests otherwise. The later have used the infrared flux method to derive:

$$\begin{aligned}\frac{5040}{T_{\rm eff}} = \theta = \; & 0.5058 + 0.2599(V-K_S) - 0.0146(V-K_S)^2 \\ & -0.0132(V-K_S)[Fe/H] \\ & +0.00289[Fe/H] + 0.0016[Fe/H]^2 \; . \end{aligned} \tag{4.2}$$

In Figure 4.1 we plot the spectroscopic $T_{\rm eff}$ value obtained by Gratton et al. (1996) against the photometrically-based $T_{\rm eff}$ value from Casagrande for each subdwarf in Table 4.1. The results are remarkably consistent, lending additional support for our choice of the Gratton (and the model) $T_{\rm eff}$ scale since these two scales are based on completely different methods and yield nearly identical results.

4.2.2 Observed versus Predicted Colours

Comparisons of the observed and predicted colours of subdwarfs allows us to see any inconsistencies in the MARCS transformations. That is, if MARCS colours are

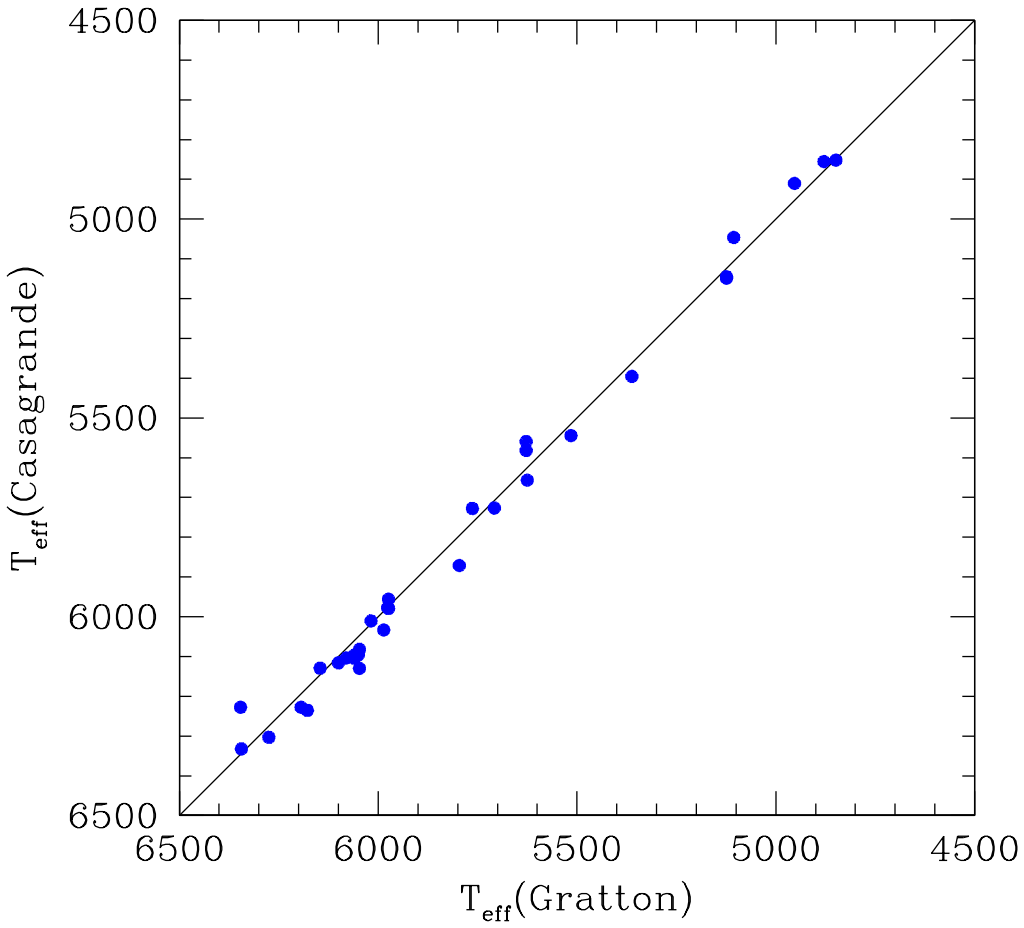

Figure 4.1 Comparison of spectroscopic and photometric $T_{\rm eff}$ estimates of the subdwarfs. The former is taken from Gratton et al. (1996), while the latter comes from the empirical relation developed by Casagrande (in preparation) given in equation 4.2, using inputs of 2MASS K and Hipparcos V photometry, along with Gratton estimates for [Fe/H]. The solid curve indicates the line of equality.

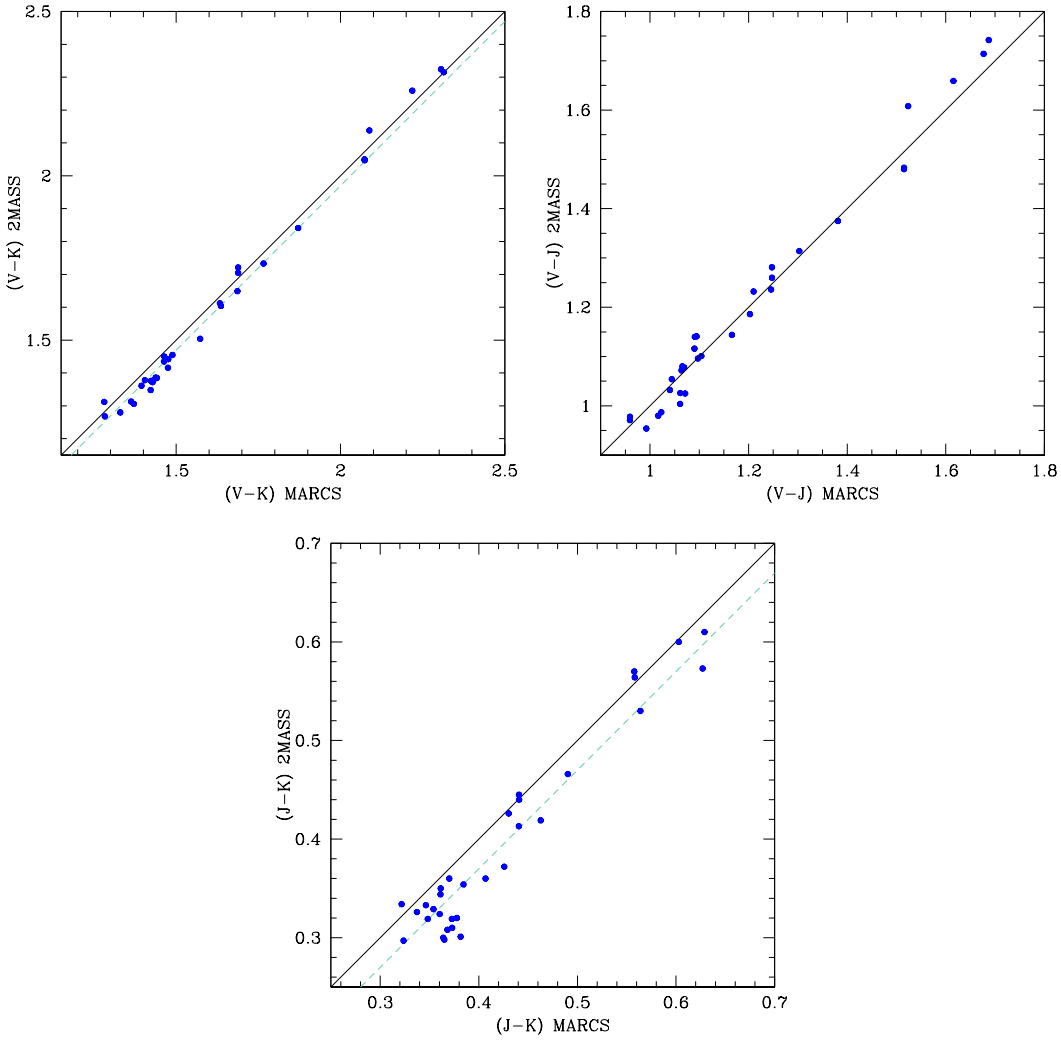

Figure 4.2 Comparisons of the predicted and observed $(V-K)$, $(V-J)$ and $(J-K)$ colours of subdwarfs from Table 4.1. For the theoretical colour, Carretta et al. (2000) estimates for [Fe/H], and the Gratton et al. (1996) estimates of $\log g$, and $T_{\rm eff}$ were used to interpolate in the colour tables of MARCS model atmospheres. The empirical colours are from 2MASS photometry and V magnitudes from the Hipparcos catalog. Solid curves indicate the line of equality, while the dashed curves apply a constant offset of 0.03 mag.

generated for each subdwarfs' best estimate of $T_{\rm eff}$, $\log g$ and [Fe/H], they should reproduce the observed photometry from the 2MASS (J and K) and Hipparcos (V) catalogs. Figure 4.2 shows the level of agreement between the observed and predicted $(V-K)$, $(V-J)$, and $(J-K)$ colours for the subdwarfs in Table 4.1.

An inspection of the upper left panel of Figure 4.2 indicates that a constant offset of ~ 0.03 mag to the blue is needed for the models to match the observations in $(V-K)$. This is similar to what is required to center the $(J-K)$ observations (see the lower plot) on the line of equality. The predicted and observed $(V-J)$ colours match well at bluer colours, but appear to deviate at the red end which suggests that the $(V-J)$ transformations for cooler dwarf stars do not reproduce the observations (also suggested by the cluster photometry). Possible explanations for this are considered in section 4.4.

As $T_{\rm eff}$ is the most sensitive determinant of stellar colour, it is worth discussing the effect of the $T_{\rm eff}$ scale on the colour offsets seen in Figure 4.2. If we were to apply an increase in the temperatures of the subdwarfs, it would cause all the predicted colours to shift to the blue. However, the colours of cool stars are much more sensitive to $T_{\rm eff}$ than those of hot stars, and therefore increasing each subdwarf's temperature by a constant amount results in a much larger colour correction for those stars with redder intrinsic colours. Thus when we apply a 75 K increase in $T_{\rm eff}$ to all subdwarfs and produce the same plots as in Figure 4.2, the results are no longer lines, but curves fitting the hotter stars, while the predicted colours of the cooler stars become too *blue*. Since the Gratton et al. (1996) and Casagrande et al. (in prep.) scales are already among the hottest temperature scales in the literature, it is difficult to justify a further increase of the temperatures in order to match the observed colours. In addition, any increase in a spectroscopic temperature scale must be coupled with an increase in the metallicity scale in order to match the observed spectral line strengths. This would be in conflict with several Population II subdwarf studies where the Gratton [Fe/H] scale has long been favoured (e.g., VandenBerg 2003). Furthermore, the remarkable consistency between the spectroscopic Gratton scale and most up-to-date empirical photometric scale seen in Figure 4.1, provides compelling support for the Gratton temperature scale.

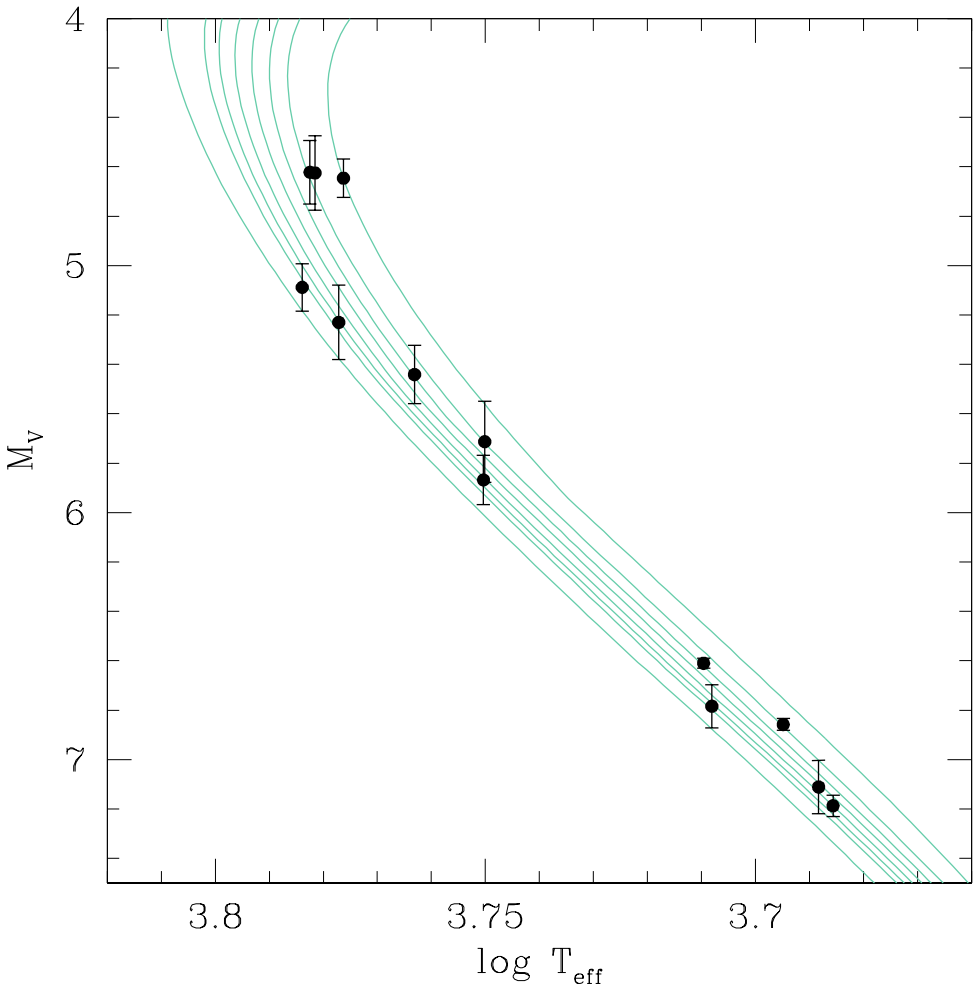

Figure 4.3 Sample of Hipparcos subdwarfs overlying 14 Gyr Victoria isochrones for [Fe/H] values of -2.0, -1.7, -1.6, -1.5, -1.4, -1.3, -1.2, and -1.0, respectively, from left to right. The subdwarfs plotted here are those listed in Table 4.1, with M_V values calculated from Hipparcos parallaxes, and $T_{\rm eff}$ values from Gratton et al. (1996).

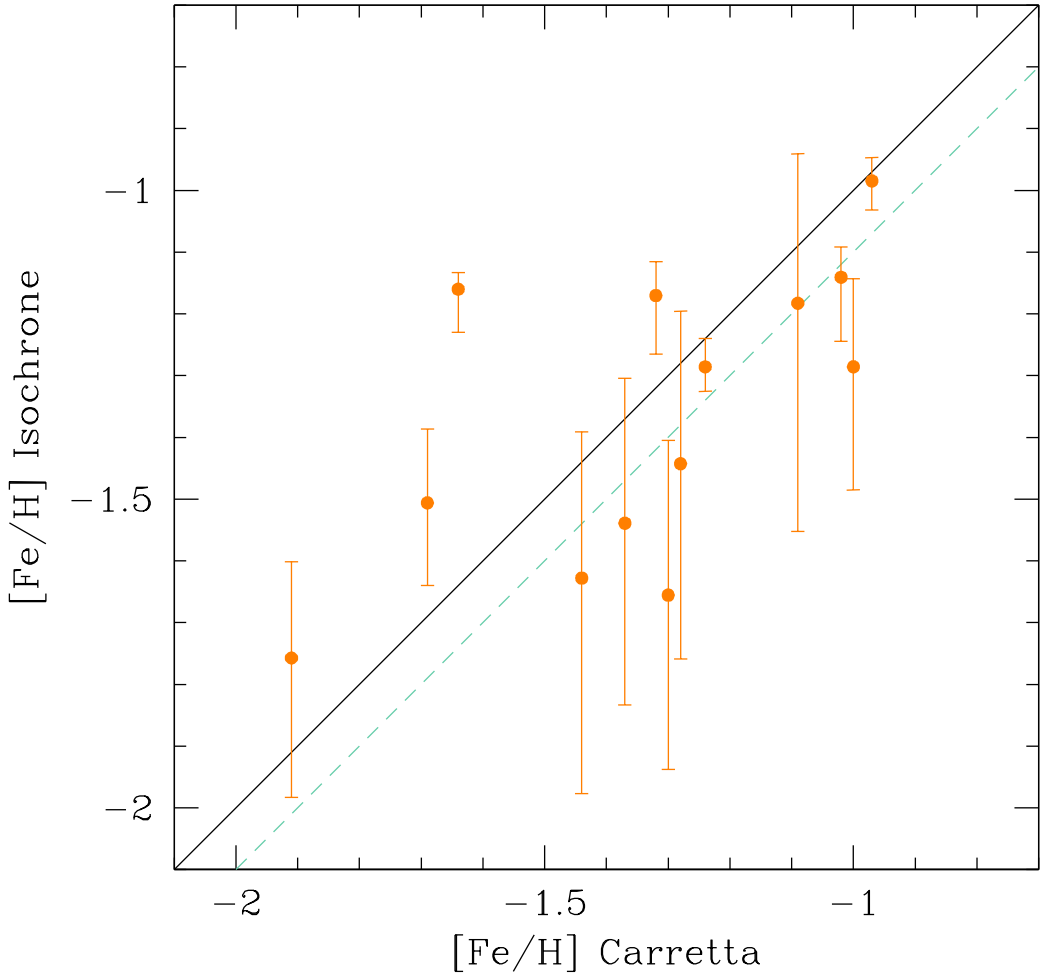

Figure 4.4 Comparison between the spectroscopically obtained [Fe/H] from Carretta et al. (2000), with the [Fe/H] estimate based on Victoria isochrones. The latter was found by using the estimated M_V and $T_{\rm eff}$ values of each subdwarf given in table 4.1, and interpolating these within a grid of main-sequence isochrone segments (those plotted in figure 4.3) to find [Fe/H]. Upper and lower error bars on the $[{\rm Fe/H}]_{isochrone}$ measurements are found by subtracting and adding the σ_{M_V} to the M_V and re-interpolating in the isochrones. The solid curve shows the line of equality, while the dashed curve is a constant offset of 0.1 dex.

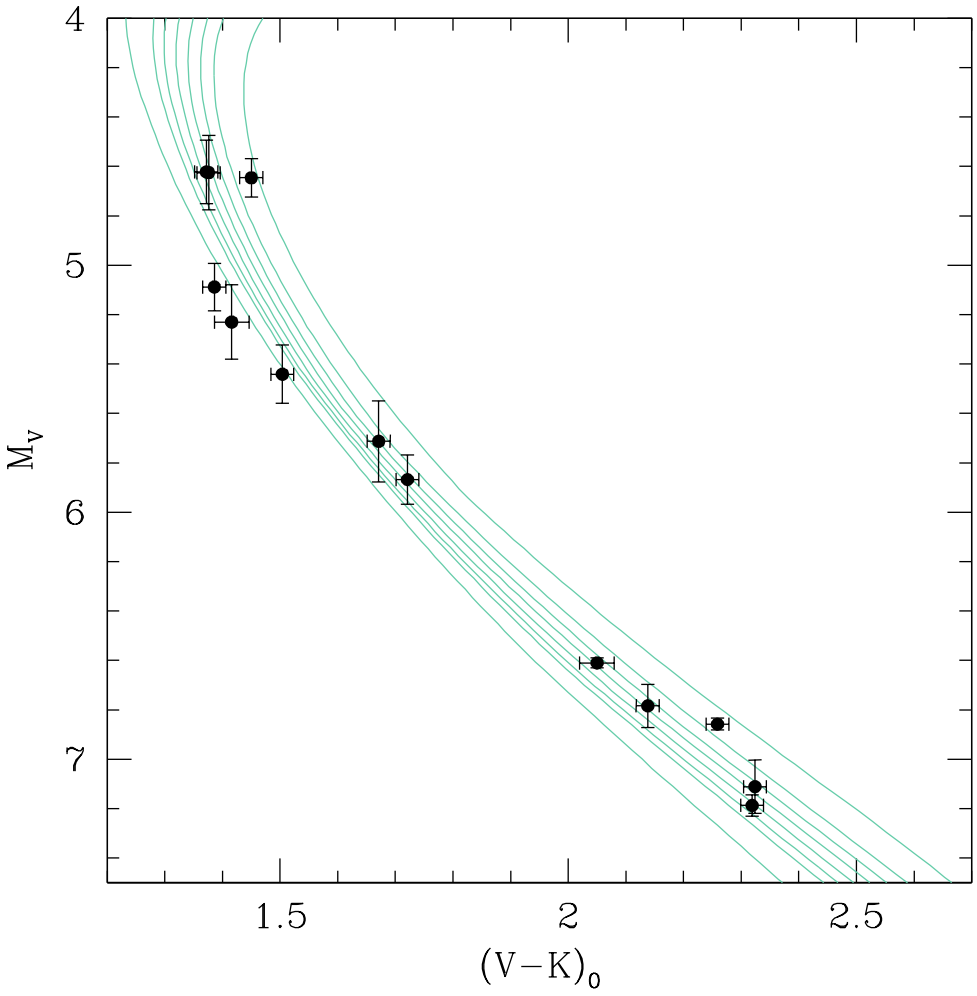

Figure 4.5 Sample of Hipparcos subdwarfs overlying 14 Gyr Victoria isochrones in the M_V-$(V-K)$ plane. The isochrones plotted here have [Fe/H] values of -2.0, -1.7, -1.6, -1.5, -1.4, -1.3, -1.2, and -1.0, respectively, from left to right, and have been transformed to the $(V-K)$ plane using MARCS transformations. The subdwarfs are those listed in Table 4.1, with M_V values calculated from Hipparcos parallaxes, and colours from the 2MASS and Hipparcos catalogs.

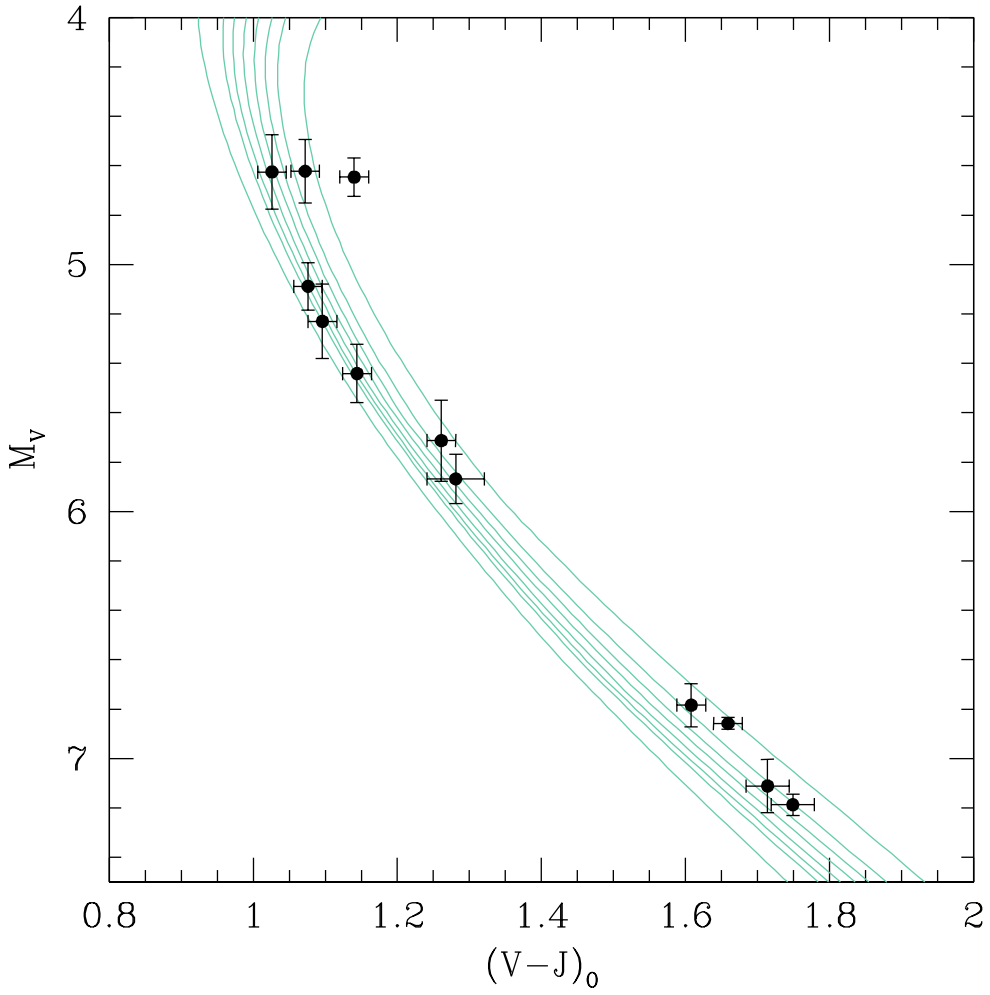

Figure 4.6 Sample of Hipparcos subdwarfs overlying 14 Gyr Victoria isochrones in the M_V-$(V-J)$ plane. The isochrones plotted here have [Fe/H] values of -2.0, -1.7, -1.6, -1.5, -1.4, -1.3, -1.2, and -1.0, respectively, from left to right, and have been transformed to the $(V-J)$ plane using MARCS transformations. The subdwarfs are those listed in Table 4.1, with M_V values calculated from Hipparcos parallaxes, and colours from the 2MASS and Hipparcos catalogs. HD 103095 was not included in this plot due to its large J photometric uncertainty of 0.2, prohibiting any useful conclusions to be drawn from its position.

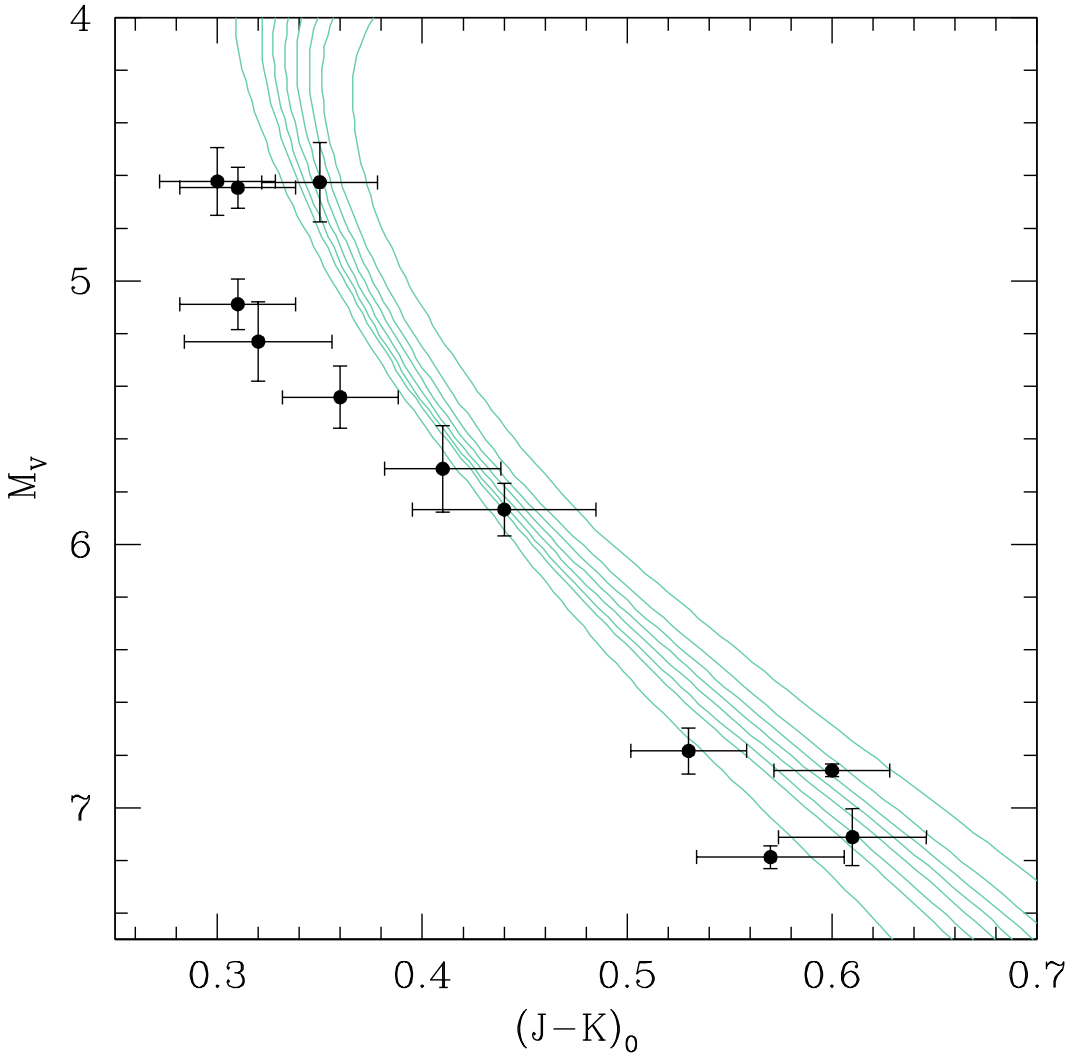

Figure 4.7 Sample of Hipparcos subdwarfs overlying 14 Gyr Victoria isochrones in the M_V-(J-K) plane. The isochrones plotted here have [Fe/H] values of -2.0, -1.7, -1.6, -1.5, -1.4, -1.3, -1.2, and -1.0, respectively, from left to right, and have been transformed to the $(V - J)$ plane using MARCS transformations. The subdwarfs are those listed in Table 4.1, with M_V values calculated from Hipparcos parallaxes, and colours from the 2MASS and Hipparcos catalogs. HD 103095 was not included in this plot due to its large J photometric uncertainty of 0.2, prohibiting any useful conclusions to be drawn from its position.

4.2.3 Consistency Across Colour Planes

The comparisons described in the previous section are completely independent of stellar evolutionary models, however, one can also compare Hipparcos subdwarfs *directly* with isochrones on the theoretical $T_{\rm eff}$-M$_V$ plane. Figure 4.3 shows a sample of Hipparcos subdwarfs overlying 14 Gyr Victoria isochrones for a range in [Fe/H] values from -2.0 to -1.0. The subdwarfs plotted here are those listed in Table 4.1 which span the same range in metallicity as the isochrones. Their M_V values are calculated from Hipparcos parallaxes, and $T_{\rm eff}$ estimates are from Gratton et al. (1996). The isochrones bracket the $T_{\rm eff}$ values of all the subdwarfs. By overlying the subdwarf standards onto a grid of isochrones for a wide range in [Fe/H] (and a fixed age—though there is essentially no age dependence at faint luminosities) it is possible to examine the consistency of the observed [Fe/H] value with that inferred from the isochrones, given the observed $T_{\rm eff}$.

Figure 4.4 shows a comparison between the spectroscopically obtained [Fe/H] from Carretta et al. (2000), with the [Fe/H] estimates based on Victoria isochrones. The latter were derived in the following way: at the M_V of each subdwarf, the isochrones span a range in $T_{\rm eff}$ as a consequence of the assumed metallicity differences (from -2.0 to -1.0). The point representing each subdwarf superimposes an isochrone for a specific [Fe/H] value — which can be readily obtained by linear interpolation at a constant M_V. This is our so-called "[Fe/H]$_{isochrone}$" estimate. If there were perfect consistency with the spectroscopic estimate of [Fe/H] (from Carretta et al. 2000) the two values would be identical. In fact 4.4 indicates that there is good agreement between [Fe/H]$_{isochrone}$ and [Fe/H]$_{Carretta}$ to within $\sim$0.1 dex.

Upper and lower error bars on the [Fe/H]$_{isochrone}$ values are derived from subtracting and adding σ_{M_V} to the M_V and re-running the interpolation. In the mean, we find remarkable agreement between the predicted and observed [Fe/H] scales. With regards to outlaying stars in this plot, it is possible that some may be spectroscopic binaries, as was the case for a star previously included in our sample: HD 116064 (Smith et al. 1998).

Moreover, one wants to ensure that the adopted colour-$T_{\rm eff}$ relations yield consistent interpretations of the observations on the different colour planes. If a star lies on the same isochrone (say, one with [Fe/H]$= -1.5$) in all colour planes, it indicates that the colour-$T_{\rm eff}$ transformations are consistent for those colours. If any obvious discrepancies exist for different filter combinations, then this is an indication that

there may be a problem with the colour-temperature relations for one or more filters (i.e., they do not adequately represent the spectrum of a star in the wavelength range spanned by that filter).

Figures 4.5 - 4.7, plot the same isochrones, but transformed to the $(V-K)$, $(V-J)$ and $(J-K)$ colour planes using the MARCS colour-$T_{\rm eff}$ relations. The $(V-K)$ and $(V-J)$ plots show a significant shift (especially at the lowest [Fe/H] values) of the subdwarfs with respect to the isochrones relative to what is shown in Figure 4.3. The strongest indication of a problem is found in the $(J-K)$ transformations shown in Figure 4.7; the MARCS-transformed isochrones imply implausibly low values of [Fe/H] which are contrary to the implications of the other colour planes, as well as the $T_{\rm eff}$ - M_V plot.

The systematic offsets seen between the different colour planes lead to conflicting interpretations of the observations, depending on what colour is used. This is strong evidence that a problem exists with the MARCS transformations to J, in particular, for dwarf stars. As this is also seen with the cluster photometry that is presented in the following section, we discuss the results together in section 4.4.

4.3 Testing the Isochrones with Cluster Photometry

Because each Galactic star cluster has essentially a single age and metallicity, these nearby, well studied stellar populations provide an ideal testing ground for theoretical isochrones. Comparisons between isochrones and observed fiducial sequences are fundamental tests of stellar evolutionary models as well as the colour-$T_{\rm eff}$ relations employed in transforming them from the theoretical to observational planes.

Because the MARCS grids have not only a $T_{\rm eff}$ dependence, but are also a function of log g and [Fe/H], we separate our analysis of the fiducials into two parts: the giant branch and the main sequence fits. This allows us to test whether the transformed isochrones are able match observations at both high and low surface gravities. Within this separation of log g values, we also want to examine clusters of both high and low metallicity, in order to test whether the relations are able to adequately reproduce cluster fiducials across all metallicities. Galactic clusters are unique testing grounds, as only by comparisons with these fiducial sequences can we ascertain whether or not the transformed isochrones are able to connect dwarfs and giants of the same

metallicity.

For all comparisons with our fiducials we use the latest Victoria isochrones which incorporate He diffusion and have an alpha enhancement of $[\alpha/\mathrm{Fe}] = +0.4$, except in the case of NGC6791 where the solar value of $[\alpha/\mathrm{Fe}] = 0$ was used. The [Fe/H] values of the isochrones were based on spectroscopic estimates of each cluster's [Fe/H] value, given in Table 3.1. We then transformed the isochrones of these same [Fe/H] values to the $(V-J)$ and $(V-K)$ planes using the MARCS colour-T_{eff} relations.

4.3.1 Main Sequence Fits

The MARCS-transformed isochrones are compared with the $(V-K)$ and $(V-J)$ fiducials of our six clusters in Figures 4.8–4.13.

Focusing first on the main sequence, isochrones on both the $(V-J)$-M_V and $(V-K)$-M_V planes fit all six of our clusters in the vicinity of the turnoff quite well. As we look at fainter magnitudes along the main sequence, we find the isochrones match the $(V-K)$ colours of the cluster stars though there are minor deviations between the predicted and observed $(J-K)$ colours at low metallicity. For our metal poor clusters, M15, M13 and M92, we see that the isochrones in $(V-J)$ appear to be slightly too blue relative to the observations at magnitudes fainter than ~ 2 mag below the turn-off. For our most metal rich cluster, NGC6791, which is also our only open cluster, (see Figure 4.13) the isochrones provide an excellent match to the dwarfs at cool temperatures.

Since isochrones transformed to the $(V-J)$ and $(V-K)$ planes are identical in their [Fe/H], log g and T_{eff} values, the fact that the $(V-J)$ colours give different predictions for the lower main sequence than $(V-K)$ for the same metallicities, suggests that there is an inconsistency in the MARCS transformations (assuming that the photometry is accurate).

Although not shown here, the MARCS transformations fit the curvature of the main sequences in $(V-I)$ and $(B-V)$ for metal-poor systems, which adds to our suspicion that the discrepancies in lower main sequence fits seen in $(V-J)$ are caused by inaccuracies in the predicted MARCS J-band for cool main sequence stars. At these cool temperatures, molecules form very complex absorption spectra, and since the J-band samples the range where water absorption occurs, insufficient modeling of this effect could be a possible explanation for the discrepancies seen.

4.3.2 Red Giant Branch Fits

As far as the predicted and observed red giant branches (RGBs) are concerned, we find good agreement for the most metal-rich clusters: M71, NGC1851 and NGC6791. Additionally, we find excellent agreement when overlying isochrones on 2MASS $(V - K)$ data for the solar metallicity open cluster, M67.

A clear discrepancy, however, emerges for our metal-poor clusters, M15, M92 and M13 shown in Figures 4.8, 4.9 and 4.10. In both $(V - J)$ and $(V - K)$, the isochrones consistently lie to the red of the observed giant branch, beginning at the base of the giant branch and only begin to match observations as they approach the RGB tip. For M15 and M92 the giant branches of the models show offsets from the base of the giant branch of ~ 0.12 in $(V - K)$ and ~ 0.09 in $(V - J)$. Since the predicted giant branches for metal deficient clusters exhibit the same behavior in both $(V - J)$ and $(V - K)$, it shows that the MARCS relations provide consistent giant branch interpretations. One can only speculate that, for some still unexplained reason, the predicted giant branches of Victoria isochrones for metal-poor stars are too cool.

4.4 Conclusions

Comparisons of the predicted and observed subdwarf $(V - J)$ colours show that the MARCS transformations predict the colours of the hot stars well, but are too *blue* for cooler stars. We see this effect again when comparing MARCS-transformed isochrones to our cluster photometry: the $(V - J)$ main sequences are too blue at cooler temperatures for our metal-poor clusters. Since the main sequence fits of $(V - K)$ isochrones to our cluster photometry are in excellent agreement, MARCS transformations lead to inconsistent interpretations in the different colours. Analyzing colour-magnitude planes by overlying subdwarfs on MARCS transformed isochrones also showed systematic offsets between the different colour planes. This evidence indicates a potential problem with the J filter, in particular, in the MARCS transformations for metal-poor dwarf stars. The same conclusion is reached from a consideration of the Population II subdwarf standards, which also suggest a small problem with $(V - K)$.

When comparing results for giant branches, good agreement was found for high metallicity clusters, while the isochrones systematically became redder than the observations with decreasing [Fe/H]. One might expect such a correlated discrepancy in [Fe/H] to be caused by the failure of the model atmospheres to fully account for

all sources of blanketing that exist in real stars. However the isochrone fits to our high metallicity RGB fiducials, along with independent 2MASS observations of M67, indicate that inadequate line-blanketing is unlikely to be the cause, as the problems should *worsen* for higher metallicity stars, where the number of absorption lines in stellar atmospheres increase. Without comparing model spectra using different input parameters, such as mixing length, it is difficult to explain the cause of the RGB inconsistencies on the basis of isochrone comparisons to the CMDs.

Alternatively, the discrepancies noted between the predicted and observed giant branches may be due to the temperatures predicted by the stellar models themselves. Effective temperatures of stellar evolutionary models are less certain than luminosities which are driven by well modeled nuclear physics in the core, due to uncertainties in convection theory, efficiency of diffusive processes and low-temperature opacities. Since giant stars have enormous convective envelopes, their temperatures are the most strongly effected, while changing mixing length theory has a much reduced impact on the temperatures of main sequence stars. As a result, effective temperatures of the giants are generally considered to be uncertain by at least $\pm$ 100 K (VandenBerg 2005). Indeed, to account for the offsets we see in the RGB branches, the models would have to be hotter by $\sim$50-100K to match the entire RGB, depending on metallicity.

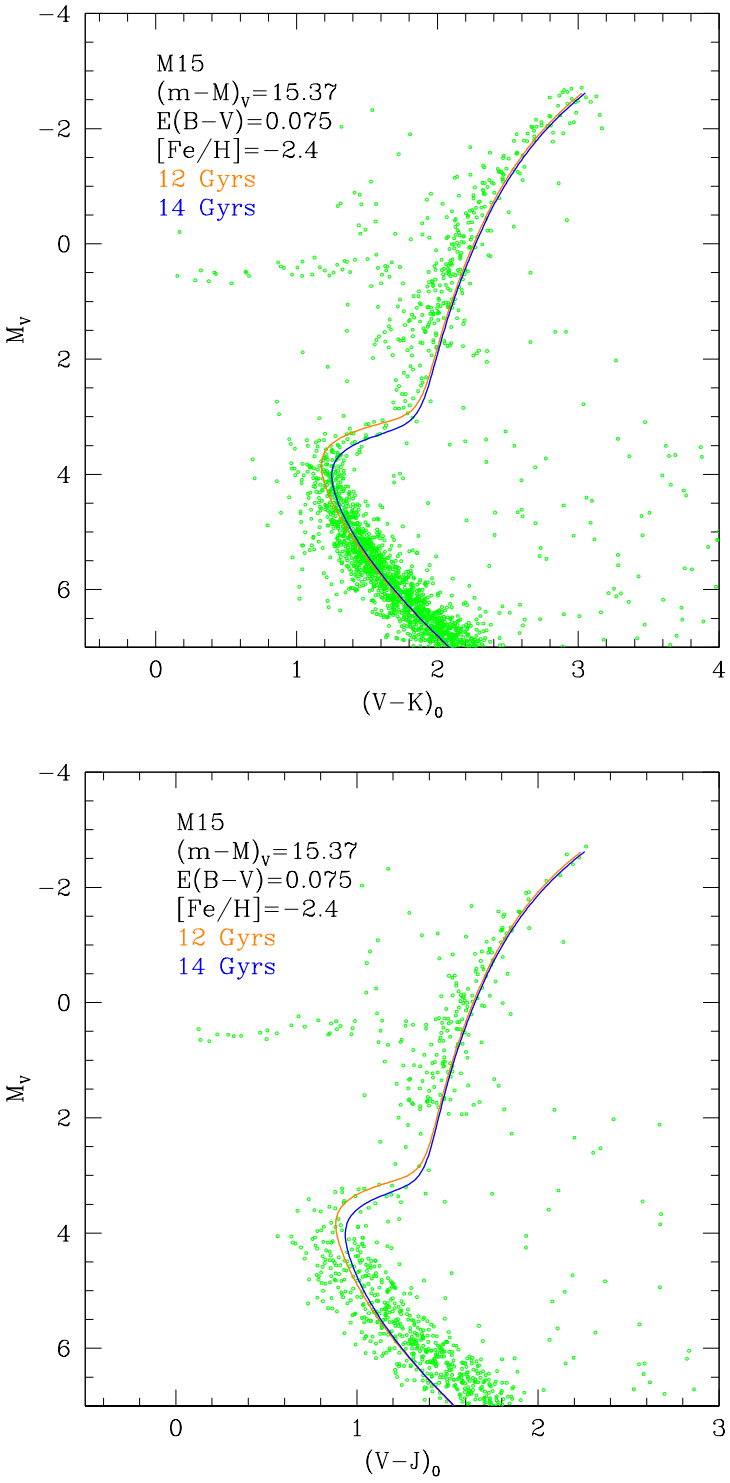

Figure 4.8 Fits of 12 and 14 Gyr Victoria isochrones to our M15 data using MARCS colours transformations.

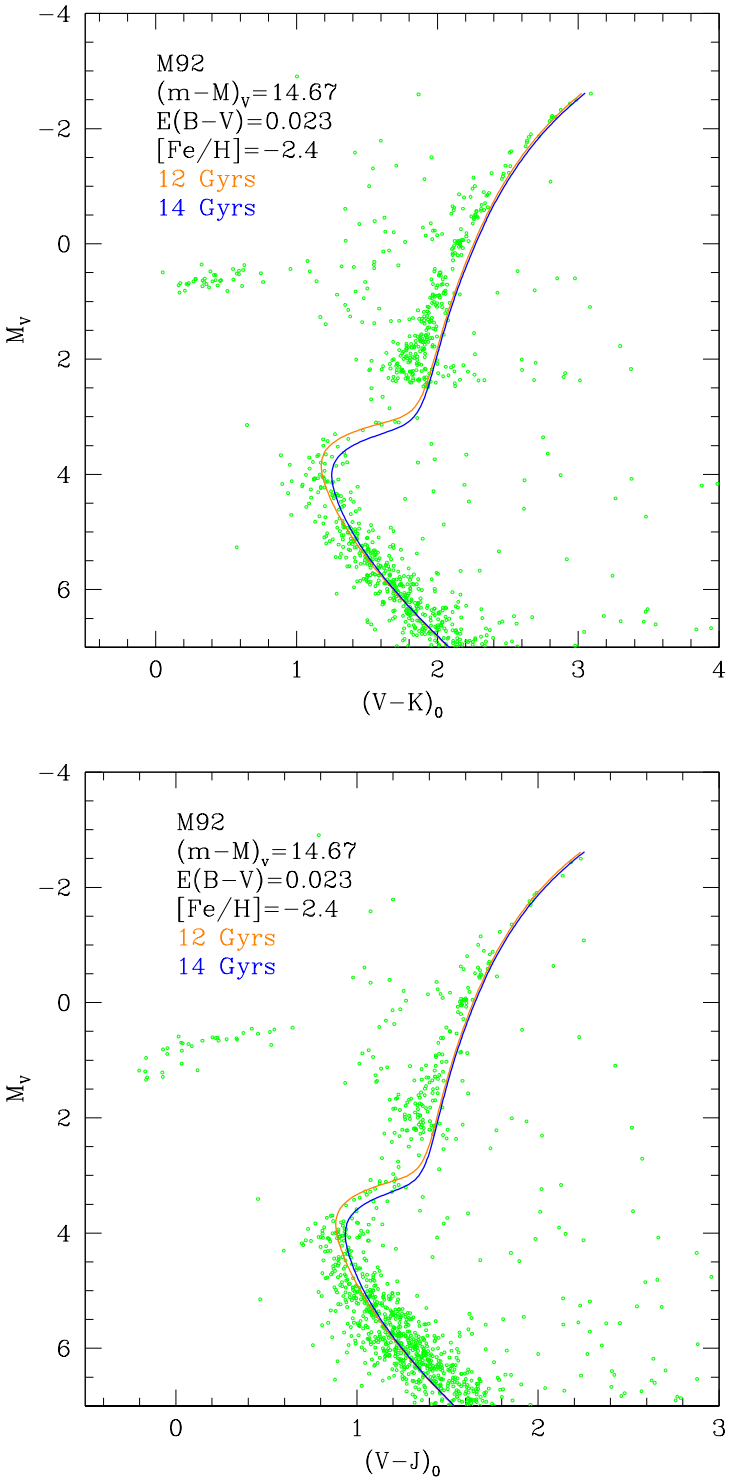

Figure 4.9 Fits of 12 and 14 Gyr Victoria isochrones to our M92 data using MARCS colours transformations.

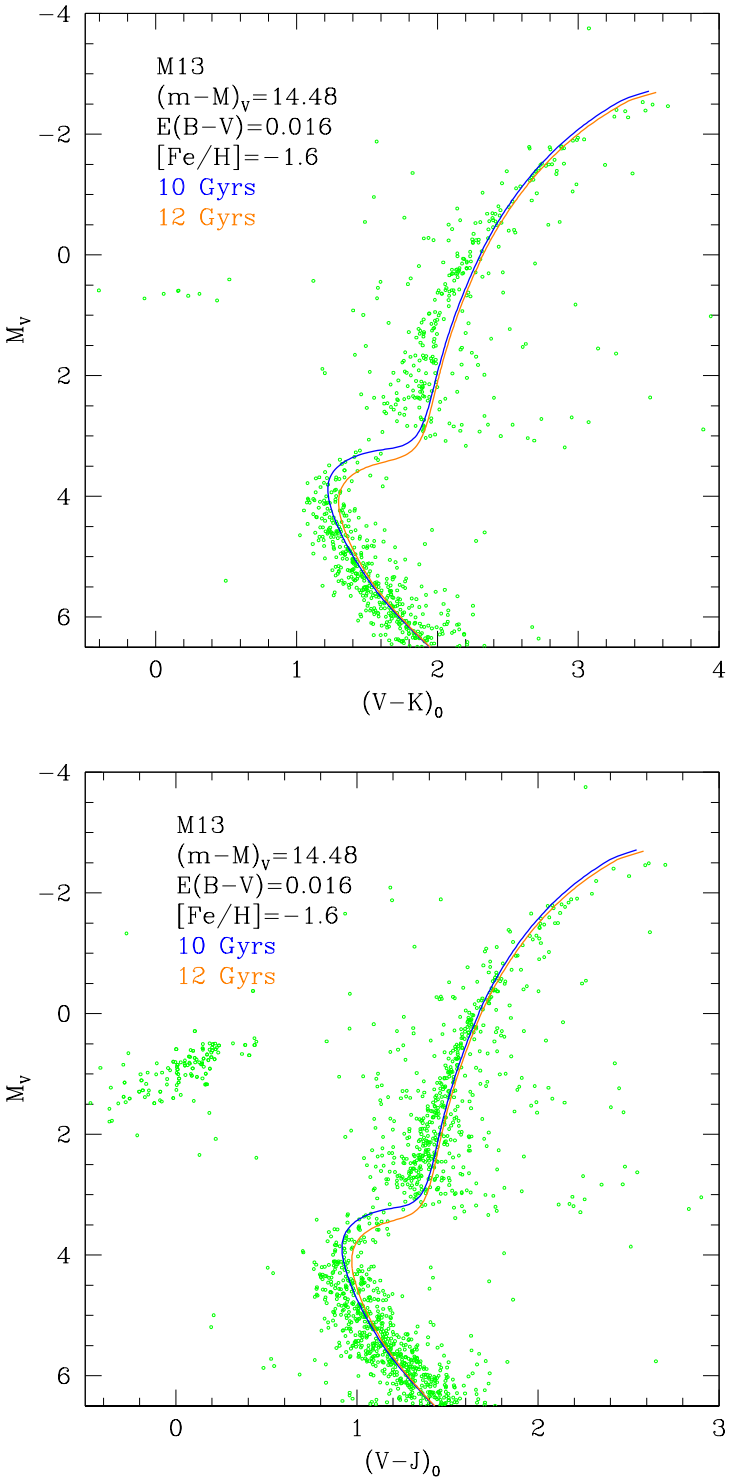

Figure 4.10 Fits of 10 and 12 Gyr Victoria isochrones to our M13 data using MARCS colours transformations.

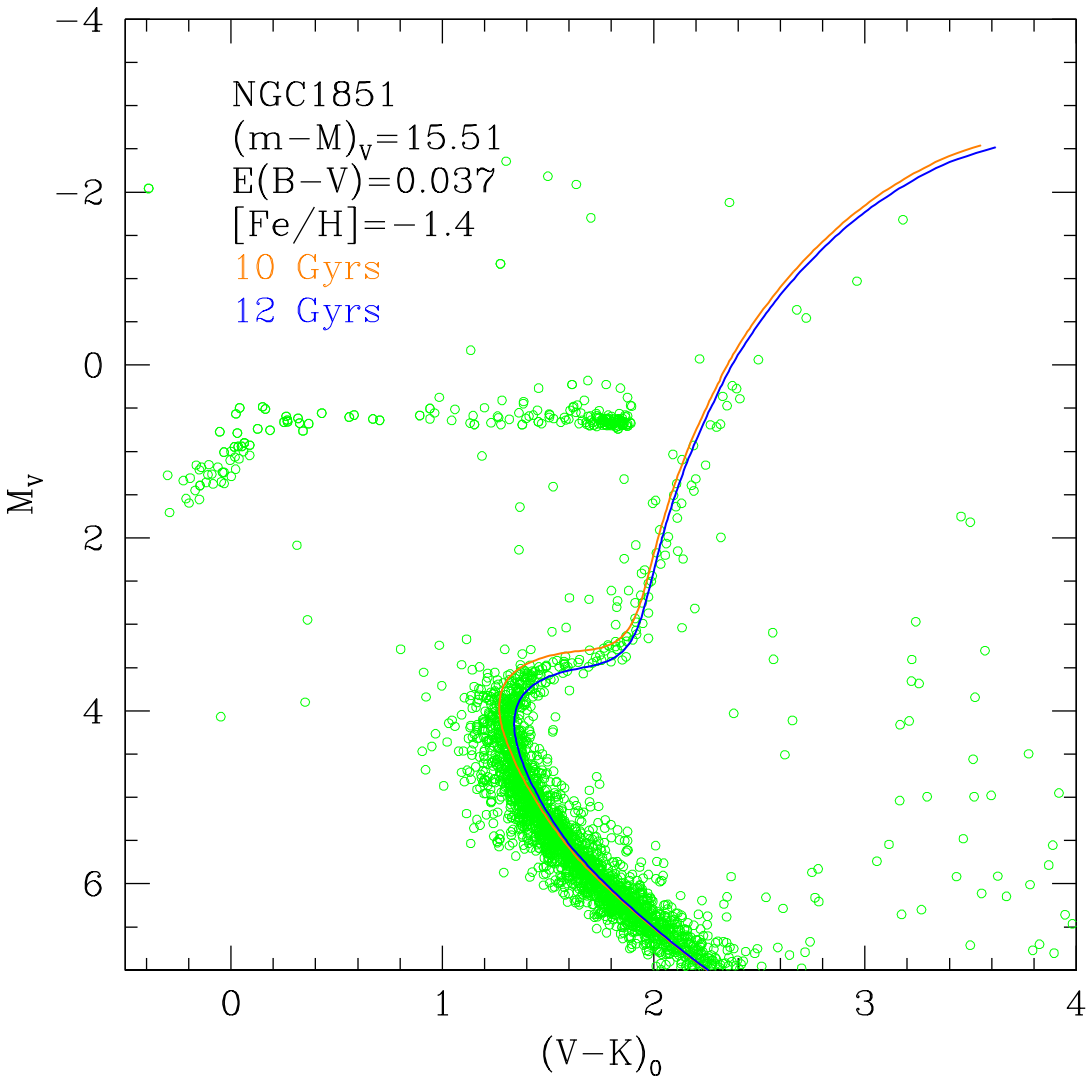

Figure 4.11 Fits of 10 and 12 Gyr Victoria isochrones to our VLT data of NGC1851 using MARCS colours transformations.

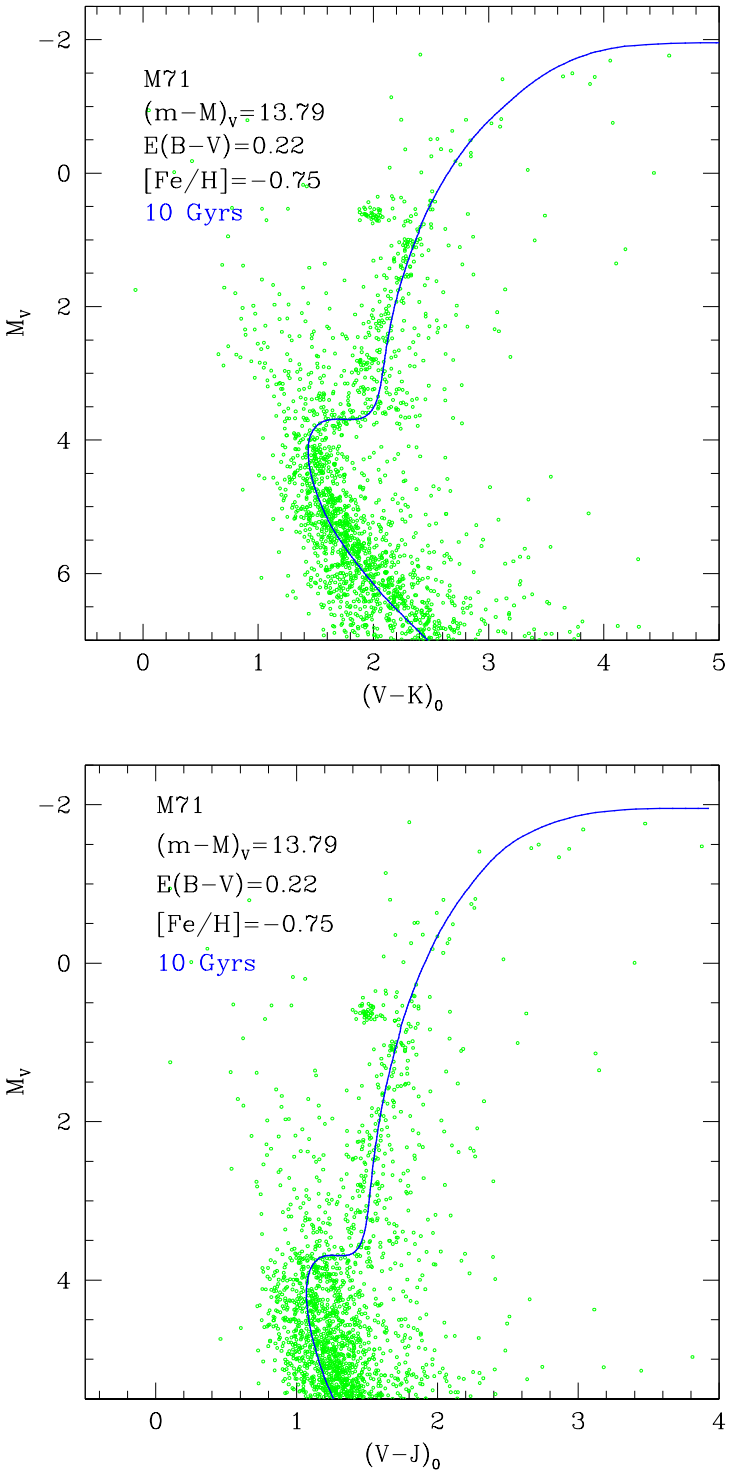

Figure 4.12 Fits of a 10 Gyr Victoria isochrone to our M71 data using MARCS colours transformations.

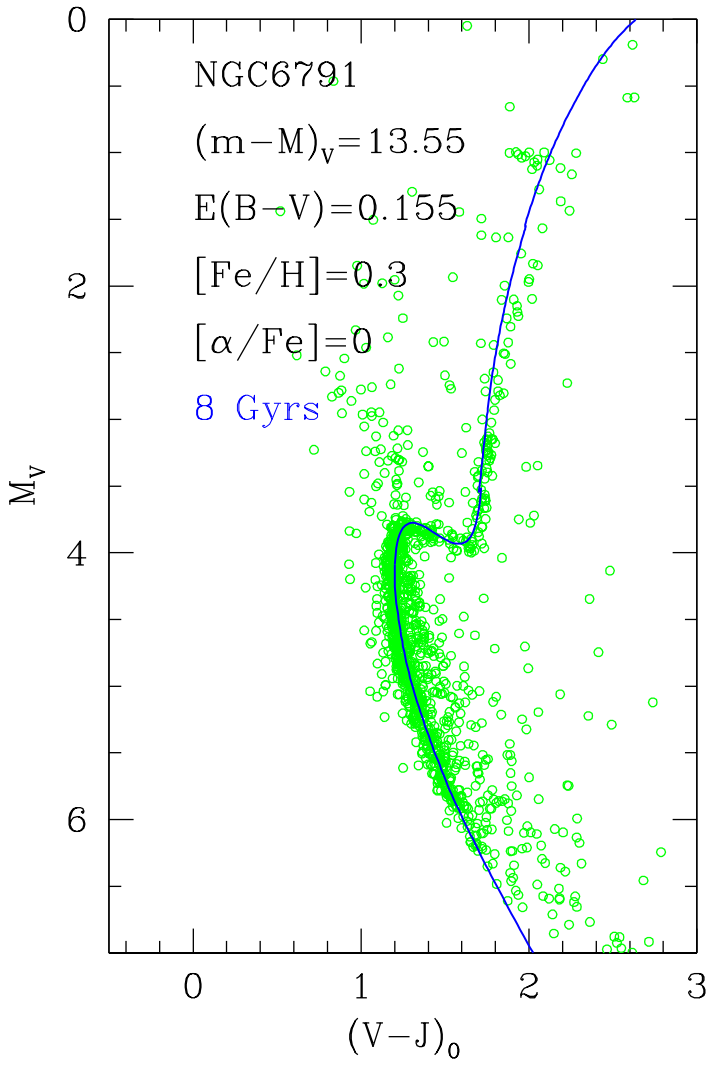

Figure 4.13 Fits of a 8 Gyr Victoria isochrone to our NGC6791 data using MARCS colours transformations.

Chapter 5

Summary

We have derived fiducial sequences for the Galactic star clusters M15, M92, M13, NGC1851, M71, and NGC 6791 (encompassing $-2.4 \leq$ [Fe/H] $\leq +0.3$) using near infrared observations obtained with the WIRCam imager on the Canada-France-Hawaii Telescope and HAWK-I on the VLT. These fiducial sequences, which are presented in Figure 5.1 on the $(V-J)_0 - M_V$ and $(V-K)_0 - M_V$ planes, demonstrate how the photometric properties of these old stellar populations vary as a function of [Fe/H]. With spectroscopic metallicity determinations and age estimates that are accurate to within $\pm$ 0.25 dex and $\pm$ 1.5 - 2 Gyr, respectively, these fiducials can, in principal, be used to photometrically determine the age and metallicity of resolved stellar systems. Unlike isochrone analyses, metallicity determinations made through comparisons with fiducials are independent of any evolutionary model. Thus these fiducials provide a set of empirical isochrones that will serve as valuable tools for future stellar population investigations involving the 2MASS bandpasses.

Based on these data, a summary of our results are as follows:

(1) A strong case is made in support of E$(B-V)$= 0.075, 0.22 and 0.155, for the historically controversial reddening values of M15, M71, and NGC6791, respectively.

(2) Tests of MARCS colour transformations using Population II subdwarfs indicate that the models predict $(V-K)$ and $(J-K)$ that are too red (by $\sim$ 0.03 mag) and that there appears to be a systematic offset with temperature in the case of $(V-J)$, consistent with what is observed when isochrones are fitted to the main sequences of our metal-poor clusters.

(3) Direct comparisons of Hipparcos subdwarfs with Victoria isochrones on the

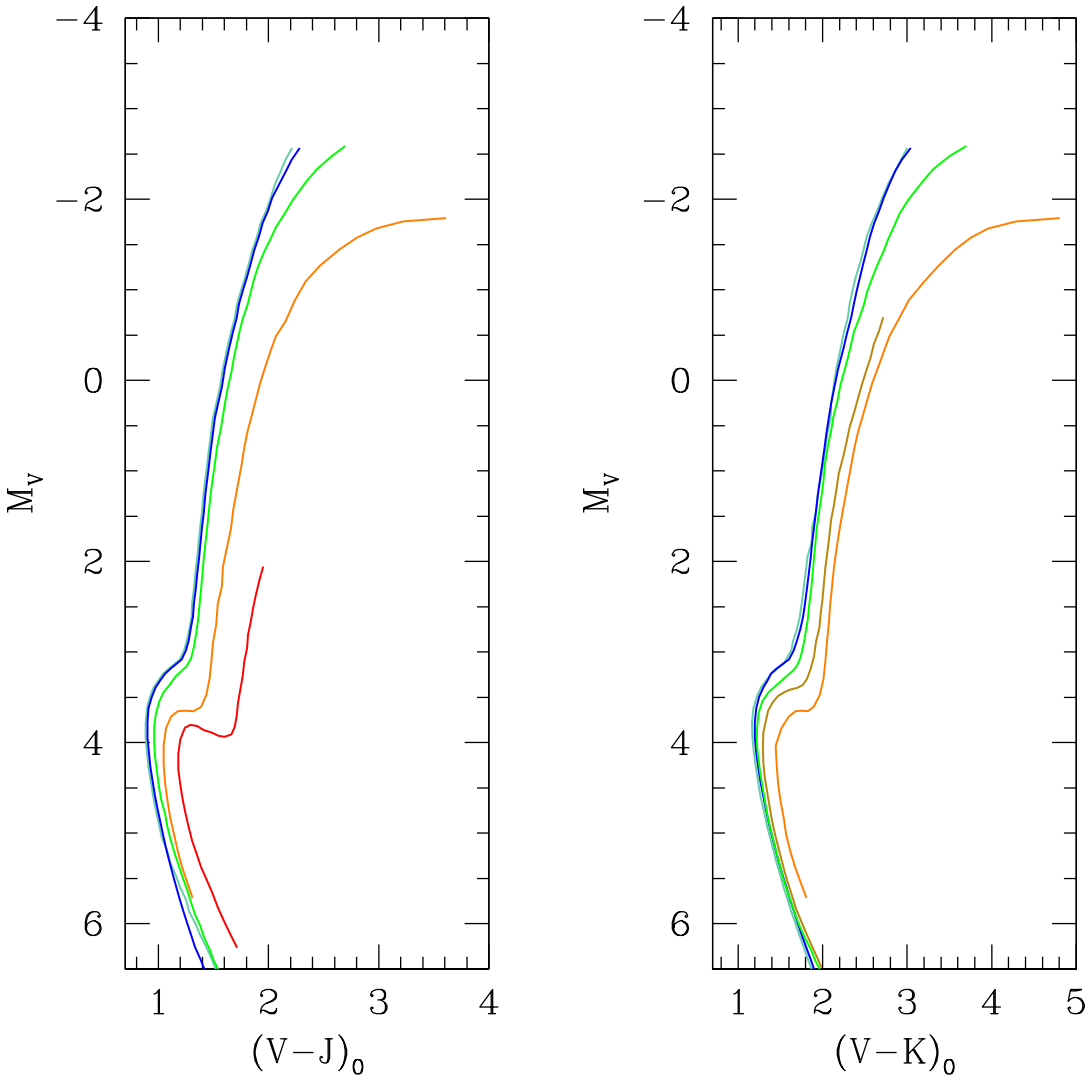

Figure 5.1 Our cluster fiducials mapped to the $(V-J)_0-M_V$ and $(V-K)_0-M_V$ planes using the reddenings and distance moduli given in Table 3.1. From left to right, corresponding to increasing metallicity, are M15 (turquoise), M92 (blue), M13 (green), NGC1851 (gold), M71 (orange) and NGC6791 (red).

$\log T_{\rm eff}$-M_V plane show that the model $T_{\rm eff}$ scale for main-sequence stars having [Fe/H]$\gtrsim -2$ agrees well with both the spectroscopic temperature scale of Gratton et al. (1996) and the photometrically-based scale of Casagrande et al. (in preparation).

(4) Isochrones show a systematic redward offset from the observed RGB loci as the metallicity of the cluster decreases below [Fe/H]~ -1.3, leading us to conclude the temperature scale of the stellar evolutionary models for giant stars at low metallicity are too cool, and/or the model atmospheres themselves are failing to predict the spectra of metal-poor giant stars.

Additional discussion concerning the aforementioned problem with the RGB colours is worthwhile. It is a widely held view in the astronomical community that both the empirical and predicted temperatures of giant stars are uncertain by at least $\pm$ 100 K (Ramirez & Meléndez 2005, VandenBerg 2005). Consequently, when examining the fits of isochrones to the giant branches of our clusters, it is difficult to disentangle uncertainties in the colour-$T_{\rm eff}$ relations from those of the effective temperatures of stellar models. Discrepancies between the observed and predicted giant branches of our cluster photometry are found to be a strong function of metallicity: the isochrones provide good fits to both the $(V-K)_0$-M_V and $(V-J)_0$-M_V CMDs for metal-rich clusters (e.g., M71), but the models predict increasingly redder RGB colours than those observed, as the metallicity decreases. For our most metal poor clusters, M92 and M15, the lower RGB segments of the isochrones appear to be too red by ~ 0.12 mag in $(V-K)$ and ~ 0.09 mag in $(V-J)$. Based on the fact that MARCS transformations give *consistent* predictions in the two colours, one could conclude these discrepancies are a result of problems with the effective temperatures of the stellar models, rather than the colour-$T_{\rm eff}$ relations.

Effective temperatures of stellar evolutionary models for giant stars are less trustworthy than those for dwarfs due to, for example, uncertainties in convection theory, the efficiency of diffusive processes, and the opacities at low temperatures. With the enormous convective envelopes of giant stars, changes in mixing length theory strongly affect their temperatures, while having a much weaker impact on the temperatures of stars along the main sequence. Since the discrepancies we see between predicted and observed RGBs are strongly a function of metallicity, it could indicate that convection in metal-poor stars is not well understood and may behave very

differently than in higher metallicity stars. While the mixing length parameter, α, in the model atmospheres and stellar models is assumed to be the solar value for all stars, it is possible that this parameter is a function of metallicity. Indeed, an increase in the assumed value of α from the solar value of $\alpha = 2.05$ to 2.30 would result in an appreciable bluer RGB for M92, nearly consistent with the observed $(V-K)_0$ photometry, in fact (D. VandenBerg, private communication).

On the other hand, it is possible that the temperatures of the stellar models are realistic, and the discrepancies seen along the RGB are a result of the MARCS models missing, for example, some additional physics in the atmospheres of low metallicity stars. Looking to empirical comparisons, the $(V-K)$-$T_{\rm eff}$ relation of Ramirez & Meléndez (2005) was shown in Chapter 1 to predict much bluer RGBs at low metallicity than the theoretical model atmospheres. The results of Ramirez & Meléndez are, however, considered controversial as they show a substantial sensitivity to [Fe/H] at low metallicities, in conflict with the findings of several other empirical studies (e.g., Nissen et al. 2007, Alonso et al. 1996). Even so, if the $(V-K)$-$T_{\rm eff}$ relation for giant stars by Ramirez & Meléndez (2005) is used to transpose the giant branch of a Victoria isochrone onto the CMD of our most metal poor cluster, M92, a good fit to the lower RGB stars is obtained — as shown in Figure 5.2. The difficulty matching the upper RGB could be an indication that there are systematic errors in the Ramirez & Meléndez transformations or in the model temperatures. This example illustrates how difficult it is to interpret any discrepancies that are found between synthetic and observed CMDs.

5.1 Future Work

As a follow up to the work presented here, our data will be examined along with the *uvby* and $u'g'r'i'z'$ observations (see Clem et al. 2004, 2008) that have already been obtained for the same target clusters we have observed with CFHT. By ensuring consistency across the many possible colour-colour and colour-magnitude diagrams that can be generated from these combined observations, significant improvements to both the 'observed' $T_{\rm eff}$ scale and to the transformations to JK_S, as well as to the other photometric systems, can be expected. Indeed, we will be able to produce a compilation of colour-colour relations for globular cluster dwarfs and giants to complement similar relations for field stars reported by Caldwell et al. (1993),

It is also important to investigate the consistency of the MARCS-transformed

isochrone fits across many colour-magnitude planes (e.g., $(B-V)$, $(V-I)$, $(V-K)$ etc.) simultaneously, when assuming consistent estimates of the cluster reddening, metallicity, and distance. Comparisons of MARCS-transformed isochrones to cluster photometry in $BV(RI)_C$ are part of a publication currently being prepared by Casagrande, VandenBerg and Stetson (in preparation); our future paper (Brasseur et al. 2009) will extend these comparisons to the near-infrared.

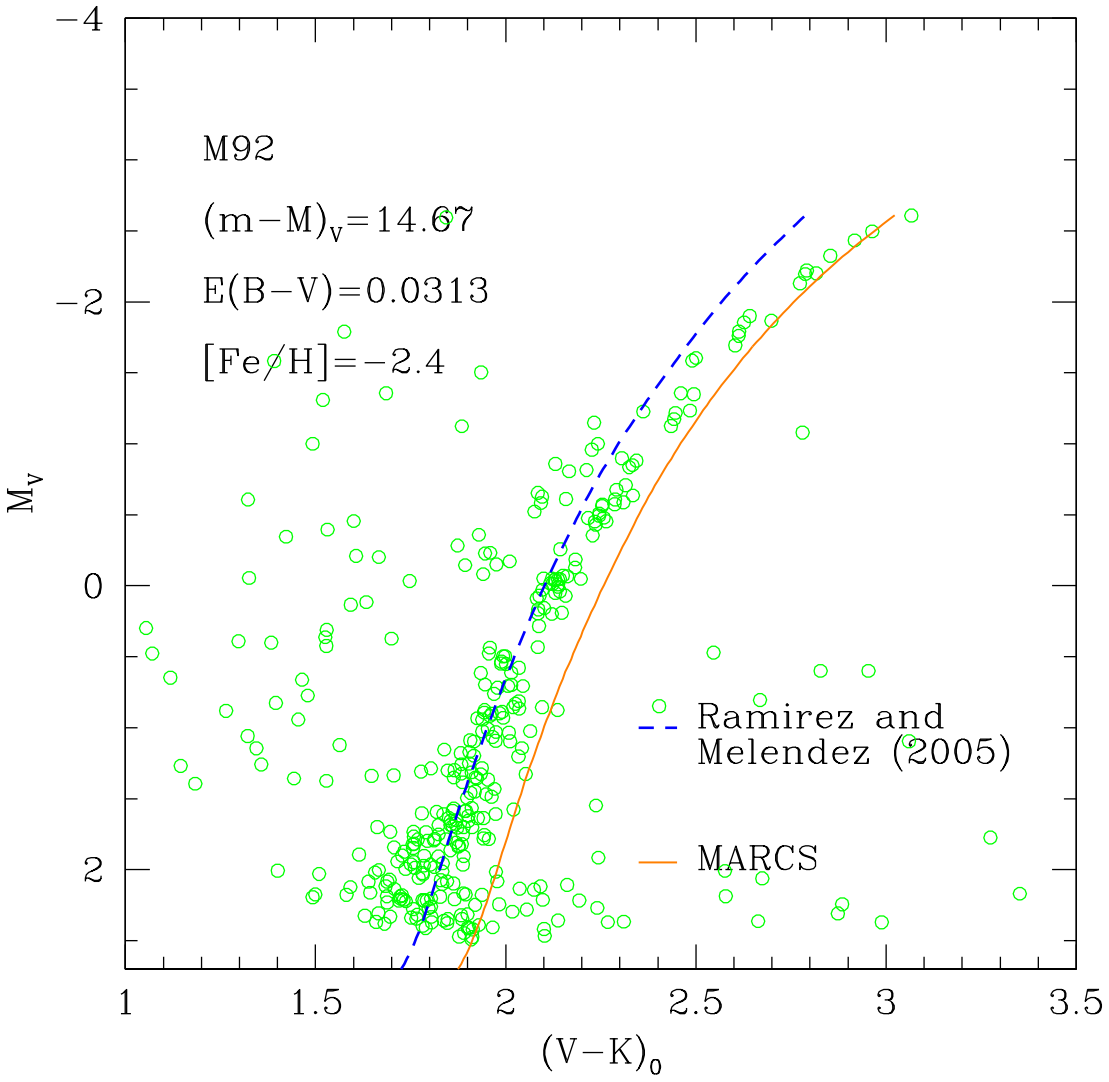

Figure 5.2 A comparison of the giant branch of M92 with the RGB segment of a 12 Gyr Victoria isochrone that has been transformed to the observational plane using the empirically constrained $(V-K)$-$T_{\rm eff}$ relations (Ramirez & Melendez 2005; dashed blue line) and the colour-$T_{\rm eff}$ relations based on MARCS model atmospheres (solid orange line).

Bibliography

Alonso, A., Arribas, S., & Martínez-Roger, C. 1996, A&A, 313, 873

Alonso, A., Arribas, S., & Martínez-Roger, C. 1998, A&A, 139, 335

Alonso, A., Arribas, S., & Martínez-Roger, C. 1999, A&A, 140, 261

Belokurov, V. et al. 2006, ApJ, 647, L111

Belokurov, V. et al. 2007, ApJ, 654, 897

Belokurov, V. et al. 2007, ApJ, 658, 337

Bergbusch, P. A. & VandenBerg, D. A. 2001, ApJ, 556, 322

Blackwell, D.E., Shallis, M.J., & Selby, M.J., 1979, MNRAS, 188, 847

Boesgaard, A.M., Jensen, E.E.C., & Deliyannis, C.P. 2009, AJ, 137, 4949

Bono G., Caputo F., Marconi M., 1995, AJ, 110, 2365

Cacciari, C., Caloi, V., Castellani, V., & Fusi Pecci, F., 1984, A&A, 139, 285C

Carretta, E., & Gratton, R. G., 1997, Astron. Astrophys. Suppl., 121, 95

Carretta et al. 2000, ApJ, 533, 215

Cassisi S., Salaris M., Pietrinferni A., Piotto G., Milone A. P., Bedin L. R., Anderson J., 2008, ApJ, 672, L115

Cassisi, S., De Santis, R., & Piersimoni, A. M. 2001, MNRAS, 326, 342

Cenarro, A., J., Peletier, R. F., Sanchez-Blazquez, P., et al. 2007, MNRAS, 374, 664

Chaboyer, B., Green, E. M., & Liebert, J. 1999, AJ, 117, 1360

Clem, J. L., Vandenberg, D. A., & Grundahl, F., Bell, R. A., 2004, AJ, 127, 1227

Cohen, J. C., & Sleeper, C. 1995, AJ, 109, 242

Collet, R., Asplund, M., & Trampedach, R., 2007, A&A, 469, 687

De Santis, R., & Cassisi, S. 1999, MNRAS, 308, 97

Durrell, P. R., & Harris, W. E. 1993, AJ, 105, 1420

Ferraro, F. R., Montegriffo, P. A., & Fusi-Pecci, F. 2000, AJ, 119, 1282

Ferraro, F., Valenti, E., & Origlia, L. 2006, ApJ, 649, 243

Friel, E. D. et al. 2002, AJ, 124, 2693

Frogel, J. A., Persson, S. E., Matthews, K., & Aaronson, M. 1978, ApJ, 220, 75

Frogel, J. A., Persson, S. E., & Cohen, J. G. 1981, ApJ, 246, 842

Frogel, J. A., Persson, S. E., & Cohen, J. G. 1983, ApJ, 53, 713

Gratton R.G., Carretta E., & Castelli F. 1996 A&A, 314, 191 (1996)

Grundahl, F., Stetson, P. B., & Andersen, M. I. 2002, A&A, 395, 481

Gustafsson, B., Edvardsson, B., Eriksson, K., Jorgensen, U.G., Nordlund, A., & Plez, B., 2008, A&A, 486, 951

Harris W. E., 1996, AJ, 112, 1487

Hempel, M., Hilker, M., Kissler-Patig, M., Puzia, T. H., & Minniti, D. 2003, A&A, 405, 487

Hodder P. J. C., Nemec J. M., Richer H. B., Fahlman G. G. , 1992, AJ, 103, 460

Jevremovic, D., Dotter, A., & Baron, E., 2007, Publications of the Astronomical Observatory of Belgrade, 82, 131

Jørgensen, U. G., Jensen, P., Sørensen, G. O., & Aringer, B. 2001, A&A, 372, 249

Kron G. E., Guetter H. H., 1976, AJ, 81, 817

Kaluzny, J., & Rucinski, S. M. 1995, A&AS, 114, 1

Kuchinski, L. E., Frogel, J. A., Terndrup, D. M., & Persson, S. E. 1995, AJ, 109, 1131

McCall, M.L. 2004, AJ, 128, 2144

Meléndez, J., & Ramírez, I. 2004, AJ, 615, 2004

Meléndez, J., & Ramírez, I. 2005, ApJ, 626, 465

Milone A. P. et al., 2008, ApJ, 673, 241

Pont, F., Mayor, M., Turon, C., & VandenBerg, D. A. 1998, A&A, 329, 87

Ramírez, I. & Meléndez, J. 2005, ApJ, 626, 446

Ramírez, I. & Meléndez, J. 2005, ApJ, 626, 465

Rejkuba, M. 2004, A&A, 413, 903

Renzini, A. 2008, MNRAS, 391, 354

Sandage, A. R., Lubin, L. M. and VandenBerg, D.A., 2003, PASP, 115, 1187

Schlegel, D.J., Finkbeiner, D.P., and Davis, M. 1998, ApJ, 500, 525

Smart, W.M. Text book on Spherical Astronomy, Fifth Edition. Cambridge University Press, 1965

Smith, V. V., Lambert, D. L., & Nissen, P. E. 1998, ApJ, 506, 405

Sneden, C., Kraft, R. P., Prosser, C. F., & Langer, G.E., 1991, AJ, 102, 2001

Taylor, B. J. 2007, AJ, 133, 370

Twarog, B. A., Ashman, K. M., & Anthony-Twarog, B. J. 1997, AJ, 114, 2556

Valenti, E., Ferraro, F., & Origlia, L. 2004, AJ, 133, 1287

VandenBerg D. A., 2000, ApJS, 129, 315

VandenBerg, D. A., Swenson, F. J., Rogers, F. J., Iglesias, C. A., & Alexander, D. R. 2000, ApJ, 532, 430

VandenBerg, D.A., Clem, J. L., 2003, AJ, 126, 778

VandenBerg D. A., 2005, ASP Conference Series, eds. D. Valls-Gabaud & M. Chavez, 2006, in press

VandenBerg D. A., 2008, Physica Scripta, 133, 14026

Wing, R. F., Jørgensen, U. G. The Journal of the American Association of Variable Star Observers, 31, 110

Zinn, R., & West, M. J., 1984, AJS, 55, 45